Nonstationary Heat Conduction in Atomic Systems

A THESIS
SUBMITTED TO THE FACULTY OF THE GRADUATE SCHOOL
OF THE UNIVERSITY OF MINNESOTA
BY

Amit K Singh

IN PARTIAL FULFILLMENT OF THE REQUIREMENTS
FOR THE DEGREE OF
Doctor of Philosophy

Adviser: Prof. Ellad Tadmor

November, 2015

© Amit K Singh 2015
ALL RIGHTS RESERVED

Acknowledgements

This thesis would not have completed without the guidance of my adviser, Prof. Ellad Tadmor, so I would first like to express my sincere gratitude to him. His scholarly suggestions, countless revisions of several manuscripts and continuous encouragement kept me going. Several discussions with him have continued clearing my doubts. His focus on even minor problems always helped me to bring more rigor into the work. It has been a real fun working with him all these years.

Next I would like to thank the department office staff, menet computing staff, janitors and several other support workers, who provide the backbone of the environment where scientific research is made possible. I would specially thank Julie Koch, Ray Muno, Lisa Schouviller and Laila Ramadi.

I would also like to thank my dissertation committee, Prof. Richard James, Prof. Ryan Elliott, Prof. Thomas Schwartzentruber, Prof Roberto Ballarini and Prof. Xiaojia Wang, for several insights and discussions. My several academic interactions with other faculty members of the department such as with Prof. Roger Fosdick and Prof. Perry Leo have also been very fruitful. So a big thanks to all of them. But I would like to save my sincerest tribute for Prof. Daniel Joseph whose work has been the overarching influence on my PhD research.

My deepest debt goes to my grandparents Ramjanam and Rajmani, my parents Ashok and Pramila, and siblings Anit and Anish, for being the source of continuous inspiration and joy. Their support, love and encouragement have been the fundamental strength all these years.

The ink would not have colored the thesis without the rainbow provided by my beloved Poonam who has always created magic. My greatest debt goes to her. The thesis would not have taken any shape without her patience and unconditional support.

And I cannot forget my roommates, officemates and colleagues. The time spent with Vivekanand Dabade, Subrahmanyam Pattamatta, Nikhil Admal, Amartya Banerjee, Vijay Srivastava, Venkata Guthikonda, Shankar Krishnan, Ganesh Borra, Dan Karls and Vincent Jusuf, have benefited my understanding immensely. More than anything else I have savored the discussion on several topics with these outstanding colleagues. I would also like to thank the group members, Mingjian Wen, Ilia Nikiforov, Jiadi Fan, Alexander Anastassiou and Min Shi with whom I have shared my research and participated in weekly meetings and seminars. Special thanks to Stephen Whalen and Valeriu Smiricinsch for all the help in finding bugs in some of my codes!

I would also like to thank my friends in India, Minneapolis, and everywhere spread around the world who have been creating progressive waves in this deeply flawed yet so beautiful world!

To my family members, Poonam and all progressive friends.

Abstract

Understanding heat at the atomistic level is an interesting exercises. It is fascinating to note how the vibration of atoms result into thermodynamic concept of heat. This thesis aims to bring insights into different constitutive laws of heat conduction. We also develop a framework in which the interaction of thermostats to the system can be studied and a well known Kapitza effect can be reduced. The thesis also explores stochastic and continuum methods to model the latent heat release in the first order transition of ideal silicon surfaces into dimers. We divide the thesis into three works which are connected to each other:

1. Fourier's law leads to a diffusive model of heat transfer in which a thermal signal propagates infinitely fast and the only material parameter is the thermal conductivity. In micro- and nano-scale systems, non-Fourier effects involving coupled diffusion and wavelike propagation of heat can become important. An extension of Fourier's law to account for such effects leads to a Jeffreys-type model for heat transfer with two relaxation times. In this thesis, we first propose a new *Thermal Parameter Identification* (TPI) method for obtaining the Jeffreys-type thermal parameters from molecular dynamics simulations. The TPI method makes use of a nonlinear regression-based approach for obtaining the coefficients in analytical expressions for cosine and sine-weighted averages of temperature and heat flux over the length of the system. The method is applied to argon nanobeams over a range of temperature and system sizes. The results for thermal conductivity are found to be in good agreement with standard Green-Kubo and direct method calculations. The TPI method is more efficient for systems with high diffusivity and has the advantage, that unlike the direct method, it is free from the influence of thermostats. In addition, the method provides the thermal relaxation times for argon. Using the determined parameters, the Jeffreys-type model is able to reproduce the molecular dynamics results for a short-duration heat pulse where wavelike propagation of heat is observed thereby confirming the existence of second sound

in argon. Implementations of the TPI method in MATLAB are available as part of the online supplementary material.

2. The second major work of the thesis is to look into the following problem. The direct method for computing thermal conductivity in nonequilibrium molecular dynamics gives rise to an artificial Kapitza resistance at the interface between thermostatted and unthermostatted regions. This resistance, which depends on the system size and the thermostat parameters, creates discontinuous jumps in the temperature and heat flux across the interface and therefore affects the measured thermal conductivity. In this part, we propose a phenomenological relation for the Kapitza resistance that can be used to extract a value for the bulk thermal conductivity, which is independent of the system size and thermostat details. We also provide insight into the Kapitza phenomenon resulting from numerical thermostatting.

3. This constitutes our third part of the thesis. Silicon (001) surfaces in non-equilibrium molecular dynamics (NEMD) simulations above a critical transformation temperature undergo a reconstruction from the ideal diamond crystalline surface to a reconstructed structure involving the formation of rows of dimers along a $\langle 110 \rangle$ direction. This process is accompanied by latent heat release that in NEMD simulations results in a dramatic increase in temperature of nanobeams that cross the transformation temperature as they are heated. To model this behavior, we propose a hybrid continuum partial differential equation for non-Fourier heat transfer coupled with a stochastic kinetic Monte Carlo (KMC) algorithm to account for latent heat release. An input to the method is the energy barrier for dimerization, which is computed separately using nudged elastic band calculations. The time-dependent temperature profiles along the beam predicted by the continuum-KMC method are in good agreement with the NEMD results.

Contents

List of Tables

List of Figures

Chapter 1

Introduction

At the atomistic level understanding heat transfer is of both academic and technological interest. In any theory describing heat transfer, a constitutive assumption is necessary to relate the heat flux vector $\boldsymbol{q}(\boldsymbol{x}, t)$ and the temperature gradient $\boldsymbol{\nabla}\theta(\boldsymbol{x}, t)$, where $\boldsymbol{x}$ is a position in the current configuration and t is the time. Such a relation can be very general as long as it satisfies constraints on its form imposed by the second law of thermodynamics (see for example Section 6.2.2 in Ref. [1]). The simplest theory of heat transfer adopts Fourier's law of heat conduction in which a linear relation is assumed between the heat flux and temperature gradient for a homogeneous isotropic body,

$$\boldsymbol{q}(\boldsymbol{x}, t) = -k\boldsymbol{\nabla}\theta(\boldsymbol{x}, t), \tag{1.1}$$

where k is the thermal conductivity of the material. As we review in Chapter 2, Fourier's law leads to the heat equation, a parabolic partial differential equation (PDE) that describes heat transfer as a diffusive process. The heat equation faces the conceptual problem that a sudden change of temperature at any point in space is felt instantly everywhere. It can be said that diffusion assumes an infinite speed of propagation (see p. 42 in Ref. [2]). In reality, a finite time is involved in heat transfer in solids, which occurs through collisions between energy carriers – free electrons and phonons – and also by scattering of these carriers at boundaries and material defects. Phonons are the major heat carriers for insulators and semiconductors, whereas free electrons are the dominant carriers in metals [3]. Some important features of the energy carriers are listed in Table 1.1. In order for continuum macroscopic properties like heat flux, stress

Some features of heat carriers [3]

	Free Electron	Phonon	Photon
Generation	valence or excited electron	lattice vibration	atomic, molecule transition
Statistics	Fermion	Boson	Boson
Frequency	0 to ∞	Debye cut-off	0 to ∞
Dispersion	$E = \hbar^2\mathbf{K}^2/(2m)$	$E = E(\mathbf{K})$	$\nu = c/\lambda$
Velocity (m/s)	$\sim 10^6$	$\sim 10^3$	$\sim 10^8$

Table 1.1: $E, \hbar, \mathbf{K}, m, \nu, c$ and λ correspond to energy, reduced Planck constant, wavevector, mass, frequency, speed of light and wavelength respectively.

and temperature, to be well defined in a statistical mechanics sense, a 'large' number of collisions must take place. Based upon this 'large' concept, a mean free path and mean free time or relaxation time, can be defined. Essentially the dynamics of carriers suggests a finite thermal wave speed, which needs to be described by any macroscopic model developed for understanding heat conduction, otherwise the microscale thermal phenomena happening at the level of relaxation time and mean free path will not be captured. The average distance traveled by a carrier in the bulk material before being scattered by other phonons is the mean free path Λ. Various temperature dependent scattering mechanisms, that involve phonons, electrons, impurities and imperfections, determine Λ. Other characteristic lengths can also be defined such as the characteristic dimension D (e.g. diameter, width, height, length etc), the characteristic wavelength λ_c and the temperature penetration depth d_T. λ_c appears because of the duality of the wave-particle for electrons and phonons and is equal to the thermal de Broglie wavelength $h/\sqrt{2\pi m k_B \theta}$ [4], where h, m and θ denote Planck constant, effective mass of the carrier and characteristic temperature of the system, respectively. The dominant phonon wavelengths at high temperature is of the order of lattice constant a and at low temperature they are of the order of $\frac{a\,\theta_D}{\theta}$, where θ_D is Debye temperature. Temperature penetration depth is defined as the characteristic temperature divided by the maximum temperature gradient, i.e. $d_T = \theta/\left(|\nabla\theta|\right)_{max}$. Figure 1.1 illustrates the characteristic lengths in conduction.[1]

The finite speed of heat transfer was recognized by many including Chester [6], and

[1] For an in-depth discussion of different length and time scales governing microscale phenomena, see Tien and Chen (1994) [3], Tzou (1997) [5].

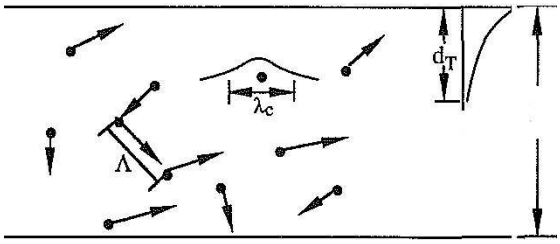

Figure 1.1: Illustration of characteristic lengths in heat conduction

Joseph and Preziosi [2] in their seminal paper on "heat waves." In the latter work as well as in earlier contributions by Cattaneo [7, 8] and Vernotte [9, 10], *non-Fourier* heat transfer models were proposed in which the relationship between $\boldsymbol{q}(\boldsymbol{x}, t)$ and $\boldsymbol{\nabla}\theta(\boldsymbol{x}, t)$ is more complex. The Cattaneo-Vernotte (CV) model leads to a hyperbolic PDE which combines wave-like and diffusive features. This model predicts that thermal discontinuities propagate at a finite velocity c. A more general Jeffreys-type model leads to a PDE in which thermal discontinuities are smoothed out as they propagate. The Jeffreys-type model includes in addition to the thermal conductivity k, two relaxation times τ_q and τ_θ. The CV and Fourier models can be obtained as special cases of the Jeffreys-type model. Various other heat-propagation models have been proposed and are comprehensively reviewed by Straughan [11].

While the question whether non-Fourier effects are present at the macroscale is controversial (see for example Refs. [12, 13, 14, 15]), there is no doubt that such effects exist and play an important role in micro and nano-scale systems [16]. This has great technological importance since modern microfabrication processes involve the miniaturization of devices that contain semiconductors, insulators and metallic layers on micro and nanometer scales. Fourier heat transfer breaks down when the characteristic lengths associated with the device approach the mean-free path of the energy carriers (electrons and phonons) [17]. For example, Fourier's law cannot explain the thickness dependence of the thermal conductivity of silicon [17, 18, 19]. Pilgrim et al. [20] studied the transient behavior of heat pulses in samples of GaAs and found that while the Fourier model successfully captured the thermal effects in larger samples, the CV model was more suitable for samples of smaller size. Lor and Chu [21] found that the CV model explained the heat transport in a thin film of a high-temperature yttrium barium copper

oxide superconductor deposited on various substrates. Wagner et al. [22] developed an energy-conserving method to couple atomistic MD regions to continuum finite element regions for nanoscale thermal problems, and suggested using a CV model to describe heat transfer in continuum regions.

Non-Fourier effects are also important on very short timescales. For example, when laser pulses are used for annealing semi-conductors, oscillatory heat flux boundary conditions (BCs) must be considered [23, 24] that cannot be described by Fourier theory. Similarly, thermal resonance phenomena due to the excitation of a body heat source oscillating at a given frequency cannot be explained by Fourier's Law [25, 26, 27, 28]. Just as displacement waves due to mechanical vibrations can lead to resonance in the displacement amplitude, a resonance phenomenon may occur in the wave amplitude of the temperature when a material is subjected to oscillatory heat flux BCs. Research in non-Fourier heat conduction also finds application in cryogenic systems, spacecraft thermal control coatings and superconducting thin films [29], reactor fuel rods [30], phase changes [31, 32], planetary heat propagation [33, 34], chemotaxis [35], skin burns [36], and other applications [11, 37, 38].

Heat transfer in atomic-scale systems has been explored computationally with molecular dynamics (MD) using two primary approaches: (1) the Green-Kubo relations within equilibrium MD; and (2) direct measurement of the thermal response in a nonequilibrium MD (NEMD) simulation. The Green-Kubo relations, which are based on the fluctuation-dissipation theorem, relate thermal conductivity to an integral of the time correlation function of the heat current (see Eq. (3.58) below). In the direct method, a thermal gradient is imposed on the system by thermostatting its ends and measuring the heat flux at steady state from which the thermal conductivity can be readily computed using Eq. (1.1). Ladd et al. [39] carefully compared the formally exact Green-Kubo relations with the direct NEMD approach and a method based on phonon perturbation theory for a face-centered cubic (fcc) lattice with "soft-sphere" interactions. They found that the Green-Kubo method works well over a broad range of temperatures but requires long simulation times to obtain good statistics. The other two methods are more efficient but were found to have a limited range of applicability. In particular, NEMD works well at higher temperatures whereas phonon perturbation theory is appropriate only at low temperatures. More recently, Schelling et al. [40] confirmed these results and showed

that at high temperature the direct NEMD method and the Green-Kubo approach give similar values for the thermal conductivity of silicon.

The MD studies described above have been primarily focused on Fourier heat transfer. However, Non-Fourier effects have also been observed in atomistic simulations. An important early study of this kind was performed by Tsai and MacDonald [41] who studied the response of a body-centered cubic (bcc) lattice to a strong heat pulse applied at the boundary. The authors observed that the disturbance propagated into the bulk "as a combination of first and second sound superimposed on a diffusive background." Here "first sound" refers to the propagation of a stress wave and "second sound" to the propagation of a thermal wave (see for example Ref. [6]). The "diffusive background" is captured by Fourier's model. No attempt was made to relate these results to non-Fourier heat transfer models. Later, Volz [42] performed similar NEMD simulations on a solid beam of fcc argon and tested the validity of the CV model. It was found that the CV model is adequate under equilibrium conditions, but does a poor job of describing the microscopic response in the initial nonequilibrium regime after the injection of heat. More recently, Mohamed and Srivastava [43] found that heat pulses of picosecond duration in single-walled carbon nanotubes induce several wave packets that travel at different propagation speeds. The largest amount of energy was found in the waves moving at the second sound speed. Single-walled nanotubes were also studied by Shiomi and Maruyama [44] who concluded that heat is conducted in a wavelike fashion. They also found that the flux profiles cannot be predicted by the hyperbolic wave equation (the CV model), but can be captured by taking the dual relaxation time scale into account, thus confirming the validity of Jeffreys-type models. Liu et al. [45] studied transient thermal conduction in pure and vacancy-containing argon films by applying a temperature jump to one end of the film and then calculating the thermal wave speed and relaxation times appearing in the non-Fourier models. They found that the wave speed is the same in both pure argon films and argon films with vacancy defects.

A practical problem with the NEMD approach is the existence of discontinuous jumps in temperature at the model boundaries where temperature is controlled. These jumps, which are referred to as the *Kapitza effect*, are due to phonon scattering at the interface between thermostatted and unthermostatted regions that causes a sharp change in thermal conductivity at the interface. The scattering occurs because thermostatting

algorithms corrupt the dynamics of the thermostatted atoms [46]. This effect leads to a discontinuity in the temperature gradient at the interface, giving rise to a jump in the temperature. Tenenbaum et al. [47] observed this phenomena in their early simulations and attempted to quantify the jumps. Aoki and Kusnezov [48] developed a quantitative description of the jumps by studying nonequilibrium properties of a one-dimensional (1D) lattice Hamiltonian (see the book by Pitaveskii and Lifshitz [49] for more details on their approach). Other researchers have also studied this effect or observed similar temperature jumps in their simulations [40, 50, 51, 52, 53]. We discuss a phenomenological model for addressing the Kapitza effect in MD simulations in Chapter 5. There we have also developed a novel method to reduce the computation cost of the direct method by taking into account the effect of friction constants of the thermostats [54].

The discussion above makes it clear that there is interest in determining the non-Fourier thermal behavior of material systems especially at the micro- and nano-scales where MD can be applied. The Green-Kubo and direct NEMD methods can be used to obtain the thermal conductivity k of the material but can be slow and difficult to apply accurately and they do not provide the thermal relaxation times.

In this thesis, we extend the approach of Daly et al. [55] for computing thermal conductivity by monitoring the decay of an initially imposed sinusoidal temperature distribution, to extract the Jeffreys-type model parameters, k, τ_q and τ_θ, from NEMD simulations of a 1D nanobeam. The nanobeam is first equilibrated with a sinusoidal temperature distribution using independent thermostats at equidistant positions along the length of the beam. The thermostats are then removed and the nanobeam evolves under under constant energy (NVE) conditions. During this nonequilibrium unsteady process, time-averaged temperature and heat-flux profiles along the nanobeam are computed and stored at regular intervals. These profiles are fitted to analytical solutions of the CV and Jeffreys-type PDEs. Thus a nonlinear regression-based *parameter identification* procedure is applied in which the coefficients of the governing PDE are obtained by analyzing the NEMD data. We refer to this method for obtaining thermal parameters as "TPI" (thermal parameter identification). The advantage of this approach is that relatively few profiles are needed to obtain the parameters to good accuracy which means that the NEMD simulation only needs to be run for a short time following the initial sinusoidal temperature equilibration.

In this thesis, we also explore the latent heat release accompanying surface reconstruction and its effect on the temperature of silicon nanostructures. For this purpose. the nanobeam temperature is initially 10 K and then the temperatures of both ends are raised to 30 K and maintained at this level. The interior of the beam gradually heats up because of the surface reconstruction, and rather than stabilizing at 30 K as expected, a dramatic overshooting in temperature occurs due to release of latent heat that accompanies dimer formation in the reconstruction process. To model this phenomenon we use a continuum partial differential equation (PDE) for non-Fourier heat transfer [2] parametrized using a novel thermal parameter identification (TPI) scheme based on an iteratively reweighted least squares (IRLS) regression method [56]. The injection of energy due to the latent heat released by dimerization is modeled using a stochastic Kinetic Monte Carlo (KMC) algorithm [57] that is coupled to the continuum PDE. The KMC rates are estimated using harmonic transition state theory (h-TST) with the activation barrier for dimer formation computed from the atomistic model using the climbing image nudged elastic band (CI-NEB) method [58]. The whole phenomenon is discussed in Chapter 6. [2]

[2] This part is in the process of a paper submission and we would like the graduate student office to hold the thesis till the paper is accepted for publication.

Chapter 2

Heat Conduction

Out of the three basic modes of heat transfer – conduction, radiation and convection – conduction is postulated to be related to the transfer of kinetic energy by the molecular movement in liquids and gases. The molecular movement involves the transfer of kinetic energy of the molecules in high temperature regime by successive collisions to the molecules in low temperature regime [59]. In crystalline solids, however, instead of collision of molecules, energy is transferred by the vibrations of phonons, the drifting of electrons, the scattering of phonons and interaction between phonons and electrons. Energy transfer via radiation further includes the photons as energy carriers [3], [5]. Here our emphasis is on understanding the mechanism of heat transfer via phonon vibrations in insulators.

Fourier's law of heat conduction, described in Eq. (1.1), relates the heat flux vector and the temperature gradient. For a rigid solid body without heat sources, the energy equation is (see for example Section 10.2 in Ref. [1])

$$\frac{\partial e}{\partial t} = -\boldsymbol{\nabla} \cdot \boldsymbol{q}, \tag{2.1}$$

where $e = e(\boldsymbol{x}, t)$ is the internal energy per unit volume. From the first law of thermodynamics, for rigid solid bodies where mechanical work cannot change the volume or shape of the system, we have

$$\frac{\partial e}{\partial \theta} = \gamma, \tag{2.2}$$

where $\gamma = \rho c_v$ is volumetric heat capacity, which is a product of the mass density and the specific heat at constant volume. Using Eqs. (1.1)–(2.2), we obtain Fourier's heat

equation:

$$\frac{\partial \theta}{\partial t} = \frac{k}{\gamma}\nabla^2\theta. \tag{2.3}$$

This is a parabolic PDE which describes heat transfer as a diffusive process. As discussed in Chapter 1, this model assumes infinite speed. In order to bring finite wave-speed, below we try to derive non-Fourier models using different approaches.

2.1 Phase-Lag Approach

According to Tzou [60], the constitutive equations can be viewed as the cause-effect phenomena in transport processes. For example, Stoke's law of viscosity, where the shear stress can be viewed as the cause for the fluid motion and the shear strain rate as its effect. Similarly, Fourier's law of heat conduction in Eq. (1.1), where the heat flux vector $\mathbf{q}$ can be observed as the cause for the heat flow and the temperature gradient $\boldsymbol{\nabla}\theta$ as its effect. In these examples, the cause and the effect are instantaneous with no time lag and therefore can interchange their positions. This implies that the temperature gradient can also be viewed as the cause where the heat flux vector becomes the effect in the above example. A simultaneity in the positions of the cause and the effect annuls their physical significance. However, should a time lag between the heat flux vector and the temperature gradient be introduced (Tzou [61]), then the cause and the effect can be separated from each other, providing the concept of cause-effect a physical meaning. In this framework, between the two terms, the heat flux vector and the temperature gradient, whichever lags behind becomes the effect. Since, the precedence of either of the two can't be set beforehand, two time (phase) lags need to be introduced in the most general sense. In these terms, Tzou (1993-95) builds the model of *dual phase-lag*. These phase lags, or delay times, are called the relaxation times, providing basis for short-time responses.

Tzou [61] introduces the time lag by writing the constitutive equation for heat flow as

$$\boldsymbol{q}(\boldsymbol{x}, t + \tau_q) = -k\boldsymbol{\nabla}\theta(\boldsymbol{x}, t), \tag{2.4}$$

where τ_q is a *relaxation time*. Performing a Taylor expansion with respect to t leads to

the Cattaneo-Vernotte (CV) wave model:

$$\tau_q \frac{\partial \boldsymbol{q}}{\partial t}(\boldsymbol{x},t) + \boldsymbol{q}(\boldsymbol{x},t) \cong -k\boldsymbol{\nabla}\theta(\boldsymbol{x},t). \tag{2.5}$$

The addition of relaxation time τ_q points to a finite wave speed c; they are related by $\tau_q = \frac{\alpha}{c^2}$, where $\alpha = k/\gamma$ is the thermal diffusivity. Taking divergence of the CV wave model in Eq. (2.5), and then using the energy equation in Eq. (2.1) and the first law of thermodynamics in Eq. (2.2), it leads to Cattaneo's hyperbolic equation:

$$\frac{\partial^2 \theta}{\partial t^2} + \frac{1}{\tau_q}\frac{\partial \theta}{\partial t} = c^2 \nabla^2 \theta. \tag{2.6}$$

For the CV wave model in Eq. (2.5), the heat flux vector $\boldsymbol{q}$ lags behind the temperature gradient $\boldsymbol{\nabla}\theta$ by a relaxation time τ_q. This fact makes sure that the temperature gradient always remains the cause and the heat flux vector its effect. To remedy this, Tzou (1995) brings *dual-phase-lag model* that allows either of the two, $\boldsymbol{q}$ and $\boldsymbol{\nabla}\theta$, to precede each other, implying that either one could become the cause or the effect. The constitutive equation for the *dual-phase-lag model* is

$$\boldsymbol{q}(\boldsymbol{x}, t+\tau_q) = -k\boldsymbol{\nabla}\theta(\boldsymbol{x}, t+\tau_\theta), \tag{2.7}$$

where τ_θ and τ_q are the phase-lag of the temperature gradient and the heat flux vector, respectively. For the case, $\tau_\theta > \tau_q$, the heat flux vector is the cause and the temperature gradient is the effect, whereas if $\tau_\theta < \tau_q$, then the heat flux vector becomes the effect and the temperature gradient becomes the cause. A first-order Taylor expansion leads to the dual-phase-lag model:

$$\tau_q \frac{\partial \boldsymbol{q}}{\partial t}(\boldsymbol{x},t) + \boldsymbol{q}(\boldsymbol{x},t) \cong -k\boldsymbol{\nabla}\theta(\boldsymbol{x},t) - k\tau_\theta \frac{\partial \boldsymbol{\nabla}\theta}{\partial t}(\boldsymbol{x},t), \tag{2.8}$$

Taking divergence of this dual-phase-lag model, substituting the energy equation in Eq. (2.1) and using the first law of thermodynamics in Eq. (2.2), we obtain a non-Fourier partial differential equation of the *Jeffreys-type* by assuming constant thermal properties,

$$\frac{\partial^2 \theta}{\partial t^2} + \frac{1}{\tau_q}\frac{\partial \theta}{\partial t} = c^2 \nabla^2 \theta + \frac{k\,\tau_\theta/\tau_q}{\gamma}\nabla^2 \frac{\partial \theta}{\partial t}, \tag{2.9}$$

where k is the thermal conductivity, and $c^2 = k/\gamma\tau_q$.

Other than determining the cause and the effect in the heat transport process, the motivation also comes from the similar nature of equations arising from the models developed to capture two different heat mechanism methods – Phonon-electron interaction and Phonon Scattering. We will describe these two methods in the following subsections.

2.1.1 Phonon-electron interaction

Heat transport requires "sufficient" number of collisions among energy carriers, so that a meaningful statistical ensemble space can be created by defining the mean free path and the mean free time. The energy carriers in metals include phonons and electrons. A phenomenological model of heat transport can be achieved by assuming the interaction between phonons and electrons in metals. Kaganov et al [62] and Anisimov et al [63] developed a two-step model for this interaction between phonons and electron gas. A phonon is the quantum of energy obtained by quantization of the energy of a lattice vibration. It is analogous in the name with photon of the electromagnetic wave. The electron gas, or more specifically, free electron Fermi gas, is a gas of free electrons subject to Pauli exclusion principle. Many physical properties of a metal can be explained by the free electron model, in which the valence electrons of the constituent atoms become conduction electrons, moving freely through the volume of metal. According to the two-step model of phonon-electron interaction, the heating mechanism involves excitation of the electron gas by the externally supplied photons as the first step, such as the photons from an intensified laser. This increases the temperature of the electron gas. In the second step, the metal lattice is allowed to be heated through phonon-electron interaction in short times. This phenomenological phonon-electron two-step interaction model was given the quantum mechanical and statistical basis by Qiu and Tien [64].

Qiu and Tien [65] consider the excitation of electron gas and the metal-lattice heating as two steps, where the exchange of energy between phonons and the electron gas occurs through a coupling factor G. In mathematical terms,

$$\gamma_e \frac{\partial \theta_e}{\partial t} = \boldsymbol{\nabla} \cdot (K \boldsymbol{\nabla} \theta_e) - G\,(\theta_e - \theta_l)\,, \qquad \textit{excitation of the electron gas}, \tag{2.10a}$$

$$\gamma_l \frac{\partial \theta_l}{\partial t} = G\,(\theta_e - \theta_l)\,, \qquad \textit{heating of the metal-lattice}, \tag{2.10b}$$

where θ refers to the temperature, γ represents the volumetric heat capacity, K refers to the thermal conductivity of the electron gas, and subscripts e and l stand for the electron

gas and the metal lattice, respectively. The second step neglects the heat conduction through the metal lattice. Substituting θ_e from Eq. (2.10b) into Eq. (2.10a) yields,

$$\frac{\partial^2 \theta_l}{\partial t^2} + \left(\frac{G(\gamma_e + \gamma_l)}{\gamma_e \gamma_l}\right) \frac{\partial \theta_l}{\partial t} = \left(\frac{KG}{\gamma_e \gamma_l}\right) \nabla^2 \theta_l + \frac{K}{\gamma_e} \nabla^2 \frac{\partial \theta_l}{\partial t} \tag{2.11}$$

Similarly, substituting θ_l from Eq. (2.10a) into Eq. (2.10b) yields,

$$\frac{\partial^2 \theta_e}{\partial t^2} + \left(\frac{G(\gamma_e + \gamma_l)}{\gamma_e \gamma_l}\right) \frac{\partial \theta_e}{\partial t} = \left(\frac{KG}{\gamma_e \gamma_l}\right) \nabla^2 \theta_e + \frac{K}{\gamma_e} \nabla^2 \frac{\partial \theta_e}{\partial t} \tag{2.12}$$

Clearly, both equations Eqs. (2.11) and (2.12), governing the lattice and electron temperature, respectively, have the same identical form as obtained above in the non-Fourier heat equation of the Jeffreys-type in Eq. (2.39). Therefore, the validity of the heat equation of the Jeffreys-type is further justified and consolidated.

2.1.2 Phonon Scattering

Aforementioned phonon-electron interaction plays major role for the heat transport process in metals, whereas phonons are dominant heat carriers in insulators and semiconductors, thereby, giving rise to phonon collision/scattering as the major mechanism for the heat transport process. This domination of collision process imparts the phonon states a hydrodynamic (fluid) character with the quasiparticle occupation probability distribution $f(\boldsymbol{k}, \boldsymbol{x}, t)$, where $\boldsymbol{k}$ and $\boldsymbol{x}$ denote the mean wave vector and position vector of the phonon wave packets. The time evolution of $f(\boldsymbol{k}, \boldsymbol{x}, t)$ is governed by the Boltzmann transport equation,

$$\frac{\partial f}{\partial t} + \boldsymbol{v_k} \cdot \boldsymbol{\nabla} f = \mathcal{C}\left[f\right], \tag{2.13}$$

where $\boldsymbol{v_k}$ corresponds to group velocity of phonon wave packets and $\mathcal{C}$ is the collision operator. $\mathcal{C}$ can be further divided into two parts, $\mathcal{C} = \mathcal{N} + \mathcal{R}$, where $\mathcal{N}$ refers to momentum conserving normal-process collision operator and $\mathcal{R}$ corresponds to other processes, e.g. momentum non-conserving umklapp scattering, mass-fluctuation scattering, etc. For the pure phonon field, not influenced by any elastic field subject to mechanical stress, and neglecting the contribution from the electron gas in conducting heat, Guyer and Krumhansl [66] developed the solution of linearized version of the Boltzmann transport

equation in Eq. (2.13) in terms of the eigenvector of the normal-process collision operator $\mathcal{N}$. Assuming $\mathcal{N} \gg \mathcal{R}$, the development leads to two macroscopic equations,

$$\gamma_p \frac{\partial \theta}{\partial t} + \boldsymbol{\nabla} \cdot \boldsymbol{q} = 0, \tag{2.14a}$$

$$\frac{\partial \boldsymbol{q}}{\partial t} + \frac{c^2 \gamma_p}{3} \boldsymbol{\nabla} \theta + \frac{1}{\tau_R} \boldsymbol{q} = \frac{\tau_N c^2}{5} \left[\nabla^2 \boldsymbol{q} + 2 \boldsymbol{\nabla} \left(\boldsymbol{\nabla} \cdot \boldsymbol{q} \right) \right], \tag{2.14b}$$

where c is the average speed of phonons, γ_p is volumetric heat capacity for phonons, τ_R denotes relaxation time for the umklapp process $\mathcal{R}$ and τ_N is the relaxation time for normal process $\mathcal{N}$.

Substituting the heat flux vector term from Eq. (2.14a) in the result obtained after taking the divergence of Eq. (2.14b),

$$\frac{\partial^2 \theta}{\partial t^2} + \frac{1}{\tau_R} \frac{\partial \theta}{\partial t} = \frac{c^2}{3} \nabla^2 \theta + \frac{3 c^2 \tau_N}{5} \nabla^2 \frac{\partial \theta}{\partial t}. \tag{2.15}$$

It is clear that, Eq. (2.15) has the same form as phonon-electron interaction model. The similarity of the models for both mechanisms of heat transfer motivated Tzou [5] to introduce the concept of generalized phase-lag behavior, which has already been discussed above.

2.2 Effective Thermal Conductivity

Joseph and Preziosi [2], based upon the insights of Gurtin and Pipkin [67] and Nunziato [68], introduced the concept of effective thermal conductivity and effective heat capacity to take into account the non-Fourier behavior.

Taking the fading memory approach[1] of Coleman and Noll [70] for simple materials, Gurtin and Pipkin showed that *the heat flux vector, like the entropy, is determined by the functional for the free-energy.* They first assumed that the response of the material at each point $\boldsymbol{x}$ is characterized by three functionals Ψ, N and $\boldsymbol{Q}$, where Ψ is a smooth scalar-valued function and N and $\boldsymbol{Q}$ are continuous. The functionals are also independent of the point $\boldsymbol{x}$, thereby assuming that the material is homogeneous. These response functionals give the instantaneous values of the free energy $\psi = \psi(t)$, entropy $\eta = \eta(t)$

[1] The recent history of temperature and deformations have more effect on the present values of stress, entropy, heat flux and free energy than their distant past history [69].

and heat flux vector $\boldsymbol{q} = \boldsymbol{q}(\boldsymbol{t})$, provided that the temperature $\theta = \theta(t)$ and the summed histories of temperature $\bar{\theta}^t$ and temperature gradient $\bar{\boldsymbol{g}}^t$, where $\boldsymbol{g} = \boldsymbol{\nabla}\theta$, be known at $\boldsymbol{x}$. Also, $\theta, \boldsymbol{\nabla}\theta \in {L_h}^2$ space. The values are given by

$$\begin{aligned} \psi &= \Psi\left(\theta, \bar{\theta}^t, \bar{\boldsymbol{g}}^t\right), \\ \eta &= N\left(\theta, \bar{\theta}^t, \bar{\boldsymbol{g}}^t\right), \\ \boldsymbol{q} &= \boldsymbol{Q}\left(\theta, \bar{\theta}^t, \bar{\boldsymbol{g}}^t\right). \end{aligned} \tag{2.16}$$

The summed histories $\bar{\theta}^t$ and $\bar{\boldsymbol{g}}^t$ on $[0, \infty)$ are defined by

$$\begin{aligned} \bar{f}^t(s) &= \int_0^s f^t(\mu) d\mu \qquad s \in [0, \infty) \\ &= \int_{t-s}^t f^t(\tau) d\tau, \\ \text{where,} \quad f^t(s) &= f(t-s), \end{aligned} \tag{2.17}$$

and $\bar{f}^t$ corresponds to either $\bar{\theta}^t$ or $\bar{\boldsymbol{g}}^t$. Norm $\|\cdot\|_{{L_h}^2}$ of a measurable scalar or vector-valued function f on $[0, \infty)$, where $f \in$ weighted ${L_h}^2$ space, is defined by

$$\|f\|_{{L_h}^2}^2 = \int_0^\infty |f(s)|^2 h(s) ds, \tag{2.18}$$

where h be a positive, continuous, monotone decreasing function, also termed as *influence function*. This determines the memory fading rate with $s^2 h(s)$ being integrable in s on $[0, \infty)$. Also, let us assume that H denote the set of all measurable scalar-valued and vector-valued functions f on $[0, \infty)$, with $\|f\|_{{L_h}^2} < \infty$. Thus, H can be given the structure of Hilbert space. For a fixed point $\boldsymbol{x}$, the *thermodynamic process* means an ordered array $[\theta(\cdot), \boldsymbol{g}(\cdot), \psi(\cdot), \eta(\cdot), \boldsymbol{q}(\cdot)]$, where $[\theta(\cdot), \boldsymbol{g}(\cdot)]$ is an *admissible* pair and $\psi(\cdot), \eta(\cdot), \boldsymbol{q}(\cdot)$ are defined by the constitutive relations (2.16). The admissible pair means:

(i) $\theta(\cdot)$ is continuous and piecewise smooth;

(ii) $\boldsymbol{g}(\cdot)$ is piecewise continuous;

(iii) $\theta \in \mathbb{R}^+$, $\theta^t, \bar{\theta}^t, \boldsymbol{g}^t, \bar{\boldsymbol{g}}^t \in H$ for all $t \in \mathbb{R}$.

The common domain of the three response functionals is $\mathbb{R}^+ \times H \times H$.[2] Ψ is smooth, therefore, it possesses partial derivatives:

[2] Actually, the common domain is $\mathbb{R}^+ \times H^{++} \times H$, where H^{++} denotes the cone of essentially strictly positive monotone increasing functions in H.

(i) $D_\theta \Psi\left(\theta, \bar{\theta}^t, \bar{\boldsymbol{g}}^t\right) \in \mathbb{R}$ with respect to θ keeping $\bar{\theta}^t$ and $\bar{\boldsymbol{g}}^t$ fixed,

(ii) $\delta_1 \Psi\left(\theta, \bar{\theta}^t, \bar{\boldsymbol{g}}^t\right) : H \to \mathbb{R}$ with respect to $\bar{\theta}^t$ keeping θ and $\bar{\boldsymbol{g}}^t$ fixed, and

(iii) $\delta_2 \Psi\left(\theta, \bar{\theta}^t, \bar{\boldsymbol{g}}^t\right) : H \to \mathbb{R}$ with respect to $\bar{\boldsymbol{g}}^t$ keeping θ and $\bar{\theta}^t$ fixed.

Also, we define $J_{\boldsymbol{g}} \Psi(\cdot) \in \mathbb{R}^3$ by $J_{\boldsymbol{g}} \Psi(\cdot) \cdot \boldsymbol{\upsilon} = \delta_2 \Psi(\cdot)\left(\boldsymbol{\upsilon}^c\right)$, for every $\boldsymbol{\upsilon} \in \mathbb{R}^3$, where $\boldsymbol{\upsilon}^c \in H$ is a constant function with value $\boldsymbol{\upsilon}$.

Using a sequence of admissible pairs, as stated above, Gurtin and Pipkin showed that *the response functional* Ψ determines N through the entropy relation $N = -D_\theta \Psi$ and $\boldsymbol{Q}$ through the heat flux relation $\boldsymbol{Q} = -\theta J_{\boldsymbol{g}} \Psi$. They also developed the linearized theory of the constitutive relations by exploiting the symmetry of the isotropic materials. By linearized theory, it was meant that an admissible pair $[\theta(\cdot), \boldsymbol{g}(\cdot)]$ close to θ_0 can be considered in the sense that

$$\sup_{-\infty < t < t_0} \{|\theta(t) - \theta_0| + |\boldsymbol{g}(t)|\} < \delta,$$

where $\theta_0 > 0$ is a constant temperature field and δ is small. After linearization, the heat flux vector $\boldsymbol{q}(\boldsymbol{x}, t)$ and the internal energy $e(\boldsymbol{x}, t)$ can be expressed by

$$\boldsymbol{q}(\boldsymbol{x}, t) = -\int_0^\infty \mathcal{Q}(s) \boldsymbol{\nabla} \theta(\boldsymbol{x}, t - s) ds, \tag{2.19}$$

$$e(\boldsymbol{x}, t) = b + \gamma \theta(\boldsymbol{x}, t) + \int_0^\infty \mathcal{F}(s) \theta(\boldsymbol{x}, t - s) ds, \tag{2.20}$$

where b and γ are constants. This becomes possible only if $s^2 \mathcal{Q}(s)$ and $s^2 \mathcal{F}(s)$, both, tend to finite limit as $s \to \infty$. Both $\mathcal{Q}(s)$ and $\mathcal{F}(s)$ are differentiable scalar-valued functions on $[0, \infty)$ with $\mathcal{Q}(\infty) = 0$, $\mathcal{Q}(0)$ finite and $\mathcal{F}(\infty) = 0$, $\mathcal{F}(0)$ finite. Also, $\mathcal{Q}(s)$ and $\mathcal{F}(s)$ are named as the *heat-flux relaxation function* and the *energy relaxation function*, respectively. They are also known as the heat-flux kernel and the energy kernel. $\mathcal{Q}(0)$ is termed as *the instantaneous conductivity*.

Let us consider the magnitude of the heat flux vector in the linearized expression

(2.19),

$$
\begin{aligned}
|\boldsymbol{q}(\boldsymbol{x},t)|^2 &= \int_0^\infty |\mathcal{Q}(s)|^2 |\boldsymbol{\nabla}\theta(\boldsymbol{x},t-s)|^2 ds \\
&= \int_0^\infty |\mathcal{Q}(s)|^2 |\boldsymbol{g}^t(\boldsymbol{x},s)|^2 ds \\
&= \int_0^\infty \Big|\frac{\mathcal{Q}(s)}{\sqrt{h(s)}}\Big|^2 |\boldsymbol{g}^t(\boldsymbol{x},s)\sqrt{h(s)}|^2 ds \\
&\qquad \textit{where } h \textit{ be the influence function on} [0,\infty), \\
&\leq \int_0^\infty \Big|\frac{\mathcal{Q}(s)}{\sqrt{h(s)}}\Big|^2 ds \quad \int_0^\infty \Big|\boldsymbol{g}^t(\boldsymbol{x},s)\sqrt{h(s)}\Big|^2 ds \\
&\qquad \textit{(from Cauchy-Schwarz inequality)}, \\
&= \int_0^\infty \Big|\frac{\mathcal{Q}(s)}{\sqrt{h(s)}}\Big|^2 ds \quad \int_0^\infty \Big|\boldsymbol{g}^t(\boldsymbol{x},s)\Big|^2 h(s) ds \\
&= \Big(\int_0^\infty \Big|\frac{\mathcal{Q}(s)}{\sqrt{h(s)}}\Big|^2 ds \Big) \quad \|\boldsymbol{g}^t\|^2_{{L_h}^2}; \quad \boldsymbol{g}^t \in H.
\end{aligned}
$$

This means $|\boldsymbol{q}(\boldsymbol{x},t)|^2 < \infty$ only if

$$
\int_0^\infty \Big|\frac{\mathcal{Q}(s)}{\sqrt{h(s)}}\Big|^2 ds < \infty, \quad or, \quad \int_0^\infty \Big|\frac{\mathcal{Q}(s)}{h(s)}\Big|^2 h(s) ds < \infty, \quad or, \quad \|\tilde{\mathcal{Q}}\|_{{L_h}^2} < \infty, \tag{2.21}
$$

where $\tilde{\mathcal{Q}}$ be a function on $[0,\infty)$ defined as $\tilde{\mathcal{Q}}(s) = \mathcal{Q}(s)/h(s)$. The condition, $\tilde{\mathcal{Q}} \in {L_h}^2$ space, demands that no Dirac delta type of functions should constitute the heat-flux relaxation function $\mathcal{Q}$.

Taking divergence of equation (2.19), differentiating equation (2.20) with respect to time t and substituting them in the energy equation (2.1), we obtain

$$
\gamma \frac{\partial \theta}{\partial t}(\boldsymbol{x},t) + \int_0^\infty \mathcal{F}(s) \frac{\partial \theta}{\partial t}(\boldsymbol{x},t-s)\, ds = \int_0^\infty \mathcal{Q}(s)\, \nabla^2 \theta(\boldsymbol{x},t-s)\, ds. \tag{2.22}
$$

Now taking partial derivative of equation (2.22) and integrating the integrals by parts with respect to time t, we get

$$
\gamma\, \frac{\partial^2 \theta}{\partial t^2}(\boldsymbol{x},t) + \mathcal{F}(0)\, \frac{\partial \theta}{\partial t}(\boldsymbol{x},t) + \int_0^\infty \mathcal{F}(s)\, \frac{\partial \theta}{\partial t}(\boldsymbol{x},t-s)\, ds \tag{2.23}
$$

$$
= \mathcal{Q}(0)\, \nabla^2 \theta(\boldsymbol{x},t) \int_0^\infty \mathcal{Q}(s)\, \nabla^2 \theta(\boldsymbol{x},t-s)\, ds. \tag{2.24}
$$

Classifying the partial differential equation (2.23) by determining the discriminant $\Delta = \gamma\mathcal{Q}(0); \quad \Delta > 0$, we find that the equation is hyperbolic with constant wave speed $c = \sqrt{\mathcal{Q}(0)/\gamma}$. When the heat flux relaxation function and the energy relaxation function, both, are represented by exponentials as

$$\mathcal{Q}(s) = \mathcal{Q}(0)e^{-s/\tau_1}, \quad \mathcal{F}(s) = \mathcal{F}(0)e^{-s/\tau_2}, \tag{2.25}$$

where τ_1, τ_2 are constants, then the linearized expressions (2.19), (2.20) and the energy equation (2.1) give

$$\gamma\,\frac{\partial^3\theta}{\partial t^3}(\boldsymbol{x},t) + \left[\mathcal{F}(0) + \frac{\gamma}{\tau_1} + \frac{\gamma}{\tau_2}\right]\frac{\partial^2\theta}{\partial t^2}(\boldsymbol{x},t) + \left[\frac{\mathcal{F}(0)}{\tau_1} + \frac{\gamma}{\tau_1\tau_2}\right]\frac{\partial\theta}{\partial t}(\boldsymbol{x},t) \tag{2.26}$$

$$= \mathcal{Q}(0)\,\nabla^2\frac{\partial\theta}{\partial t}(\boldsymbol{x},t) + \frac{\mathcal{Q}(0)}{\tau_2}\,\nabla^2\theta(\boldsymbol{x},t). \tag{2.27}$$

Likewise equation (2.23), this equation (2.26) is also hyperbolic with constant wave speed $c = \sqrt{\mathcal{Q}(0)/\gamma}$. This equation becomes similar to the non-Fourier equation of the Jeffreys-type (2.39),

$$\frac{\partial^2\theta}{\partial t^2} + \frac{1}{\tau_1}\frac{\partial\theta}{\partial t} = \frac{\mathcal{Q}(0)/\mathcal{F}(0)}{\tau_2}\,\nabla^2\theta + \frac{\mathcal{Q}(0)}{\mathcal{F}(0)}\,\nabla^2\frac{\partial\theta}{\partial t}, \tag{2.28}$$

when the constant $\gamma = 0$.

Nunziato [68] changed the domain of the response functionals in Eq. (2.16) such that the free energy, the entropy and the heat flux not only depend upon the past histories but the instantaneous values as well. Nunziato considered the fixed scalar influence function $h(s)$ on $(0,\infty)$ decaying to zero as $s \to \infty$ with a decay rate fast enough to be square-integrable over $(0,\infty)$. The norm of the measurable ordered pair $\Lambda^t \equiv (\theta^t, \boldsymbol{g}^t)$ was defined as

$$\|\Lambda^t\|^2 = |\Lambda^t(0)|^2 + \int_0^\infty |\Lambda^t(s)|^2\,h(s)^2\,ds,$$

where $|\Lambda^t(0)| = \Big(\theta(\boldsymbol{x},t), \boldsymbol{g}(\boldsymbol{x},t)\Big)$ contributes to the instantaneous value of the heat flux and the integral part contributes to the past history of the heat flux. Also, the set of all measurable ordered pairs Λ^t with finite norm forms a Hilbert space. This allows Dirac delta distribution to be a part of the heat-flux kernel $\mathcal{Q}$ as

$$\mathcal{Q}(s) = k_1\delta(s) + \mathcal{Q}_2(s), \tag{2.29}$$

where k_1 is a constant termed as the *effective conductivity* and $\mathcal{Q}_2$ is that part of heat-flux kernel which has similar properties as chosen in the description in Eq. (2.21). This changes the expression in Eq. (2.19) for the heat-flux vector as

$$\boldsymbol{q}(\boldsymbol{x},t) = -k_1 \boldsymbol{\nabla}\theta(\boldsymbol{x},t) - \int_0^\infty \mathcal{Q}_2(s)\boldsymbol{\nabla}\theta(\boldsymbol{x},t-s)ds. \tag{2.30}$$

Energy kernel in Eq. (2.20) can also be written as

$$e(\boldsymbol{x},t) = b + \int_0^\infty \mathcal{E}(s)\theta(\boldsymbol{x},t-s)ds, \tag{2.31}$$

by taking,

$$\mathcal{E}(s) = \gamma_1\delta(s) + \mathcal{E}_2(s), \tag{2.32}$$

where $\gamma_1 = \gamma$ is a constant termed as the effective capacity and $\mathcal{E} = \mathcal{F}$. Joseph and Preziosi [2] also defined two other constants, $\gamma_2 = \int_0^\infty \mathcal{E}_2(s)ds$, termed as the *elastic capacity* and $k_2 = \int_0^\infty \mathcal{Q}_2(s)ds$, termed as the *elastic conductivity*. If the heat-flux vector and the internal energy be described by Eqs. (2.30) and (2.31), then Eq. (2.22) changes to *Nunziato's equation*:

$$\gamma\frac{\partial\theta}{\partial t}(\boldsymbol{x},t) + \int_0^\infty \mathcal{E}_2(s)\frac{\partial\theta}{\partial t}(\boldsymbol{x},t-s)ds = k_1\nabla^2\theta(\boldsymbol{x},t) + \int_0^\infty \mathcal{Q}_2(s)\nabla^2\theta(\boldsymbol{x},t-s)ds. \tag{2.33}$$

which is a generalized version of the Jeffreys-type. Here, *thermal conductivity* is also defined as the sum of effective conductivity k_1 and elastic conductivity k_2, or, $k = k_1 + k_2$.

The Jeffreys-type equation shows both diffusion and wave like behavior, whose physical meaning can be understood by qualitatively explaining the fast modes (responses) and the slow modes depending upon the time scales.[3] Assuming phonons and free electrons as energy carriers for the heat conduction, a 'large' number of collisions among the heat carriers must take place to make statistical sense of the continuum properties like stress, entropy, heat flux etc. The collisions result into thermal resistance and a relaxation time τ_0 can be defined. This is *associated with the average communication time*

[3] The response or modes of the material decay at different rates. The modes that decay very fast, $O(10^{-13})$ s, continue to affect the heat transfer, even though they have decayed completely. These fast modes produce diffusion with an effective conductivity $k^* = \int_0^{s^*} \mathcal{Q}(s)ds$ where $\mathcal{Q}$ be the heat-flux kernel and $s^* = O(10^{-13})$ s.

between the collisions for the commencement of resistive flows so that a local thermodynamic equilibrium (Rohsenow et al [71]) can be achieved. Different collision times for phonon-electron (longest $\sim 10^{-11}$ s. at room temperature), phonon-phonon ($\sim 10^{-13}$ s.) and free electron interactions (shortest $\sim 10^{-13}$ s.) give rise to different relaxation times. Imperfections and impurities in the material reduce these relaxation times.

These different unknown relaxation times lead to an unknown mean relaxation time. If we have finite wave speed determined by $c = \sqrt{\mathcal{Q}(0)/\gamma}$ as described above for finite $\mathcal{Q}(0)$, and the thermal conductivity $k = \int_0^\infty \mathcal{Q}(s)ds$, then a mean relaxation time can be computed as $\tau = k/\mathcal{Q}(0)$.

Now, we will qualitatively try to constitute the constitutive equation (2.30) with the help of a schematic diagram of heat-flux relaxation function based upon different relaxation times.

Joseph and Preziosi *assumed* a fast relaxation followed by a slow relaxation, something like Fig. 2.1. The heat-flux relaxation function can be written as

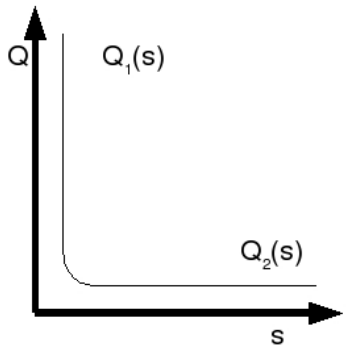

Figure 2.1: *Example of heat-flux relaxation function with a fast and a slow relaxation.*

$$\mathcal{Q}(s) = \mathcal{Q}_1(s) + \mathcal{Q}_2(s),$$

where s varies from $[0, \infty)$. Based upon this, the thermal conductivity becomes

$$k = k_1 + k_2, \quad \text{with} \quad k_1 = \int_0^\infty \mathcal{Q}_1(s)ds \approx \int_0^{\tau_1} \mathcal{Q}_1(s)ds \quad \text{and} \quad k_2 = \int_0^\infty \mathcal{Q}_2(s)ds,$$

where τ_1 is the time after which the fast mode almost decays down to zero.

A small time s_0, $0 < s_0 \leq \tau_1$, can be chosen such that $\frac{\mathcal{Q}_1(s_0)}{\mathcal{Q}_2(s_0)} \ll 1$ and $\mathcal{Q}_2(s_0) \approx \mathcal{Q}_2(0)$. For $t > s_0$, $\mathcal{Q}_1(s)$ almost becomes equal to zero, therefore,

$$\begin{aligned}
\int_0^\infty \mathcal{Q}_1(s)\boldsymbol{\nabla}\theta(\boldsymbol{x}, t-s)ds &= \int_0^{s_0} \mathcal{Q}_1(s)\boldsymbol{\nabla}\theta(\boldsymbol{x}, t-s)ds + \int_{s_0}^\infty \mathcal{Q}_1(s)\boldsymbol{\nabla}\theta(\boldsymbol{x}, t-s)ds \\
&\approx \int_0^{s_0} \mathcal{Q}_1(s)\boldsymbol{\nabla}\theta(\boldsymbol{x}, t-s)ds \\
&\approx \boldsymbol{\nabla}\theta(\boldsymbol{x}, t)\int_0^{s_0} \mathcal{Q}_1(s)ds \\
&\qquad \Big(\text{ if } s_0 \text{ is small, } t-s \sim t,\ \boldsymbol{\nabla}\theta \text{ remains unchanged in } (0, s_0) \Big) \\
&\approx \boldsymbol{\nabla}\theta(\boldsymbol{x}, t)\int_0^{\infty} \mathcal{Q}_1(s)ds \\
&= \boldsymbol{\nabla}\theta(\boldsymbol{x}, t)k_1.
\end{aligned}$$

Therefore, as per the definition of the the heat flux vector (2.19),

$$\begin{aligned}
\boldsymbol{q} &= -\int_0^\infty \left(\mathcal{Q}_1(s) + \mathcal{Q}_2(s)\right)\boldsymbol{\nabla}\theta(\boldsymbol{x}, t-s)ds \\
&\approx -k_1\boldsymbol{\nabla}\theta(\boldsymbol{x}, t) - \int_0^\infty \mathcal{Q}_2(s)\boldsymbol{\nabla}\theta(\boldsymbol{x}, t-s)ds.
\end{aligned} \tag{2.34}$$

Here, a mean relaxation time τ can be introduced that decides whether the relaxation of $\mathcal{Q}_2(s)$ is fast or slow,

$$\tau = k_2/\mathcal{Q}_2(0). \tag{2.35}$$

and if $k_2 \gg k_1$, then $\tau = k/\mathcal{Q}_2(0)$, where k_2 refers to the elastic conductivity and k is the thermal conductivity. Based upon Fig. 2.1 and the above discussion, it seems fair to represent the fast modes by a Dirac measure leading to $\mathcal{Q}_1(s) = k_1\delta(s)$. This discussion of fast and slow relaxations justifies the heat-flux kernel $\mathcal{Q}$ in Eq. (2.29) and the heat-flux vector $\boldsymbol{q}$ in Eq. (2.30).

If we express $\mathcal{Q}_2$ in exponential terms such as $\mathcal{Q}_2(s) = \frac{k_2}{\tau}e^{-s/\tau}$, where the relaxation time τ is determined by Eq. (2.35), then by substituting $s = 0$ in the exponential expression we obtain $\tau = k_2/Q_2(0)$. Finally we use the heat-flux kernel equation in Eq. (2.29) to obtain

$$\mathcal{Q}(s) = k_1\delta(s) + \frac{k_2}{\tau}e^{-s/\tau}. \tag{2.36}$$

Substituting the expression for $\mathcal{Q}$ in Eq. (2.36) in the heat-flux vector expression in

Eq. (2.30) and changing the variable s to $t - t'$, we obtain

$$\boxed{\boldsymbol{q}(\boldsymbol{x},t) = -k_1 \boldsymbol{\nabla}\theta(\boldsymbol{x},t) - \frac{k_2}{\tau}\int_{-\infty}^{t} \exp - \left[\frac{t-t'}{\tau}\right] \boldsymbol{\nabla}\theta(\boldsymbol{x},t')dt'}. \tag{2.37}$$

Equation (2.37) is the integrated form of the *heat-flux equation of the Jeffreys type*, which is:

$$\tau \frac{\partial \boldsymbol{q}}{\partial t}(\boldsymbol{x},t) + \boldsymbol{q}(\boldsymbol{x},t) = -k\boldsymbol{\nabla}\theta(\boldsymbol{x},t) - \tau k_1 \frac{\partial \boldsymbol{\nabla}\theta}{\partial t}(\boldsymbol{x},t). \tag{2.38}$$

This has the same form as the dual-phase-lag model in Eq. (2.8) obtained from phase-lag approach with $\tau = \tau_q$ and $k_1 = k\tau_\theta/\tau_q$. Here also, taking the divergence of Eq. (2.37) and then using the energy equation in Eq. (2.1) and the first law of thermodynamics in Eq. (2.2), we obtain similar Jeffreys-type equation as obtained in Eq. (2.9):

$$\boxed{\frac{\partial^2 \theta}{\partial t^2}(\boldsymbol{x},t) + \frac{1}{\tau}\frac{\partial \theta}{\partial t}(\boldsymbol{x},t) = c^2\nabla^2\theta(\boldsymbol{x},t) + \frac{k_1}{\gamma}\nabla^2\frac{\partial \theta}{\partial t}(\boldsymbol{x},t)}, \tag{2.39}$$

where the thermal conductivity k is the sum of the effective conductivity k_1 and the elastic conductivity k_2, i.e., $k = k_1 + k_2$, and $c^2 = k/\gamma\tau$.

For the case of the effective conductivity $k_1 = 0$, and $k = k_2$, Eq. (2.38) reduces to the *Cattaneo's equation*:

$$\tau \frac{\partial \boldsymbol{q}}{\partial t}(\boldsymbol{x},t) + \boldsymbol{q}(\boldsymbol{x},t) = -k\boldsymbol{\nabla}\theta(\boldsymbol{x},t). \tag{2.40}$$

This is same as CV wave model in Eq. (2.5) with $\tau = \tau_q$. Integrating Cattaneo's equation in Eq. (2.40) with respect to time $t' \in (-\infty, t)$, keeping $\boldsymbol{x}$ fixed, we obtain *Cattaneo's heat-flux law*:

$$\boldsymbol{q}(\boldsymbol{x},t) = -\frac{k}{\tau}\int_{-\infty}^{t} \exp - \left[\frac{t-t'}{\tau}\right] \boldsymbol{\nabla}\theta(\boldsymbol{x},t')dt'. \tag{2.41}$$

Taking divergence of Cattaneo's equation in Eq. (2.40) and using the energy equation in Eq. (2.1) and the first law of thermodynamics in Eq. (2.2), we obtain a telegraph equation, which we term as *Cattaneo's hyperbolic equation*:

$$\frac{\partial^2 \theta}{\partial t^2} + \frac{1}{\tau}\frac{\partial \theta}{\partial t} = c^2\nabla^2\theta. \tag{2.42}$$

This is the same equation in Eq. (2.6) as obtained from the phase-lag approach. This hyperbolic equation transmits waves of temperature with speed c coupled with attenuation of waves as the result of relaxation and the presence of temperature gradients. Obviously, when c becomes infinite, everything reduces to Fourier's behavior.

2.3 A Thermodynamic Discussion

A third approach which leads to similar equations for the heat-flux law as those obtained by Joseph and Perziosi [2] and Tzou [60, 61] is based upon thermodynamics. All of the constitutive equations for the heat flux discussed above must obey the second law of thermodynamics, i.e., the entropy production rate is always non-negative for all thermodynamic processes.

According to the basic assumption of thermodynamics, the kinematic variables $\hat{\boldsymbol{\gamma}}$ and one additional independent scalar parameter is sufficient to determine the specific internal energy u. This means a *caloric equation of state* can be defined as

$$u = u\left(s, \hat{\boldsymbol{\gamma}}\right),$$

where s is the specific entropy and $\hat{\boldsymbol{\gamma}}$ represents the intensive set of kinematic variables. Also, the shape change of the material can be captured by the deformation in an infinitesimal neighborhood around the particle $\boldsymbol{X}$ of the reference configuration. This deformation can be characterized by the deformation gradient $\boldsymbol{F} = \frac{\partial \boldsymbol{x}}{\partial \boldsymbol{X}}$, where $\boldsymbol{x}$ in the current configuration is the changed position of particle $\boldsymbol{X}$. Then the *caloric equation of state* becomes

$$u = u\left(s, \boldsymbol{F}\right). \tag{2.43}$$

Assuming that the caloric equation of state in Eq. (2.43) is invertible, we obtain

$$s = s\left(u, \boldsymbol{F}\right). \tag{2.44}$$

Thermodynamic temperature θ is defined by

$$\theta \equiv \frac{\partial u}{\partial s}\Big|_{\boldsymbol{F}}, \quad \text{or,} \quad \theta^{-1} \equiv \frac{\partial s}{\partial u}\Big|_{\boldsymbol{F}}. \tag{2.45}$$

For a given particle, from the caloric equation of state in Eq. (2.43), and the definition in Eq. (2.45), it follows that

$$\theta = \theta\left(s(u, \boldsymbol{F}), \boldsymbol{F}\right) = \hat{\theta}\left(u, \boldsymbol{F}\right). \tag{2.46}$$

Taking a material time derivative of Eq. (2.44) and using the definition in Eq. (2.45), we obtain

$$\begin{aligned}\dot{s} &= \frac{\partial s}{\partial u}\Big|_{\boldsymbol{F}}\dot{u} + \frac{\partial s}{\partial \boldsymbol{F}}\Big|_{u} : \dot{\boldsymbol{F}} \\ &= \frac{1}{\theta}\dot{u} + \frac{\partial s}{\partial \boldsymbol{F}}\Big|_{u} : \dot{\boldsymbol{F}}.\end{aligned} \tag{2.47}$$

When the deformation in the material is allowed without keeping any heat source in the body, then the energy equation in Eq. (2.1) takes the form

$$\rho\dot{u} = \boldsymbol{\sigma} : \boldsymbol{d} - \mathrm{div}\boldsymbol{q}, \tag{2.48}$$

where ρ is the density, $\boldsymbol{\sigma}$ is the stress tensor and $\boldsymbol{d}$ represents the rate of deformation tensor. Actually, $\boldsymbol{d}$ is the symmetric part of the velocity gradient $\boldsymbol{l}$, i.e., $\boldsymbol{d} = \frac{1}{2}\left(\boldsymbol{l} + \boldsymbol{l}^T\right)$ and $\boldsymbol{l} = \boldsymbol{\nabla v}$, where $\boldsymbol{v} = \boldsymbol{v}(\boldsymbol{x}, t)$ is the velocity at space point $\boldsymbol{x}$ and time t. Now, substituting Eq. (2.48) into Eq. (2.47), we have

$$\rho\theta\dot{s} = \rho\left[\frac{1}{\rho}\boldsymbol{\sigma} : \boldsymbol{d} + \theta\frac{\partial s}{\partial \boldsymbol{F}} : \dot{\boldsymbol{F}}\right] - \mathrm{div}\boldsymbol{q}. \tag{2.49}$$

Since $\boldsymbol{\sigma}$ is the symmetric tensor, therefore, $\boldsymbol{\sigma} : \boldsymbol{d} = \boldsymbol{\sigma} : \boldsymbol{l}$. Also, since $\dot{\boldsymbol{F}} = \boldsymbol{l}\boldsymbol{F}$, we have $\boldsymbol{l} = \dot{\boldsymbol{F}}\boldsymbol{F}^{-1}$. Substituting these in Eq. (2.49), we get

$$\rho\dot{s} = \frac{1}{\theta}\left[\boldsymbol{\sigma}\boldsymbol{F}^{-T} + \rho\theta\frac{\partial s}{\partial \boldsymbol{F}}\right] : \dot{\boldsymbol{F}} - \frac{1}{\theta}\mathrm{div}\boldsymbol{q}. \tag{2.50}$$

Also, we know that

$$\mathrm{div}\frac{\boldsymbol{q}}{\theta} = \frac{1}{\theta}\mathrm{div}\boldsymbol{q} - \frac{1}{\theta^2}\boldsymbol{q} \cdot \boldsymbol{\nabla}\theta. \tag{2.51}$$

Adding Eq. (2.50) and Eq. (2.51), we obtain

$$\rho\dot{s} + \mathrm{div}\frac{\boldsymbol{q}}{\theta} = \frac{1}{\theta}\left[\boldsymbol{\sigma}\boldsymbol{F}^{-\mathrm{T}} + \rho\theta\frac{\partial \mathrm{s}}{\partial \boldsymbol{F}}\right] : \dot{\boldsymbol{F}} - \frac{1}{\theta^2}\boldsymbol{q} \cdot \boldsymbol{\nabla}\theta. \tag{2.52}$$

Also, Reynolds transport equation for the entropy flux vector can be written as,

$$\int_V \rho\dot{s}dV = \int_V \Sigma dV - \int_S \boldsymbol{J} \cdot \boldsymbol{n}dS \tag{2.53}$$

where $\boldsymbol{J}$ is the energy flux vector, Σ is the entropy production rate per unit volume within volume V of the thermodynamic system, and $\boldsymbol{n}$ is the unit normal of the surface

area dS. Using the divergence theorem for the surface integral in Eq. (2.53), and making sure that Eq. (2.53) remains valid for any arbitrary volume V, the Reynolds transport equation for the entropy flux vector takes the following form:

$$\rho\dot{s} + \mathrm{div}\boldsymbol{J} = \Sigma \tag{2.54}$$

Comparing the two equations, Eqs. (2.52) and (2.54), we can say that,

$$\boldsymbol{J} = \frac{\boldsymbol{q}}{\theta}, \qquad \Sigma = -\frac{1}{\theta^2}\boldsymbol{q}\cdot\boldsymbol{\nabla}\theta + \frac{1}{\theta}\left[\boldsymbol{\sigma}\boldsymbol{F}^{-T} + \rho\theta\frac{\partial s}{\partial \boldsymbol{F}}\right] : \dot{\boldsymbol{F}} \tag{2.55}$$

The Clausius-Duhem inequality can be written as $\Sigma \geq 0$. One possible solution satisfying this inequality is

$$\frac{1}{\theta^2}\boldsymbol{\nabla}\theta = -A\boldsymbol{q}, \quad \text{and} \quad \left[\boldsymbol{\sigma}\boldsymbol{F}^{-T} + \rho\theta\frac{\partial s}{\partial \boldsymbol{F}}\right] : \dot{\boldsymbol{F}} \geq 0. \tag{2.56}$$

where A is a constant and $A \geq 0$. This leads to the familiar Fourier's law of heat conduction:

$$\boldsymbol{q} = -k\boldsymbol{\nabla}\theta, \qquad \text{where,} \quad k = \frac{1}{A\theta^2} \geq 0. \tag{2.57}$$

Thus Fourier's law is derived with the help of thermodynamics where it has been assumed that processes are *quasi-stationary*. Here, we have also assumed that the heat flux vector and the temperature gradient develop simultaneously, i.e., one doesn't precede the other. Similarly, we have assumed that neither the stress tensor nor the rate of deformation tensor precede each other. However, in the fast transient processes, it may happen that the heat flux vector $\boldsymbol{q}$ follows the temperature gradient $\boldsymbol{\nabla}\theta$ and the stress tensor $\boldsymbol{\sigma}$ follows the rate of deformation tensor $\boldsymbol{d}$. In this case, additional fundamental state variables have to be considered in defining the specific entropy s. Thus, the functional form (2.44) of the specific entropy s changes as

$$s = s\left(u, \boldsymbol{F}, \boldsymbol{q}, \boldsymbol{\sigma}\right). \tag{2.58}$$

Again, taking a material time derivative of Eq. (2.58), we get

$$\dot{s} = \frac{\partial s}{\partial u}\Big|_{\boldsymbol{F},\boldsymbol{q},\boldsymbol{\sigma}}\dot{u} + \frac{\partial s}{\partial \boldsymbol{F}}\Big|_{u,\boldsymbol{q},\boldsymbol{\sigma}} : \dot{\boldsymbol{F}} + \frac{\partial s}{\partial \boldsymbol{q}}\Big|_{u,\boldsymbol{F},\boldsymbol{\sigma}}\cdot\dot{\boldsymbol{q}} + \frac{\partial s}{\partial \boldsymbol{\sigma}}\Big|_{u,\boldsymbol{F},\boldsymbol{q}}\dot{\boldsymbol{\sigma}}^{T}. \tag{2.59}$$

Temperature θ is defined in this case as $\frac{1}{\theta} = \frac{\partial s}{\partial u}\Big|_{\boldsymbol{F},\boldsymbol{q},\boldsymbol{\sigma}}$ and, therefore, eq. (2.59) becomes

$$\dot{s} = \frac{1}{\theta}\dot{u} + \frac{\partial s}{\partial \boldsymbol{F}}\Big|_{u,\boldsymbol{q},\boldsymbol{\sigma}} : \dot{\boldsymbol{F}} + \frac{\partial s}{\partial \boldsymbol{q}}\Big|_{u,\boldsymbol{F},\boldsymbol{\sigma}} \cdot \dot{\boldsymbol{q}} + \frac{\partial s}{\partial \boldsymbol{\sigma}}\Big|_{u,\boldsymbol{F},\boldsymbol{q}} \dot{\boldsymbol{\sigma}^T}. \tag{2.60}$$

Performing a Taylor series expansion around an equilibrium state for both $\boldsymbol{q}$ and $\boldsymbol{\sigma}$ gives,

$$s = s_0 + \frac{\partial s}{\partial \boldsymbol{q}}\bigg|_0 \cdot \boldsymbol{q} + \frac{\partial s}{\partial \boldsymbol{\sigma}}\bigg|_0 \boldsymbol{\sigma}^T + \frac{1}{2}\left(\frac{\partial^2 s}{\partial \boldsymbol{q}^2}\bigg|_0 \boldsymbol{q}\cdot\boldsymbol{q} + 2\frac{\partial^2 s}{\partial \boldsymbol{q}\partial\boldsymbol{\sigma}^T}\bigg|_0 \boldsymbol{q}\boldsymbol{\sigma}^T + \frac{\partial^2 s}{\partial \boldsymbol{\sigma}\partial\boldsymbol{\sigma}^T}\bigg|_0 \boldsymbol{\sigma}\boldsymbol{\sigma}^T\right) + \cdots \tag{2.61}$$

If one neglects the coupling between the thermal and mechanical terms and takes into account that the specific entropy should reach maximum at equilibrium, i.e., $\frac{\partial s}{\partial \boldsymbol{q}}\Big|_0 = \frac{\partial s}{\partial \boldsymbol{\sigma}}\Big|_0 = 0$, then

$$\frac{\partial s}{\partial \boldsymbol{q}} = \frac{\partial^2 s}{\partial \boldsymbol{q}^2}\bigg|_0 \boldsymbol{q} + \cdots \tag{2.62}$$

$$\frac{\partial s}{\partial \boldsymbol{\sigma}} = \frac{\partial^2 s}{\partial \boldsymbol{\sigma}\partial\boldsymbol{\sigma}^T}\bigg|_0 \boldsymbol{\sigma} + \cdots \tag{2.63}$$

Usually, $\frac{\partial s}{\partial \boldsymbol{q}} \geq 0$, and $\frac{\partial s}{\partial \boldsymbol{\sigma}} \geq 0$, since whatever be the process, the entropy never decreases. Moreover, $\frac{\partial^2 s}{\partial \boldsymbol{q}^2} < 0$, and $\frac{\partial^2 s}{\partial \boldsymbol{\sigma}\partial\boldsymbol{\sigma}^T} < 0$, since the specific entropy achieves maxima at equilibrium. Hence, equation (2.62) suggests that

$$\frac{\partial s}{\partial \boldsymbol{q}} \approx -C_1 \boldsymbol{q}, \qquad C_1 = -\frac{\partial^2 s}{\partial \boldsymbol{q}^2}\bigg|_0 \geq 0, \tag{2.64}$$

$$\frac{\partial s}{\partial \boldsymbol{\sigma}} \approx -C_2\, \boldsymbol{\sigma}, \qquad C_2 = \frac{\partial^2 s}{\partial \boldsymbol{\sigma}\partial\boldsymbol{\sigma}^T}\bigg|_0 \geq 0. \tag{2.65}$$

Consequently, Eq. (2.60) becomes,

$$\dot{s} = \frac{1}{\theta}\dot{u} + \frac{\partial s}{\partial \boldsymbol{F}}\Big|_{u,\boldsymbol{q},\boldsymbol{\sigma}} : \dot{\boldsymbol{F}} - C_1 \boldsymbol{q}\cdot\dot{\boldsymbol{q}} - C_2\, \boldsymbol{\sigma}\dot{\boldsymbol{\sigma}^T}. \tag{2.66}$$

Using Eq. (2.66), we get the corresponding equation for Eq. (2.52):

$$\begin{aligned}\rho\dot{s} + \operatorname{div}\frac{\boldsymbol{q}}{\theta} = -\boldsymbol{q}\cdot\left[\frac{1}{\theta^2}\boldsymbol{\nabla}\theta + \rho C_1 \dot{\boldsymbol{q}}\right] \\ + \frac{1}{\theta}\left[\boldsymbol{\sigma}\boldsymbol{F}^{-T} + \rho\theta\frac{\partial s}{\partial \boldsymbol{F}}\right] : \dot{\boldsymbol{F}} - \rho C_2 \boldsymbol{\sigma}\dot{\boldsymbol{\sigma}^T}.\end{aligned} \tag{2.67}$$

We now can compare the above equation with the Reynolds transport equation in Eq. (2.55) to obtain the entropy production rate Σ,

$$\Sigma = -\boldsymbol{q} \cdot \left[\frac{1}{\theta^2} \boldsymbol{\nabla}\theta + \rho C_1 \dot{\boldsymbol{q}} \right] + \frac{1}{\theta} \left[\boldsymbol{\sigma} \boldsymbol{F}^{-T} + \rho\theta \frac{\partial s}{\partial \boldsymbol{F}} \right] : \dot{\boldsymbol{F}} - \rho C_2 \boldsymbol{\sigma} \dot{\boldsymbol{\sigma}}^T. \tag{2.68}$$

To satisfy the Clausius-Duhem inequality, i.e., $\Sigma \geq 0$, one possible solution as like eq. (2.56) is

$$\begin{aligned} &\frac{1}{\theta^2} \boldsymbol{\nabla}\theta + \rho C_1 \dot{\boldsymbol{q}} = -A\boldsymbol{q}, \\ \text{and} \quad &\left[\boldsymbol{\sigma} \boldsymbol{F}^{-T} + \rho\theta \frac{\partial s}{\partial \boldsymbol{F}} \right] : \dot{\boldsymbol{F}} - \rho C_2 \boldsymbol{\sigma} \dot{\boldsymbol{\sigma}}^T \geq 0, \end{aligned} \tag{2.69}$$

where A is a constant and $A \geq 0$. This leads to the constitutive equation for the heat flux vector similar to the CV wave model in Eq. (2.5) or Cattaneo's equation in Eq. (2.40):

$$\tau \frac{\partial \boldsymbol{q}}{\partial t}(\boldsymbol{x}, t) + \boldsymbol{q}(\boldsymbol{x}, t) = -k \boldsymbol{\nabla}\theta(\boldsymbol{x}, t), \tag{2.70}$$

where, $k = \frac{1}{A\theta^2} \geq 0$ and $\tau = \frac{\rho C_1}{A} \geq 0$. For the above relationship, we have assumed that higher than second order disturbances are negligible and the thermomechanical coupling can be neglected. We have also assumed that the temperature gradient precedes the heat flux vector. Now, this time let us assume opposite that the heat flux vector $\boldsymbol{q}$ precedes the temperature gradient $\boldsymbol{\nabla}\theta$ and the stress tensor $\boldsymbol{\sigma}$ precedes the rate of deformation tensor $\boldsymbol{d}$. This changes the functional form (2.44) of the specific entropy s such that

$$s = s\left(u, \boldsymbol{F}, \boldsymbol{\nabla}\theta, \boldsymbol{d}\right). \tag{2.71}$$

Proceeding in the same way as we did for Eq. (2.59), we obtain

$$\dot{s} = \left.\frac{\partial s}{\partial u}\right|_{\boldsymbol{F}, \boldsymbol{\nabla}\theta, \boldsymbol{d}} \dot{u} + \left.\frac{\partial s}{\partial \boldsymbol{F}}\right|_{u, \boldsymbol{\nabla}\theta, \boldsymbol{d}} : \dot{\boldsymbol{F}} + \left.\frac{\partial s}{\partial \boldsymbol{\nabla}\theta}\right|_{u, \boldsymbol{F}, \boldsymbol{d}} \cdot \dot{\boldsymbol{\nabla}}\theta + \left.\frac{\partial s}{\partial \boldsymbol{d}}\right|_{u, \boldsymbol{F}, \boldsymbol{\nabla}\theta} \dot{\boldsymbol{d}}^T. \tag{2.72}$$

Neglecting higher than second order terms from Taylor series expansion for the entropy s around an equilibrium state for both $\boldsymbol{\nabla}\theta$ and $\boldsymbol{d}$, we get

$$\begin{aligned} s = s_0 + &\left.\frac{\partial s}{\partial \boldsymbol{\nabla}\theta}\right|_0 \cdot \boldsymbol{\nabla}\theta + \left.\frac{\partial s}{\partial \boldsymbol{d}}\right|_0 \boldsymbol{d}^T + \\ &\frac{1}{2} \left(\left.\frac{\partial^2 s}{\partial (\boldsymbol{\nabla}\theta)^2}\right|_0 \boldsymbol{\nabla}\theta \cdot \boldsymbol{\nabla}\theta + 2 \left.\frac{\partial^2 s}{\partial \boldsymbol{\nabla}\theta \partial \boldsymbol{d}^T}\right|_0 \boldsymbol{\nabla}\theta \boldsymbol{d}^T + \left.\frac{\partial^2 s}{\partial \boldsymbol{d} \partial \boldsymbol{d}^T}\right|_0 \boldsymbol{d}\boldsymbol{d}^T \right) + \cdots \end{aligned} \tag{2.73}$$

Doing the operations as we have done above, Eq. (2.72) takes this form:

$$\dot{s} = \frac{1}{\theta}\dot{u} + \frac{\partial s}{\partial \boldsymbol{F}}\Big|_{u,\boldsymbol{\nabla}\theta,\boldsymbol{d}} : \dot{\boldsymbol{F}} - C_3 \boldsymbol{\nabla}\theta \cdot \dot{\boldsymbol{\nabla}}\theta - C_4 \boldsymbol{d}\dot{\boldsymbol{d}}^T, \tag{2.74}$$

where the constants

$$C_3 = -\frac{\partial^2 s}{\partial(\boldsymbol{\nabla}\theta)^2}\bigg|_0 \geq 0, \quad \text{and} \quad C_4 = \frac{\partial^2 s}{\partial \boldsymbol{d}\partial \boldsymbol{d}^T}\bigg|_0 \geq 0.$$

Using Eq. (2.74), and performing similar operations as we did for Eq. (2.67), we obtain,

$$\begin{aligned}\rho\dot{s} + \operatorname{div}\frac{\boldsymbol{q}}{\theta} = -\boldsymbol{\nabla}\theta \cdot \left[\frac{1}{\theta^2}\boldsymbol{q} + \rho C_3 \dot{\boldsymbol{\nabla}}\theta\right] \\ + \frac{1}{\theta}\left[\boldsymbol{\sigma}\boldsymbol{F}^{-T} + \rho\theta\frac{\partial s}{\partial \boldsymbol{F}}\right] : \dot{\boldsymbol{F}} - \rho C_4 \boldsymbol{d}\dot{\boldsymbol{d}}^T.\end{aligned} \tag{2.75}$$

With the help of Eq. (2.75), Eq. (2.68) takes this form:

$$\Sigma = -\boldsymbol{\nabla}\theta \cdot \left[\frac{1}{\theta^2}\boldsymbol{q} + \rho C_3 \dot{\boldsymbol{\nabla}}\theta\right] + \frac{1}{\theta}\left[\boldsymbol{\sigma}\boldsymbol{F}^{-T} + \rho\theta\frac{\partial s}{\partial \boldsymbol{F}}\right] : \dot{\boldsymbol{F}} - \rho C_4 \boldsymbol{d}\dot{\boldsymbol{d}}^T.$$

The equation analogous to Eq. (2.69) is,

$$\begin{aligned}\frac{1}{\theta^2}\boldsymbol{q} + \rho C_3 \dot{\boldsymbol{\nabla}}\theta = (A_2 - A_1)\,\boldsymbol{\nabla}\theta, \\ \text{and} \quad \left[\boldsymbol{\sigma}\boldsymbol{F}^{-T} + \rho\theta\frac{\partial s}{\partial \boldsymbol{F}}\right] : \dot{\boldsymbol{F}} - \rho C_4 \boldsymbol{d}\dot{\boldsymbol{d}}^T \geq 0,\end{aligned} \tag{2.76}$$

where the constants $A_1 > A_2 \geq 0$. This expression (2.76) assumes the heat flux-precedence whereas the expression (2.69) is built upon the temperature gradient-precedence. Combining the two expressions leads to the full spectrum of the dual-phase-lag behavior. Plugging out the term $\boldsymbol{\nabla}\theta$ from Eq. (2.76), $\boldsymbol{\nabla}\theta = \frac{A_1}{A_2}\boldsymbol{\nabla}\theta + \frac{1}{A_2\theta^2}\boldsymbol{q} + \frac{\rho C_3}{A_2}\dot{\boldsymbol{\nabla}}\theta$, and substituting this into Eq. (2.69), we obtain,

$$\tau_q \frac{\partial \boldsymbol{q}}{\partial t}(\boldsymbol{x},t) + \boldsymbol{q}(\boldsymbol{x},t) = -k\boldsymbol{\nabla}\theta(\boldsymbol{x},t) - k\tau_\theta \frac{\partial \boldsymbol{\nabla}\theta}{\partial t}(\boldsymbol{x},t), \tag{2.77}$$

where the constants

$$\tau_q = \frac{\rho C_1}{A + 1/\left(A_2\theta^4\right)} > 0, \quad \tau_\theta = \frac{\rho C_3}{A_1} > 0, \quad \text{and,} \quad k = \frac{A_1/\left(A_2\theta^2\right)}{A + 1/\left(A_2\theta^4\right)} > 0.$$

Clearly, Eq. (2.77) is similar to the *dual-phase-lag model* in Eq. (2.8) or *heat-flux equation of Jeffreys-Type* (2.38).

2.4 Summary

Should we summarize this chapter, the modification in Fourier's equation in Eq. (1.1) has been suggested. The non-physical assumption of infinite speed involved in the Fourier's equation motivated Joseph and Perziosi [2] to introduce the concept of *effective thermal conductivity* and *effective heat capacity*. Inspired by separating the cause and effect between the heat flux vector and the temperature gradient, Tzou [25, 26, 27, 28, 60, 61] introduces the *dual phase-lag* concept. Further, the thermodynamic analysis supports the proposed modifications. Based upon overall discussion, we can list down different constitutive equations for heat flux:

Fourier's equation:

$\boldsymbol{q} = -k\boldsymbol{\nabla}\theta$

Cattaneo's equation or the CV wave model:

$\tau\frac{\partial \boldsymbol{q}}{\partial t} + \boldsymbol{q} = -k\boldsymbol{\nabla}\theta$

Heat-flux equation of the Jeffreys-type or the dual-phase-lag model:

$\tau\frac{\partial \boldsymbol{q}}{\partial t} + \boldsymbol{q} = -k\boldsymbol{\nabla}\theta - \tau k_1\frac{\partial \boldsymbol{\nabla}\theta}{\partial t}$

The corresponding partial differential equations for the temperature field when the material is perfectly *rigid*:

Diffusion Equation:

$\frac{\partial\theta}{\partial t} = \frac{k}{\gamma}\nabla^2\theta$

Cattaneo's telegraph equation:

$\frac{\partial^2\theta}{\partial t^2} + \frac{1}{\tau}\frac{\partial\theta}{\partial t} = c^2\nabla^2\theta$

Jeffreys-type:

$\frac{\partial^2\theta}{\partial t^2} + \frac{1}{\tau}\frac{\partial\theta}{\partial t} = c^2\nabla^2\theta + \frac{k_1}{\gamma}\nabla^2\frac{\partial\theta}{\partial t}$

$k = k_1 + k_2$	thermal conductivity
k_1	effective conductivity
k_2	elastic conductivity
τ	relaxation time
c	wave speed
$\tau_q = \tau$	phase-lag of heat flux
$\tau_\theta = \frac{k_1}{k}\tau$	phase-lag of temperature gradient
$\alpha = k/\gamma = c^2\tau_q$	thermal diffusivity
γ	specific heat capacity

Chapter 3

Obtaining thermal parameters using molecular dynamics

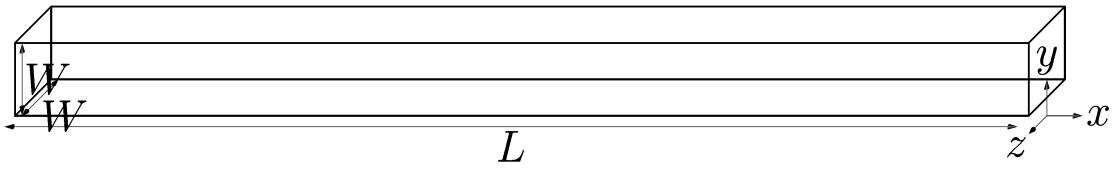

Figure 3.1: Schematic of a slender beam.

Our objective is to obtain the thermal parameters appearing in the continuum models described in Chapter 2 by performing MD simulations. As the test system, we choose a slender nanobeam of length L and square cross-section of side W with $L \gg W$ (see Fig. 3.1). Slender beam allows us to approximate the three-dimensional heat transfer models as one-dimensional. The thermal conductivity is obtained using the standard Green-Kubo and NEMD direct methods outlined in Section 3.2, and all three Jeffreys-type model parameters are obtained using the new regression-based TPI approach proposed in Section 3.2.3. We begin by describing a binning procedure for MD simulations, which is required for both the NEMD direct method and the TPI approach. But, first we will discuss the details of equilibrium MD, NEMD terms and tools.

3.1 Introduction to equilibrium and nonequlibrium Molecular Dynamics

Molecular Dynamics (MD) simulation is a technique for computing the equilibrium and transport properties of a classical many body system. The history of MD goes back to the mid 50's when computer simulations were performed on simple systems. Metropolis and co-workers [72] developed a general method for computing the statistical properties of a system composed of interacting molecules, which was later known as Metropolis Monte-Carlo algorithm. Fermi, Pasta and Ulam [73, 74] studied a one-dimensional vibrating string that included nonlinear terms of quadratic, cubic and broken linear types and found that instead of showing the ergodic behavior and giving rise to equipartition of energy among all degrees of freedom in average sense, the system exhibited complex quasi-periodic behavior.

Alder and Wainwright [75, 76] first developed the molecular dynamics simulation techniques through which they solved the simultaneous classical equations of motion of several hundred particles, including the liquid-solid phase transition for hard sphere. Rahman [77] studied a system of 864 particles interacting with Lennard-Jones potential under the classical equations of motion to simulate liquid argon. He found the pair-correlation function and the self-diffusion constant close to the experimental values. Following Rahman's work, Verlet [78] showed the possibility of integrating the equations of motion of 864 particles in a relatively easier way, later known as Verlet algorithm, and found the results to be in agreement with the thermodynamics of real argon.

MD simulations assume that the molecules or atoms are a system of interacting points or particles, whose motion is described by their instantaneous positions and velocities vectors. Also the interaction has a strong dependence upon the spatial orientation and distances between separate points. It is also assumed that mass of the system remains the same [79].

3.1.1 Simulation Algorithm

Consider a system of N interacting particles whose cartesian coordiantes are given by $\boldsymbol{r}^N = \{\boldsymbol{r}_i\}$, where $i = 1, \ldots, N$ and $\boldsymbol{r}_i := \boldsymbol{r}_i(t)$. The classical equations of motion can

be written in Newtonian form as

$$m_i \ddot{\boldsymbol{r}}_i = -\frac{\partial \mathcal{U}}{\partial \boldsymbol{r}_i} = \boldsymbol{f}_i, \tag{3.1}$$

where m_i and $\boldsymbol{f}_i$ refer to the mass of the ith particle and the force action upon the ith particle by all other particles. $\mathcal{U} := \mathcal{U}(\boldsymbol{r}^N)$ defines the potential energy of the system of particles, which is further written as

$$\mathcal{U}(\boldsymbol{r}^N) = \sum_{i=1}^{N-1} \sum_{j>i}^{N} \phi\left(\boldsymbol{r}_{ij}\right), \tag{3.2}$$

where $\boldsymbol{r}_{ij} = \boldsymbol{r}_i - \boldsymbol{r}_j$ and $\phi\left(\boldsymbol{r}_{ij}\right)$ is the interatomic potential between the particles i and j, assuming that $\mathcal{U}$ is pairwise additive. For covalent solids, silicon or carbon, an additional three body term is included to take into account the bong angle dependence of the potential.[1] In general, the potential energy function is presented as

$$\mathcal{U}(\boldsymbol{r}^N) = \sum_{i=1}^{N} \phi_1\left(\boldsymbol{r}_i\right) + \sum_{i=1}^{N-1} \sum_{j>i}^{N} \phi_2\left(\boldsymbol{r}_{ij}\right) + \sum_{i=1}^{N-2} \sum_{j>i}^{N-1} \sum_{k>j}^{N} \phi_3\left(\boldsymbol{r}_i, \boldsymbol{r}_j, \boldsymbol{r}_k\right) + \cdots, \tag{3.3}$$

where the function ϕ_m is m-body potential depending upon the m body terms involving $\{\boldsymbol{r}_i\}$, where $i = 1, \ldots, M$. The first term in this Eq. (3.3) represents the potential energy because of a conservative external force field or the effects of the boundary walls. This is usually dropped for fully periodic simulations of bulk systems. One of the most common interatomic two-body (pair) potential is *Lennard-Jones (LJ) potential*, proposed by Jones in 1924 [85, 86]:

$$\mathcal{U}\left(\boldsymbol{r}_i, \boldsymbol{r}_j\right) = \tilde{\mathcal{U}}\left(r\right) = 4\,\epsilon \left[\left(\frac{\sigma}{r}\right)^{12} - \left(\frac{\sigma}{r}\right)^{6}\right], \tag{3.4}$$

where $r = |\boldsymbol{r}_{ij}| = |\boldsymbol{r}_i - \boldsymbol{r}_j|$. Also, $\boldsymbol{r}_{ij}$ is the interatomic separation vector, ϵ is the dislocation energy and σ is the collision diameter, the distance at which $\tilde{\mathcal{U}}\left(r\right) = 0$. The first term is positive in the potential function (3.4) and represents repulsion, where as the second term is negative and represents attraction between two particles. The equilibrium distance between the two particles is attained when $\tilde{\mathcal{U}}$ is minimum, or $r_{eqb} = 2^{1/6}\sigma$. The dislocation energy ϵ is thus the amount of work done to remove one of the bonded

[1] For a detail discussion on interatomic potentials, please see [79, 80, 81, 82, 83, 84].

particles from r_{eqb} to ∞. The corresponding force between the two particles can be written in terms of distance r as

$$f(r) = -\frac{\partial \tilde{\mathcal{U}}(r)}{\partial r} = 24\,\frac{\epsilon}{\sigma}\left[\left(\frac{\sigma}{r}\right)^{13} - \left(\frac{\sigma}{r}\right)^{7}\right]. \tag{3.5}$$

The Newtonian form in Eq. (3.1) comes from the Lagrangian description of the system [79], where Lagrangian $\mathcal{L}$ is

$$\mathcal{L}\left(\dot{\boldsymbol{r}}^N, \boldsymbol{r}^N\right) = \sum_{i=1}^{N} \frac{1}{2}\, m_i\, \dot{\boldsymbol{r}}_i^2 - \mathcal{U}\left(\boldsymbol{r}^N\right) \tag{3.6}$$

Usually, $\mathcal{L} := \mathcal{L}\left(\dot{\boldsymbol{r}}^N(t), \boldsymbol{r}^N(t), t\right)$ and using calculus of variation it can be showed that the Lagrangian $\mathcal{L}$ follows Euler-Lagrange equation:

$$\frac{d}{dt}\frac{\partial \mathcal{L}\left(\dot{\boldsymbol{r}}^N(t), \boldsymbol{r}^N(t), t\right)}{\partial \dot{\boldsymbol{r}}_i} - \frac{\partial \mathcal{L}\left(\dot{\boldsymbol{r}}^N(t), \boldsymbol{r}^N(t), t\right)}{\partial \boldsymbol{r}_i} = 0, \quad \text{for} \quad i = 1, \ldots, N. \tag{3.7}$$

In our case, as Eq. (3.6) suggests, $\mathcal{L}$ is explicitly independent of variable t, and only remains parametrically dependent upon time t, i.e., $\mathcal{L} := \mathcal{L}\left(\dot{\boldsymbol{r}}^N(t), \boldsymbol{r}^N(t)\right)$. For this Lagrangian, we get the equation of motion in the Newtonian form, which is Eq. (3.1).

Now, we also introduce *generalized momenta* of all the particles $\boldsymbol{p}^N = \{\boldsymbol{p}_i\}$, where $i = 1, \ldots, N$ and $\boldsymbol{p}_i := \boldsymbol{p}_i(t)$, and write the total kinetic energy of the system as $\mathcal{K}_T := \mathcal{K}_T\left(\boldsymbol{p}^N\right)$, where

$$\mathcal{K}_T\left(\boldsymbol{p}^N\right) = \sum_{i=1}^{N} \frac{{\boldsymbol{p}_i}^2}{2\, m_i}. \tag{3.8}$$

Now, for all the known positions and generalized momenta vectors, $\boldsymbol{r}^N, \boldsymbol{p}^N \in \mathbb{R}^{dN}$, where d be the dimensional space, the definition for the generalized momentum

$$\boldsymbol{p}_i = \frac{\partial \mathcal{L}\left(\dot{\boldsymbol{r}}^N, \boldsymbol{r}^N\right)}{\partial \dot{\boldsymbol{r}}_i}$$

has the unique solution for $\dot{\boldsymbol{r}}_i$ as a smooth function of $\boldsymbol{p}_i$, i.e., $\dot{\boldsymbol{r}}_i = \boldsymbol{p}_i/m_i = \boldsymbol{v}_i(\boldsymbol{p}_i)$. Using this definition, the Euler-Lagrange equation becomes:

$$\dot{\boldsymbol{p}}_i = \frac{\partial \mathcal{L}\left(\dot{\boldsymbol{r}}^N, \boldsymbol{r}^N\right)}{\partial \boldsymbol{r}_i} \quad \text{for} \quad i = 1, \ldots, N. \tag{3.9}$$

By definition, the Hamiltonian $\mathcal{H}$ of the system associated with the Lagrangian $\mathcal{L}$ is

$$\mathcal{H}\left(\boldsymbol{p}^N, \boldsymbol{r}^N, t\right) = \left(\sum_{i=1}^{N} \boldsymbol{p}_i \cdot \boldsymbol{v}_i\left(\boldsymbol{p}_i\right)\right) - \mathcal{L}\left(\boldsymbol{v}_1(\boldsymbol{p}_1), \ldots, \boldsymbol{v}_N(\boldsymbol{p}_N), \boldsymbol{r}^N, t\right), \tag{3.10}$$

which by using the Eq. (3.6) gives,

$$\mathcal{H}\left(\boldsymbol{p}^N, \boldsymbol{r}^N, t\right) = \sum_{i=1}^{N} \frac{{\boldsymbol{p}_i}^2}{2\, m_i} + \mathcal{U}(\boldsymbol{r}^N), \tag{3.11}$$

and does not remain explicitly dependent upon time t, i.e., $\mathcal{H} := \mathcal{H}\left(\boldsymbol{p}^N, \boldsymbol{r}^N\right)$. The Hamiltonian $\mathcal{H}$ is thus the total energy, the sum of the kinetic and potential energies, i.e., $\mathcal{H} = \mathcal{K}_T + \mathcal{U}$. Using Eqs. (3.9) and (3.10), we can obtain the classical equations of motion in the Hamiltonian description:

$$\dot{\boldsymbol{r}}_i = \frac{\partial \mathcal{H}}{\partial \boldsymbol{p}_i}, \quad \dot{\boldsymbol{p}}_i = -\frac{\partial \mathcal{H}}{\partial \boldsymbol{r}_i}, \tag{3.12}$$

where momenta $\boldsymbol{p}_i = m_i\, \dot{\boldsymbol{r}}_i$ and the rate of momenta $\dot{\boldsymbol{p}}_i = \boldsymbol{f}_i$. This Hamiltonian $\mathcal{H}$, or the total energy, is constant in the case of conserved system $\mathcal{H}\left(\boldsymbol{p}^N, \boldsymbol{r}^N\right)$, as it follows from differentiating $\mathcal{H}$ w.r.t. time t and using eq. (3.12) :

$$\frac{d\mathcal{H}}{dt} = \frac{\partial \mathcal{H}}{\partial \boldsymbol{p}_i}\dot{\boldsymbol{p}}_i + \frac{\partial \mathcal{H}}{\partial \boldsymbol{r}_i}\dot{\boldsymbol{r}}_i = \dot{\boldsymbol{r}}_i\dot{\boldsymbol{p}}_i - \dot{\boldsymbol{p}}_i\dot{\boldsymbol{r}}_i = 0. \tag{3.13}$$

The equation system in Eq. (3.12) is a coupled system of ordinary differential equations, that can be solved if the initial states of the system remain known. Thus, we have an Initial Value Problem and solving it gives us the instantaneous position and momentum vectors of all the particles of the system. In effect, we get the full phase space trajectory of the system and, therefore, the thermodynamic states can be computed using the method of statistical mechanics, which will be described later. Newtonian version of the equations of motion in (3.1), which is equivalent to the Hamiltonian description of motion in Eq. (3.12), can be integrated in many ways by using different algorithms. A computationally efficient algorithm is Verlet Algorithm [78, 87], which exists in many equivalent versions such as 'Leapfrog' form [88] and 'Velocity Verlet' algorithm [89]. To derive the original Verlet algorithm, we start with a Taylor expansion of the position

vector of ith particle around time t,

$$\boldsymbol{r}_i(t+\delta t) = \boldsymbol{r}_i(t) + \dot{\boldsymbol{r}}_i(t)\,\delta t + \frac{\boldsymbol{f}_i(t)}{2\,m_i}\delta t^2 + \dddot{r}\frac{\delta t^3}{3!} + \mathcal{O}\left(\delta t^4\right)$$
$$\boldsymbol{r}_i(t-\delta t) = \boldsymbol{r}_i(t) - \dot{\boldsymbol{r}}_i(t)\,\delta t + \frac{\boldsymbol{f}_i(t)}{2\,m_i}\delta t^2 - \dddot{r}\frac{\delta t^3}{3!} + \mathcal{O}\left(\delta t^4\right).$$

Adding these two, we obtain the position vector at the next time-step,

$$\boldsymbol{r}_i(t+\delta t) = \boldsymbol{r}_i(t) - \boldsymbol{r}_i(t-\delta t) + \frac{\boldsymbol{f}_i(t)}{m_i}\delta t^2 + \mathcal{O}\left(\delta t^4\right). \tag{3.14}$$

Subtracting one from the second in above expansion yields the velocity vector,

$$\dot{\boldsymbol{r}}_i(t) = \frac{\boldsymbol{r}_i(t+\delta t) - \boldsymbol{r}_i(t-\delta t)}{2\delta t} + \mathcal{O}\left(\delta t^2\right). \tag{3.15}$$

This Verlet algorithm is time-reversible, as exchange of $\boldsymbol{r}_i(t+\delta t)$ and $\boldsymbol{r}_i(t-\delta t)$ changes the sign of the velocity and evolution of the algorithm takes place backward in time tracing the same trajectory. Also, it can be seen from Eq. (3.15) that the velocity updates one step behind the position vector. However, it is possible to cast the Verlet algorithm in such a way that both position and velocity vectors are updated at the same time-step. This is the 'Velocity Verlet' algorithm [89]. Here we use the same expansion as above,

$$\boldsymbol{r}_i(t+\delta t) = \boldsymbol{r}_i(t) + \dot{\boldsymbol{r}}_i(t)\,\delta t + \frac{\boldsymbol{f}_i(t)}{2\,m_i}\delta t^2 + \dddot{r}\frac{\delta t^3}{3!} + \mathcal{O}\left(\delta t^4\right). \tag{3.16}$$

And the corresponding time-reversed equation is

$$\boldsymbol{r}_i(t) = \boldsymbol{r}_i(t+\delta t) - \dot{\boldsymbol{r}}_i(t+\delta t)\,\delta t + \frac{\boldsymbol{f}_i(t+\delta t)}{2\,m_i}\delta t^2 - \dddot{r}\frac{\delta t^3}{3!} + \mathcal{O}\left(\delta t^4\right). \tag{3.17}$$

Adding Eqs. (3.16) and (3.17), we obtain

$$\dot{\boldsymbol{r}}_i(t+\delta t) = \dot{\boldsymbol{r}}_i(t) + \frac{\boldsymbol{f}_i(t+\delta t) + \boldsymbol{f}_i(t)}{2\,m_i}\delta t + \mathcal{O}\left(\delta t^3\right). \tag{3.18}$$

The order of the velocity computation has also increased by one as compared to the original Verlet algorithm. The Velocity Verlet algorithm can also be written as

$$\boldsymbol{p}_i\left(t+\frac{1}{2}\delta t\right) = \boldsymbol{p}_i(t) + \frac{1}{2}\boldsymbol{f}_i(t)\,\delta t \tag{3.19a}$$
$$\boldsymbol{r}_i(t+\delta t) = \boldsymbol{r}_i(t) + \frac{1}{m_i}\boldsymbol{p}_i\left(t+\frac{1}{2}\delta t\right)\delta t \tag{3.19b}$$
$$\boldsymbol{p}_i(t+\delta t) = \boldsymbol{p}_i\left(t+\frac{1}{2}\delta t\right) + \frac{1}{2}\boldsymbol{f}_i(t+\delta t)\,\delta t \tag{3.19c}$$

A fresh force calculation is carried out after the step in Eq. (3.19b). It can be showed [88] that this algorithm is equivalent to the original Verlet algorithm in Eqs. (3.14) and (3.15) in the sense that both algorithms yield the identical trajectories. Verlet algorithms by the nature of being time-reversible are area preserving and, therefore, exhibits little long-term energy drift. But these algorithms don't generate very accurate trajectories, where as higher-order schemes can allow to choose a longer time-step δt without loss of short-term accuracy. Though, higher-order schemes require more storage than Verlet algorithms and, usually, are neither time-reversible nor area-preserving. Gear predictor-corrector [90] and Runge-Kutta [91] are some of the higher order algorithms.

3.1.2 Periodic Boundary Conditions

Molecular Dynamics as molecular modeling only provides information about particles positions and momenta at the microscopic level. But measurement of most of the structural and thermodynamic properties, such as pressure, heat capacity, energy, temperature etc, require the macroscopic average of the microscopic positions and momenta. This connection from microscopic to macroscopic properties is made through Statistical Mechanics. Ergodic hypothesis is the justification behind this approach, which makes the statistical ensemble averages equal to the time averages of the system. Statistical mechanics provides a mathematical understanding of that physical system, which is an assembly of large number of identical small subsystems (particles) interacting among themselves to produce a thermodynamic behavior of the system [92]. A large number of small subsytems involve the consideration of the limit of an infinite system, known as the *thermodynamic limit*. In other words, if large number of particles or subsystems N tending to ∞ are enclosed in a bounded region Λ with volume V_Λ, then the thermodynamic limit is achieved by making V_Λ tending to ∞ and keeping N/V_Λ fixed. In other words,

$$\lim_{\substack{N\to\infty \\ V_\Lambda\to\infty \\ N/V_\Lambda \text{fixed}}} \text{system} = \text{thermodynamic limit} \approx \text{macroscopic observation.}$$

The thermodynamic limit is sufficient for a normal thermodynamic behavior, which deals with the phenomena close to the equilibrium states, even if the ergodicity assumption is not fulfilled [92].

But most MD simulations involve few hundred to few thousand particles, thus taking the system away from the thermodynamic limit. Also, the boundaries or surface effects become important for a small system. In order to mimic the the bulk and achieve the thermodynamic limit, periodic boundary conditions are employed. The enclosed volume containing N particles is assumed as primitive cell of an infinite periodic lattice of infinite cells [88, 90]. A particle and all its images behave in the same way and when a particle leaves the primitive cell, one of its images will enter the primitive cell through the opposite face, thus conserving the number of particles in the primitive cell. The topology of the one-dimensional periodic lattice is homeomorphic to a circle and that of two-dimensional is homeomorphic to a three-dimensional torus or doughnut. Periodic boundary conditions simulate the bulk but it captures only those fluctuations whose wavelengths are not more than the length of the periodic lattice. For large-range interatomic potential, where the interaction between particle and its images in the neighboring cells become important, then the artificial symmetry of the cell structure affects the system and an artificial anisotropy is introduced. There are other problems as well with periodic boundary conditions such as the unphysical rate at which the simulated liquid nucleates [90]. But in general, periodic boundary conditions have little effect on the equilibrium thermodynamic properties, and the effect decreases considerably when large number of particles are simulated.

3.1.3 Interatomic potential truncation

In the case of periodic boundary condition, every particle is ideally interacting with rest of the particles in the primitive and the other cells of the infinite periodic lattice. This involves infinite number of interactions. For the practical purpose in MD, which allows simulation for finite number of particles, the interactions can be approximated by truncation of potential for a system with *short-range* interactions. 'Simple truncation' is one method where all interactions are ignored beyond a spherically cut-off radius r_c. In another similar procedure, the potential is truncated and shifted such that beyond the cut-off radius there exists no interaction. Another quite common method is 'minimum image convention'. This is the method employed in our simulations. Here, any particle in the primitive cell interacts with the most nearest periodic image of other $N-1$ particles. Metropolis and co-workers [72] first used this method. There is still $N(N-1)/2$

interactions involved for pair-potential system, which could be further reduced for *short-range* interactions by using 'Simple truncation', i.e., by forcing the pair-potential $\tilde{\mathcal{U}}(r)$ to zero when $r \geq r_c$. In a cubic cell of length-size L, the number of neighbors explicitly considered is reduced by a factor of $4\pi r_c^3/3L^3$ [90]. Also, the cut-off radius r_c should not be more than $\frac{1}{2} L_{max}$, $L_{max} = \max\{L_i : i = 1, \ldots, d\}$, where d be the dimensional space of the system, to be consistent with 'minimum image convention'.

3.1.4 Neighbor Lists

The time spent in checking all pair separations, so that the separation distances remain within the cut-off radius r_c for which pair forces can be computed, is proportional to $N(N-1)/2$. Verlet [78] suggested an improved way for the pair force calculation in which a list of the neighbors for a particular particle is maintained. This list is updated at certain intervals. The potential cut-off sphere with radius r_c around all particles is enlarged by adding a 'skin' distance, so that a bigger sphere of radius $r_l = r_c +$ skin surrounds a particular atom or molecule. At first, a list is constructed of all the neighbors, defined by the pair separation less than r_l, i.e., by counting all the particles that lie in a spherical ball of radius r_l surrounding each particle. The list is reconstructed from time to time. The 'skin' distance is chosen such that between each reconstruction the particles which don't belong to the neighbors of a particular atom or molecule should not penetrate the list cut-off sphere with the radius r_l. The process of list construction can be automated on the basis that total displacement of each particle since the last reconstruction can be recorded at each time-step, and when the magnitudes of two largest displacements exceed the 'skin' distance, then the next reconstruction is triggered [90]. There is a trade-off between choosing r_l and the number of times the list demands to be updated. For large number of particles under simulation, cell index methods and linked list method can also be used [90].

3.1.5 Temperature

A usual definition of temperature in a classical many-particle system considers the use of Equipartition Theorem, which states that at thermal equilibrium each microscopic degree of freedom has average internal kinetic energy $\frac{1}{2} k_B \theta$, where k_B is Boltzmann

constant and θ is the temperature. When $\boldsymbol{p}_\alpha$ be the α component of the momentum vector of a particle, the following relation should hold:

$$\left\langle \frac{\boldsymbol{p}_\alpha^2}{2\,m_\alpha} \right\rangle = \frac{1}{2} k_B \theta, \tag{3.20}$$

where any instantaneous property $A(\Gamma)$, $\Gamma = \left(\boldsymbol{r}^N, \boldsymbol{p}^N\right)$ be a point in phase-space $\{\boldsymbol{r}^N, \boldsymbol{p}^N\}$, has experimentally measurable property A_m, which is reasonably assumed to be equal to the time average of $A(\Gamma)$ taken over a long time-interval:

$$A_m = \langle A \rangle = \lim_{t\to\infty} \frac{1}{t} \int_{t_0}^{t_0+t} A\left(\Gamma(\tau)\right)\, d\tau. \tag{3.21}$$

Therefore, in the case of internal kinetic energy $\mathcal{K}$ corresponding to the total number of internal degrees of freedom N_f, thermodynamic temperature is defined as

$$\langle \mathcal{K} \rangle = \frac{N_f}{2} k_B \theta, \quad \text{or,} \quad \theta = \frac{2}{N_f k_B} \langle \mathcal{K} \rangle . \tag{3.22}$$

Following Jellinek and Li [93], the internal kinetic energy can be separated from "rigid-body" part, i.e. rotational and translational part of the total kinetic energy of the system of N particles. The instantaneous internal kinetic energy is given by,

$$\mathcal{K} = \sum_{i=1}^{N} \frac{\tilde{\boldsymbol{p}}_i^2}{2\,m_i}, \tag{3.23}$$

where peculiar momentum $\tilde{\boldsymbol{p}}_i$ is given by,

$$\tilde{\boldsymbol{p}}_i = \boldsymbol{p}_i - \boldsymbol{p}^{cm} - \boldsymbol{\omega}^{cm} \times \left(\boldsymbol{r}_i - \boldsymbol{r}^{cm}\right). \tag{3.24}$$

Here $\boldsymbol{p}^{cm}$ is the momentum of the center of mass of the system and $\boldsymbol{\omega}^{cm}$ is the angular velocity of the system expressed in terms of inertia tensor $\boldsymbol{I}^{cm}$ of the system relative to the center of mass and angular momentum $\boldsymbol{L}^{cm}$ of the system about the center of mass, where

$$\boldsymbol{I}^{cm} = \boldsymbol{L}^{cm} \boldsymbol{\omega}^{cm}, \quad \boldsymbol{I}^{cm} = \sum_{i=1}^{N} m_i \left(\boldsymbol{r}_i - \boldsymbol{r}^{cm}\right) \otimes \left(\boldsymbol{r}_i - \boldsymbol{r}^{cm}\right), \tag{3.25}$$

$$\boldsymbol{L}^{cm} = \boldsymbol{r}^{cm} \times \boldsymbol{p}^{cm}, \quad \boldsymbol{r}^{cm} = \frac{\sum_i m_i \boldsymbol{r}_i}{\sum_i m_i}, \quad \boldsymbol{p}^{cm} = \frac{\sum_i m_i \boldsymbol{p}_i}{\sum_i m_i}. \tag{3.26}$$

In line with instantaneous internal kinetic energy, instantaneous *kinetic temperature* $\mathcal{T}$ can also be defined as

$$\mathcal{T} = \frac{2}{N_f k_B}\mathcal{K}, \tag{3.27}$$

and thermodynamic temperature is the ensemble average of $\mathcal{T}$, i.e., $\theta = \langle \mathcal{T} \rangle$.

Following the above formulation, the linear and angular momenta of the system vanish when particles have peculiar velocities. Also, since we have enforced the balance of linear and angular momenta of the system when the frame is chosen with respect to the center of mass, this means the number of constraints $= 2d$ in d-dimensional space. Therefore, total number of internal degrees of freedom becomes $N_f = d(N-2)$.

3.1.6 Thermostats

A modified MD algorithm in Eq. (3.1) or Eq. (3.12) so that a thermodynamic ensemble at constant temperature can be produced is called thermostat algorithm. Normally, the thermodynamic ensemble of MD in Eq. (3.1) is the microcanonical NVE ensemble [90, 94], because the Hamiltonian $\mathcal{H}$ or the total energy E remains conserved as suggested by Eq. (3.13), provided that the number of particles N and the volume occupied V also remains constant during the simulation and the errors in numerical integration remains negligible. But for various purposes the simulation demands that a part of the system (e.g. NEMD) or the full system remains at constant temperature. Here, we expect that canonical Maxwell-Boltzmann distribution should be obtained for the phase space distribution function, so that canonical isothermal-isochoric NVT ensemble, or the conjugate isothermal-isobaric NPT ensemble or isobaric-isoenthalpic NHT ensemble can be imitated. Since there are measures defined for these ensembles on phase space such as $\exp\left(-\beta\mathcal{H}(\boldsymbol{p}^N, \boldsymbol{r}^N)\right)$ for NVT or $\exp\left(-\beta(PV + \mathcal{H}(\boldsymbol{p}^N, \boldsymbol{r}^N))\right)$ for NPT or $\exp\left(-\beta(PV + \mathcal{H}(\boldsymbol{p}^N, \boldsymbol{r}^N) - H)\right)$ for NPH, where $\beta = \frac{1}{k_B\theta}$ and k_B be Boltzmann constant, therefore, the tools of Statistical Mechanics can be widely used with the help of these measures to mimic the real experiments [95].

But not all algorithms meant for controlling the temperature follow these ensembles [96]. For example, simple velocity rescaling algorithm, where after each update the

peculiar momenta of all the particles are rescaled by a parameter $\lambda_s = \sqrt{\frac{\theta_0}{\theta(t)}}$ as

$$\tilde{\boldsymbol{p}}_i(t+\delta t) = \lambda_s \tilde{\boldsymbol{p}}_i(t), \tag{3.28}$$

where θ_0 is the target temperature and $\theta(t)$ is the instantaneous temperature. Another improved velocity rescaling algorithm given by Berendsen et al [97] also fails to produce canonical ensemble, in which the rescaling parameter is $\lambda_s = \left[1 + \frac{\delta t}{\tau_\theta}\left(\frac{\theta(t)}{\theta_0} - 1\right)\right]^{1/2}$, where τ_θ is a constant called the "rise time" of the thermostat. But this thermostat is still widely used.

The first canonical ensemble producing thermostat was developed by Andersen [95] in which the system is coupled to a heat bath, represented by stochastic collision forces, which ensure that all accessible constant energy surface are sampled to their Boltzmann weight. The mixing of Newtonian equation of motion with stochastic collisions turns MD simulation into a Markov process, which is irreducible and aperiodic, thus generating a canonical distribution. The particle undergoing the collision with the heat bath is given a velocity from a Maxwell-Boltzmann distribution corresponding to the target temperature θ. Times between collisions with bath are chosen from a Poisson distribution with a specified mean collision time. The first deterministic thermostat, or Gaussian/isokinetic thermostat was developed by Hoover et al [98] and Evans [99], which generates isokinetic ensemble where total kinetic energy is strictly kept constant. But experimentally this is not realized. However, since thermostatting in this case is part of the equations of motion, hence its analysis becomes direct with the help of the response theory [100].

There are numerous thermostat algorithms but two of the widely used canonical NVT ensembles generating thermostats are discussed next.

3.1.7 Langevin Thermostat

As like in Andersen thermostat, here also the particle interacts with a heat bath in a stochastic manner. Inside the heat bath exists extremely fast modes as compared to the availability of slow modes in the main system. When both fast and slow modes are present, then solving the Newtonian equation of motion for both heat bath and the main system becomes highly expensive if short time-steps are chosen to capture all fast modes. But here fast modes are not of so much interest and the equations of motion can be simplified. The theoretical basis for removing rapidly changing degrees of freedom is

given by Mori [101, 102] and Zwanzig [103, 104, 105]. Consider two dynamical variables $A\left(\Gamma(t)\right), B\left(\Gamma(t)\right)$, where $\Gamma(t) = \left(\boldsymbol{r}^N(t), \boldsymbol{p}^N(t)\right)$, with a scalar product or equilibrium average defined by

$$\langle B, A^* \rangle = \int f_0(\Gamma) B(\Gamma) A^*(\Gamma)\, d\Gamma, \tag{3.29}$$

where f_0 be the equilibrium phase distribution function for any microcanonical, canonical or isobaric-isoenthalpic ensemble. Phase variable B doesn't depend explicitly upon time and its rate of change is given by

$$\dot{B}(\Gamma) = \dot{\Gamma} \cdot \frac{\partial}{\partial \Gamma} B = iL(\Gamma) B(\Gamma), \tag{3.30}$$

where operator $iL(\Gamma)$ is termed as p-Liouvillean. The solution for the eq. (3.30) is

$$B(t) = \exp\left[iLt\right] B(0), \tag{3.31}$$

where $\exp\left[iLt\right]$ is termed as *p-propagator*. Now, we will defining a projector operator which transforms B to a vector which has no correlation with the dynamic variable A. The component of B parallel to A is given by the projection operator P as

$$PB(\Gamma(t)) = \frac{\langle B(\Gamma(t)), A^*(\Gamma) \rangle}{\langle A(\Gamma), A^*(\Gamma) \rangle} A\left(\Gamma\right). \tag{3.32}$$

We define another operator $Q = 1 - P$, complement of P, which defines the component of B orthogonal to A as QB. Clearly,

$$\langle QB(t), A^* \rangle = \langle B(t) - \frac{\langle B(t), A^* \rangle}{\langle A, A^* \rangle} A, A^* \rangle \tag{3.33}$$

$$= \langle B(t), A^* \rangle - \frac{\langle B(t), A^* \rangle}{\langle A, A^* \rangle} \langle A, A^* \rangle = 0. \tag{3.34}$$

Using above equations of projectors $PP = P$, $QQ = Q$ and $PQ = QP$. The direct and random parts of p-Liouvillean iL are iPL and iQL, which define the corresponding random and direct propagators, $\exp\left[iPLt\right]$ and $\exp\left[iQLt\right]$. Now Dyson equation [100] can be used to relate these propagators:

$$\exp\left[iLt\right] = \exp\left[iQLt\right] + \int_0^t \exp\left[iL(t-\tau)\right] iPL \exp\left[iQL\tau\right] d\tau \tag{3.35}$$

Using eq. (3.31), the time-derivative of $A(t)$ becomes:

$$\frac{dA(t)}{dt} = \exp\left[iLt\right] iLA(0) = \exp\left[iLt\right] i(Q+P)LA(0). \tag{3.36}$$

Defining the frequency operator $i\Omega$ as

$$\exp\left[iLt\right]iPLA(0) = \frac{\langle iLA, A^*\rangle}{\langle A, A^*\rangle}\exp\left[iLt\right]A(0) = i\Omega A(t), \tag{3.37}$$

and using Eq. (3.35), and then taking $\exp\left[iQLt\right]iQLA(0)$ as the random force $R(t)$, because

$$\langle R(t), A^*\rangle = \langle \exp\left[iQLt\right]iQLA(0), A^*\rangle = \langle QR(t), A^*\rangle = 0. \tag{3.38}$$

Here, we have used the property $QQ = Q$ and Eq. (3.34) for arbitrary phase variable R. Further, using the properties of projectors and above equations, and then setting the term $\frac{\langle R(0),R(0)^*\rangle}{\langle A,A^*\rangle}$ as the memory kernel $M(t)$, we can show that

$$\frac{dA(t)}{dt} = i\Omega A(t) - \int_0^t M(\tau)A(t-\tau)\,d\tau + R(t). \tag{3.39}$$

This is the *generalized Langevin Equation*. Multiplying both sides of this equation by $A^*(0)$ and taking ensemble average gives

$$\frac{dC(t)}{dt} = i\Omega C(t) - \int_0^t M(\tau)C(t-\tau)\,d\tau, \tag{3.40}$$

where $C(t)$ be the equilibrium autocorrelation function for A, defined by $C(t) = \langle A(t)A^*(0)\rangle$.

Now we will be showing how classical Langevin equation is obtained. Take the phase variable A as single component $p_{i\alpha}$, a component of the generalized momentum vector of a particle in α direction. This makes Eq. (3.39) of this form in Cartesian coordiantes:

$$\dot{p}_{i\alpha}(t) = -\int_0^t M(\tau)p_{i\alpha}(t-\tau)\,d\tau + R_{i\alpha}(t), \tag{3.41a}$$

$$r_{i\alpha} = p_{i\alpha}/m_i \tag{3.41b}$$

where random force $R_{i\alpha}(t) = \exp\left[iQLt\right]iQLp_{i\alpha}(0)$ Assume that elements of the memory kernel $M(t)$ are proportional to Dirac delta function of time $\delta(t)$. Then we have,

$$\langle R_{i\alpha}(t)R_{i\alpha}(0)\rangle = M(t)\langle {p_{i\alpha}}^2\rangle = 2\xi\delta(t)\langle {p_{i\alpha}}^2\rangle = 2m_i k_B\theta\xi\delta(t), \tag{3.42}$$

where ξ is friction coefficient. Also using delta function approximation for $M(t)$, the equation of motion gives classical Langevin equation:

$$\dot{p}_{i\alpha}(t) = -\xi\, p_{i\alpha}(t) + R_{i\alpha}(t). \tag{3.43}$$

Also, the momentum autocorrelation function $C(t) = \langle p_{i\alpha}(t) p_{i\alpha}(0) \rangle$ has the solution:

$$C(t) = \langle {p_{i\alpha}}^2 \rangle \exp -\xi t. \tag{3.44}$$

For eq. (3.43) to be treated as simulation, the statistical properties of the random force $R_{i\alpha}(t)$ must be completely specified. Usually, $R_{i\alpha}(t)$ is assumed to be a normal random process. The linear form of Eq. (3.41b) gives Maxwellian velocity distribution. For this random process [106], and any function $g(t)$, the variable

$$\delta p_{i\alpha} = \int_t^{t+\delta t} g(\tau) R_{i\alpha}(\tau)\, d\tau \tag{3.45}$$

is a random variable with a normal distribution function

$$f(\delta p_{i\alpha}) = \frac{1}{\sigma\sqrt{2\pi}} \exp\{-\frac{(\delta p_{i\alpha})^2}{2\sigma^2}\} \tag{3.46}$$

with zero mean and variance

$$\sigma^2 = 2\xi m_i k_B \theta \int_t^{t+\delta t} g^2(\tau)\, d\tau. \tag{3.47}$$

For a system of N interacting particles, we add force acting on each particle in Eq. (3.43) to get equations for each particle:

$$\boxed{\dot{\boldsymbol{p}}_i(t) = \boldsymbol{f}_i - \xi\, \boldsymbol{p}_i(t) + \boldsymbol{R}_i(t)}. \tag{3.48}$$

Friction coefficient ξ is scalar and doesn't depend upon particles position and momenta, but may depend upon the nature of particles. Usually, even for all the particles, they are set a constant value. The random forces $\boldsymbol{R}_i(t)$ are independent of each other for $i = 1, \ldots, N$ and each vectorial component satisfies equations Eqs. (3.42), (3.45)-(3.47). The random forces $\boldsymbol{R}_i(t)$ are uncorrelated with the velocities $\dot{\boldsymbol{r}}^N(\tau)$ and conservative forces $\boldsymbol{f}_i(t)$ at previous time $\tau < t$; their time-averages are zero, and

$$\langle R_{i\alpha}(t) R_{j\nu}(\tau) \rangle = 2\, m_i\, k_B\, \theta\, \xi\, \delta_{ij}\, \delta_{\alpha\nu}\, \delta(t - \tau). \tag{3.49}$$

It can be showed that a trajectory generated by Langevin equation maps a canonical distribution at constant volume corresponding to the target temperature θ. The Langevin equation is smooth, non-deterministic and irreversible. If the friction coeffs are two low, then after a very long evolution, canonical distribution will be achieved, but that may drift the total energy away from the desired results. On the other hand, too large friction coefficients may cause large random and frictional forces to interfere with the system in a great detail. So a trade-off is required.

3.1.8 Nosé Hoover Thermostat

Nosé [107, 108] discovered a most unusual temperature-dependent Hamiltonian for thermostatting number of degrees of freedom, where deterministic instead of stochastic Molecular Dynamics at constant temperature can be performed, so that equations of motion become time-reversible. It uses the concept of extended Lagrangian by introducing additional coordinate s, which Nosé interpreted as "time-scaling" . The new Lagrangian becomes:

$$L_{Nose} = \sum_{i=1}^{N} \frac{1}{2} m_i \, s^2 \, \dot{\boldsymbol{r}}_i^2 - V(\boldsymbol{r}^N) + \frac{M}{2} \dot{s}^2 - \frac{l}{\beta} \ln s, \tag{3.50}$$

where l is a parameter and M is an "effective mass" associated to s. The corresponding Hamiltonian becomes:

$$H_{Nose} = \sum_{i=1}^{N} \frac{1}{2m_i} \left(\frac{\boldsymbol{p}_i}{s} \right)^2 + V(\boldsymbol{r}^N) + \frac{p_s^2}{2M} + \frac{l}{\beta} \ln s, \tag{3.51}$$

corresponding to the momenta $\boldsymbol{p}_i = \frac{\partial L}{\partial \dot{\boldsymbol{r}}_i} = m_i \, s^2 \dot{\boldsymbol{r}}_i$ and $p_s = \frac{\partial L}{\partial \dot{s}} = M \dot{s}$. This Hamiltonian gives the following equations of motion:

$$\begin{aligned}
\dot{\boldsymbol{r}}_i &= \frac{\partial H_{Nose}}{\partial \boldsymbol{p}_i} = \frac{\boldsymbol{p}_i}{m_i \, s^2} \\
\dot{\boldsymbol{p}}_i &= -\frac{\partial H_{Nose}}{\partial \boldsymbol{r}_i} = -\frac{\partial V(\boldsymbol{r}^N)}{\partial \boldsymbol{r}_i} \\
\dot{s} &= \frac{\partial H_{Nose}}{\partial p_s} = p_s / M \\
\dot{p_s} &= \frac{\partial H_{Nose}}{\partial s} = \sum \left[\frac{p_i^2}{m_i \, s^3} - \frac{l}{\beta \, s} \right].
\end{aligned}$$

Clearly, the equations of motion are smooth, deterministic and time-reversible. Writing the above equations in a new set of "time-scaled" variables $r' = r$, $p' = p/s$, $s' = s$ and

$\delta t' = \delta t/s$, the new equations take this form:

$$\frac{d\boldsymbol{r'}_i}{dt'} = \frac{\boldsymbol{p'}_i}{m_i} \tag{3.52a}$$

$$\frac{d\boldsymbol{p'}_i}{dt'} = -\frac{\partial V(\boldsymbol{r'}^N)}{\partial \boldsymbol{r'}_i} - \xi\, \boldsymbol{p'}_i \tag{3.52b}$$

$$\frac{d\xi}{dt} = \frac{1}{M} \sum \left[\frac{p'^2_i}{m_i} - \frac{l}{\beta} \right] \tag{3.52c}$$

$$\frac{1}{s}\frac{ds'}{dt'} = \xi \tag{3.52d}$$

where $\xi = \frac{s'p'_s}{M}$ is the thermodynamic friction coefficient. By using friction coeffiecient ξ, Hoover [109, 110] showed the importance of the scaled equations of motion and complete irrelevance of the scaling variable s, as the last Eq. (3.52d) in the above set is redundant. For these equations, the following quantity is conserved:

$$H'_{Nose} = \sum_{i=1}^{N} \frac{1}{2m_i} \boldsymbol{p'}_i{}^2 + V(\boldsymbol{r'}^N) + \frac{\xi^2 M}{2} + \frac{l}{\beta} \ln s'. \tag{3.53}$$

This conserved term H'_{Nose} is not a Hamiltonian because equations of motion are not derivable from it, therefore, Nosé-Hoover thermostat is a non-Hamiltonian thermostat. This thermostat is global since the temperature is defined globally as the same friction coefficient in Eq. (3.52c) is used for all the particles and then an ensemble of particles are enforced to maintain an average internal kinetic energy over time. One can show that this extended system indeed generates canonical ensemble [88], provided there is only one constant of motion, for example, presently it is H'_{Nose}. In the case of more than one conservation laws or the case where there is no external force field but the center of mass doesn't remain fixed, Nosé-Hoover chain algorithm is used [88, 111]. Here the thermostatted variable is thermostatted by another thermostatting variable and thus all thermostatting variables form a chain. Some modifications are done in the algorithm to generate NPT ensemble [88].

3.1.9 Binning for spatial and temporal averaging

The integration of the equations of motion by MD provides the positions and momenta of all particles in the system as a function of time. We are interested in computing the time-dependent profiles along the beam of thermodynamic properties such as the temperature

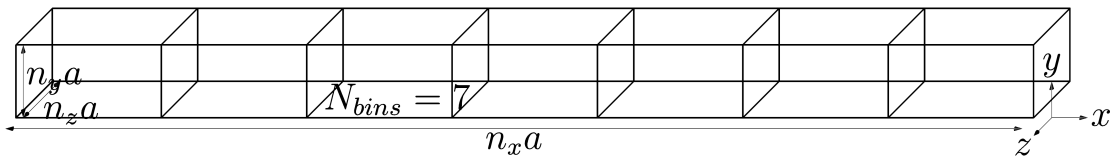

Figure 3.2: Division of the nanobeam into bins.

$\theta(x,t)$ and heat flux $\boldsymbol{q}(x,t)$. Such profiles are needed for computing thermal properties and also for the imposition of thermal BCs. In order to do so, we divide the beam into N_{bins} bins of equal size as shown for example in Fig. 3.2 for $N_{\text{bins}} = 7$. The value of a thermodynamic property is then obtained as a spatial average over an appropriate phase function across all atoms in a bin. For example the instantaneous temperature of bin n is

$$\theta_n^{\text{inst}} = \frac{2\mathcal{K}}{3N_n k_{\text{B}}}, \tag{3.54}$$

where $\mathcal{K}$ is kinetic energy (with rigid-motion removed [93]) of all N_n atoms in bin n and k_{B} is Boltzmann's constant. The temperature follows as the phase average of the instantaneous temperature which in an MD simulation is obtained by performing a time average:

$$\theta_n(t) = \left\langle \theta_n^{\text{inst}} \right\rangle = \frac{1}{\Delta_t} \int_t^{t+\Delta_t} \theta_n^{\text{inst}}(\tau)\, d\tau. \tag{3.55}$$

In this relation Δ_t is a time interval which must be taken sufficiently long to ensure that *local thermodynamic equilibrium* (LTE) is established but not so long as to smear out nonequilibrium effects. The basic assumption in LTE is that during a nonequilibrium process, there exists a timescale over which thermodynamic variables such as temperature are well-defined and obey standard thermodynamic relations such as equations of state [84]. The TPI approach for parameter extraction described below assumes that LTE exists so that temperature profiles are meaningful and can be used in a curve fitting procedure.

The objective is then to find the smallest value of Δ_t for which LTE is established. To test for LTE, we compute the relative fluctuation defined by

$$\Delta_{\text{r.f.}} = \max\{\delta\theta_n/\theta_n;\ n = 1, \ldots, N_{\text{bins}}\}, \tag{3.56}$$

where $\delta\theta_n$ is the fluctuation (or standard error) of the temperature in bin n,

$$\delta\theta_n = \left[\langle(\theta_n^{\text{inst}})^2\rangle - \langle\theta_n^{\text{inst}}\rangle^2\right]^{1/2}. \tag{3.57}$$

If the maximum relative fluctuation $\Delta_{\text{r.f.}}$ is sufficiently small, for example [42] less than 1%, then it can be assumed that the LTE assumption is satisfied. In order to improve the statistics, and reduce the necessary Δ_t, simulations can be repeated multiple times with different initial conditions drawn from a distribution associated with the initial temperature. Bin averages are then computed over all realizations of a given bin. This reduces the fluctuation $\delta\theta_n$ and therefore allows for a smaller averaging time interval.

3.2 Standard methods for calculating thermal properties

The non-Fourier Jeffreys-type model described in Chapter 2 includes three material parameters: the steady-state thermal conductivity k and two relaxation times τ_q and τ_θ. Two standard approaches for calculating k are (1) the Green-Kubo method using equilibrium MD, and (2) the "direct method" using NEMD. These approaches are described below, followed in Section 3.2.3 by the TPI method which obtains all three non-Fourier parameters.

3.2.1 Green-Kubo method

The Green-Kubo method is based on the fluctuation-dissipation theorem. The thermal conductivity is[2]

$$\boldsymbol{k} = \frac{1}{Vk_{\text{B}}\theta^2}\int_0^\infty \langle \boldsymbol{J}(t)\otimes\boldsymbol{J}(0)\rangle_{\boldsymbol{\nabla}\theta=0}\, dt, \tag{3.58}$$

where V is the volume and $\boldsymbol{J} = V\boldsymbol{q}$ is the microscopic heat current. For practical calculations, the thermal conductivity tensor in Eq. (3.58) can also be written as [40]

$$\begin{aligned}\boldsymbol{k} &= \lim_{\tau_I\to\infty}\frac{1}{Vk_{\text{B}}\theta^2}\int_0^{\tau_I}\langle \boldsymbol{J}(t)\otimes\boldsymbol{J}(0)\rangle_{\boldsymbol{\nabla}\theta=0}\, dt \\ &= \lim_{\substack{S,I\to\infty\\ S\gg I}}\frac{\Delta t_{\text{MD}}}{Vk_{\text{B}}\theta^2}\sum_{a=1}^{I}\frac{1}{S-a}\sum_{b=1}^{S-a}\boldsymbol{J}_{a+b}\otimes\boldsymbol{J}_b,\end{aligned} \tag{3.59}$$

[2] This expression is obtained by writing the energy equation in terms of fluctuations around the equilibrium value in the linear regime and the wave-vector-dependent internal energy density autocorrelation function. A more detailed analysis is available in Ref. [100].

where Δt_{MD} is the MD time step, S is the total number of simulation steps, I is the total number of integration steps, τ_I is the integration time ($\tau_I = I\Delta t_{\mathrm{MD}}$), and $\boldsymbol{J}_m = \boldsymbol{J}(m\Delta t_{\mathrm{MD}})$. In order to obtain a bulk property, τ_I must be very large, i.e., I must be a large number.

We consider a system of N atoms with mass m_i and position $\boldsymbol{r}_i$. The distance between atoms i and j is $r_{ij} = \|\boldsymbol{r}_j - \boldsymbol{r}_i\|$. The velocity of atom i relative to the center-of-mass velocity of the nanobeam (or bin) is denoted $\tilde{\boldsymbol{v}}_i$. For pair potential interactions, the heat current $\boldsymbol{J}$ is [39, 112, 113, 114],

$$\boldsymbol{J} = \sum_{i=1}^{N} e_i \tilde{\boldsymbol{v}}_i + \sum_{\substack{i,j \\ i<j}}^{N} \left[\boldsymbol{f}_{ij} \cdot \frac{\tilde{\boldsymbol{v}}_i + \tilde{\boldsymbol{v}}_j}{2} \right] (\boldsymbol{r}_i - \boldsymbol{r}_j). \tag{3.60}$$

Here e_i is the local site energy of atom i which includes both kinetic and potential terms. For a monoatomic system with pair potential interactions this is

$$e_i = \frac{1}{2}\, m_i\, \tilde{\boldsymbol{v}}_i^2 + \frac{1}{2} \sum_{\substack{j \\ j\neq i}}^{N} \phi_2(r_{ij}), \tag{3.61}$$

where $\phi_2(r)$ is the pair potential function. Also appearing in Eq. (3.60), $\boldsymbol{f}_{ij}$ is the force on atom i due to the presence of atom j. For a pair potential this is

$$\boldsymbol{f}_{ij} = \phi_2'(r_{ij}) \frac{\boldsymbol{r}_j - \boldsymbol{r}_i}{r_{ij}}. \tag{3.62}$$

For the interatomic potential involving 3 body terms, such as the Stillinger-Weber (SW) potential [115], the heat current can be written as

$$\boldsymbol{J} = \sum_{i=1}^{N} e_i \tilde{\boldsymbol{v}}_i + \sum_{\substack{i,j \\ i<j}}^{N} \left[\boldsymbol{f}_{ij} \cdot \frac{\tilde{\boldsymbol{v}}_i + \tilde{\boldsymbol{v}}_j}{2} \right] (\boldsymbol{r}_i - \boldsymbol{r}_j) + \frac{1}{6} \sum_{i=1}^{N} \sum_{\substack{j=1 \\ j\neq i}}^{N} \sum_{\substack{k=1 \\ k\neq i,j}}^{N} \left(\boldsymbol{f}_{ijk} \cdot \tilde{\boldsymbol{v}}_i \right) (\boldsymbol{r}_{ij} + \boldsymbol{r}_{ik}), \tag{3.63}$$

where three-body force term $\boldsymbol{f}_{ijk} = -\nabla_i \phi_3 \left(\boldsymbol{r}_i, \boldsymbol{r}_j, \boldsymbol{r}_k \right)$ is the result of three-body potential function as defined in Eqs. (3.2) and (3.3). Rest of the terms are the same as for pairwise potential except the local site energy e_i, which is given by

$$e_i = \frac{1}{2}\, m_i\, \tilde{\boldsymbol{v}}_i^2 + \frac{1}{2} \sum_{\substack{j \\ j\neq i}}^{N} \phi_2(r_{ij}), + \frac{1}{6} \sum_{i=1}^{N} \sum_{\substack{j=1 \\ j\neq i}}^{N} \sum_{\substack{k=1 \\ k\neq i,j}}^{N} \phi_3 \left(\boldsymbol{r}_i, \boldsymbol{r}_j, \boldsymbol{r}_k \right). \tag{3.64}$$

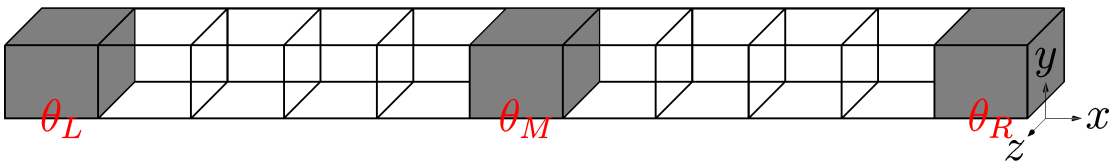

Figure 3.3: Schematic diagram of a beam partitioned into bins with periodic BCs. Shaded regions are thermostatted.

3.2.2 Direct method

In the direct method, a temperature gradient is created in the nanobeam by thermostatting the left and right ends of the nanobeam at the same temperature, i.e. $\theta_{\mathrm{L}} = \theta_{\mathrm{R}}$, and maintaining the middle bin at a temperature θ_{M} (see Fig. 3.3) with periodic BCs applied in all directions. Thus for a nanobeam of length L, the BCs are

$$\theta\left(0,t\right) = \theta_{\mathrm{L}}, \quad \theta\left(L,t\right) = \theta_{\mathrm{R}}, \quad \theta\left(L/2,t\right) = \theta_{\mathrm{M}}. \tag{3.65}$$

The temperature gradients to the left and right of the middle bin are calculated by fitting straight lines to the steady-state temperature profiles in the regions away from thermostats. For this purpose, the two nearest bins to each thermostatted bin are excluded from the linear fitting. Then the thermal conductivity along the x direction is estimated from Eq. (1.1) as

$$k = \frac{1}{2}\left(\langle q\rangle_{\mathrm{L}}\left(\frac{\Delta\theta}{\Delta x}\right)_{\mathrm{L}}^{-1} + \langle q\rangle_{\mathrm{R}}\left(\frac{\Delta\theta}{\Delta x}\right)_{\mathrm{R}}^{-1}\right), \tag{3.66}$$

where the x-component of the heat flux vector is obtained from Eq. (3.60) ($q = J_x/V_{\mathrm{bin}}$, where V_{bin} is the volume of each bin) and $\Delta\theta/\Delta x$ is the temperature gradient obtained from the linear fit. The subscripts L and R refer to left and right sides of the nanobeam, and $\langle q\rangle$ represents the average of the x-component of the heat flux vector of all bins included in the linear fitting.

The thermal conductivity depends on the length (size) of the beam for two reasons [40, 116, 117]: (a) shorter nanobeams have fewer phonon modes available and therefore include less phonon-phonon scatterings; (b) when the nanobeam length is smaller than the bulk phonon mean-free paths, phonon-boundaries scattering effects increase significantly.

3.2.3 Regression-based thermal parameter identification

In the TPI approach, an NEMD simulation is performed starting with initial conditions similar to Daly et al. [55], in which the nanobeam has a sinusoidal temperature distribution of the form:

$$\theta(x,0) = \theta_0 + \Delta\theta_0 \cos(2\pi x/L), \qquad 0 \leq x \leq L, \tag{3.67}$$

where θ_0 and $\Delta\theta_0$ are the initial temperature and fluctuation amplitude. The initial temperature profile is applied by dividing the nanobeam into bins (as shown in Fig. 3.2) and individually thermostatting each bin in accordance with Eq. (3.67). The thermostats are then switched off and the nanobeam is left to evolve freely subject to periodic BCs, $\theta(0,t) = \theta(L,t)$, for $t \geq 0$. The relaxation of the temperature and heat flux profiles are analyzed to calculate the thermal parameters by comparing to the following analytical solution for the non-Fourier models.

Given the slender nanobeam geometry, we approximate the three-dimensional heat transfer problem as 1D. Using the expression for the speed of the heat waves, we rewrite Eq. (2.39) in 1D as

$$\tau_q \frac{\partial^2\theta}{\partial t^2} + \frac{\partial\theta}{\partial t} = \frac{k}{\gamma}\frac{\partial^2\theta}{\partial x^2} + \frac{k}{\gamma}\tau_\theta \frac{\partial^3\theta}{\partial x^2 \partial t}. \tag{3.68}$$

Since there are no heat sources in the system, it is reasonable to assume that the temperature rate of change at time $t = 0$ is zero, i.e.,

$$\frac{\partial\theta}{\partial t}(x,0) = 0, \qquad 0 \leq x \leq L. \tag{3.69}$$

Rather than solving for $\theta : (0,L) \times (0,+\infty) \to \mathbb{R}_+$, where $\mathbb{R}_+$ is the set of non-negative real numbers, we solve for the perturbation $\phi(x,t)$ in the temperature from the mean temperature θ_0, defined as $\phi(x,t) := \theta(x,t) - \theta_0$. We thus seek to solve,

$$\begin{cases} \tau_q \frac{\partial^2\phi}{\partial t^2} + \frac{\partial\phi}{\partial t} = \alpha\frac{\partial^2\phi}{\partial x^2} + \alpha\tau_\theta \frac{\partial^3\phi}{\partial x^2\partial t} & , \\ \phi(0,t) = \phi(L,t), & t \geq 0, \\ \phi(x,0) = \Delta\theta_0 \cos(2\pi x/L), & 0 \leq x \leq L, \\ \frac{\partial\phi}{\partial t}(x,0) = 0, & 0 \leq x \leq L. \end{cases} \tag{3.70}$$

where $\alpha = k/\gamma$ is thermal diffusivity. Using the method of separation of variable, we can write all solutions of the above problem in the special form $\phi(x,t) = X(x)T(t)$, where $X(x)$ and $T(t)$ are unknown functions of x and t. Substituting this into Eq. (3.70), we obtain

$$\begin{aligned} \left[\tau_q \ddot{T}(t) + \dot{T}(t)\right] X(x) &= \alpha X''(x) \left[T(t) + \tau_\theta \dot{T}(t)\right], \\ \implies \frac{X''(x)}{X(x)} &= \frac{1}{\alpha} \frac{\tau_q \ddot{T}(t) + \dot{T}(t)}{T(t) + \tau_\theta \dot{T}(t)} = -\omega^2, \end{aligned} \tag{3.71}$$

where ω is the separation constant independent of x and t. Using the initial and boundary conditions in Eq. (3.70), Eq. (3.71) leads to two separate problems:

$$\begin{cases} X''(x) + \omega^2 X(x) = 0, \\ X(0) = X(L), X(x) = \Delta\theta_0 \cos(2\pi x/L), \end{cases} \tag{3.72}$$

and

$$\begin{cases} \tau_q \ddot{T}(t) + \left(1 + \omega^2 \alpha \tau_\theta\right) \dot{T}(t) + \omega^2 \alpha T(t) = 0, \\ T(0) = 1, \dot{T}(0) = 0. \end{cases} \tag{3.73}$$

The solution to Eq. (3.72) is $X(x) = \Delta\theta_0 \cos(\omega x)$, with $\omega = 2\pi/L$. The solution to Eq. (3.73) is

$$T(t;\lambda_i) = \begin{cases} e^{\lambda_1 t}\left(\cos\lambda_2 t - \frac{\lambda_1}{\lambda_2}\sin\lambda_2 t\right), & \text{if } \lambda_2^2 > 0, \\ \frac{e^{\lambda_1 t}}{2\lambda_3}\left[(\lambda_3 - \lambda_1)e^{\lambda_3 t} + \right. & \\ \quad \left.(\lambda_3 + \lambda_1)e^{-\lambda_3 t}\right], & \text{if } \lambda_2^2 < 0, \\ e^{\lambda_1 t}\left(1 - \lambda_1 t\right), & \text{if } \lambda_2^2 = 0, \end{cases} \tag{3.74}$$

where λ_i; $i = 1, 2, 3$, are parameters defined by

$$\lambda_1 = -\frac{1}{2\tau_q}\left(1 + \omega^2\alpha\tau_\theta\right), \lambda_2 = \sqrt{\omega^2\frac{\alpha}{\tau_q} - \lambda_1^2}, \lambda_3^2 = -\lambda_2^2. \tag{3.75}$$

Thus the solution to the Jeffreys-type model in Eq. (3.68) subject to the initial conditions in Eqs. (3.67) and (3.69) under periodic BCs is given by

$$\theta(x,t) = \theta_0 + \Delta\theta_0 \cos(2\pi x/L)\, T(t), \quad 0 \le x \le L, \tag{3.76}$$

where $T(t)$ is given by Eq. (3.74). The existence, uniqueness and stability of the solution in Eq. (3.76) is demonstrated in the Appendix A.

We will also require an expression for the x-component of the heat flux vector. We start with a 1D version of Eq. (2.37):

$$q(x,t) = -k_1 \frac{\partial \theta}{\partial x}(x,t) - \frac{k_2}{\tau_q} \int_0^t \frac{\partial \theta}{\partial x}(x,t') e^{-(t-t')/\tau_q} dt', \tag{3.77}$$

where the lower limit in the integral is $t' = 0$, since the initial conditions are known at this time.[3] Substituting Eq. (3.76) into Eq. (3.77), we obtain

$$q(x,t) = \pi \Delta\theta_0 \sin(2\pi x/L) \left[Q(t) + k_1 e^{-t/\tau_q} \right], \tag{3.78}$$

where $k_1 = k\tau_\theta/\tau_q$, $k_2 = k - k_1$, and

$$Q(t;\lambda_i) = \tag{3.79}$$

$$\begin{cases} \frac{e^{\lambda_1 t}}{\lambda_2} \frac{k}{\tau_q} \sin \lambda_2 t, & \text{if } \lambda_2^2 > 0, \\ \frac{e^{\lambda_1 t}}{2\lambda_3} \left[\left(k_1 + \frac{k_2}{\tau_q(\lambda_1+\lambda_3)+1} \right) (\lambda_3 - \lambda_1) e^{\lambda_3 t} + \right. & \\ \left. \left(k_1 + \frac{k_2}{\tau_q(\lambda_1-\lambda_3)+1} \right) (\lambda_3 + \lambda_1) e^{-\lambda_3 t} \right], & \text{if } \lambda_2^2 < 0, \\ -e^{\lambda_1 t} \left(k_1 + \frac{k_2}{\tau_q \lambda_1 + 1} \right) \lambda_1 t, & \text{if } \lambda_2^2 = 0. \end{cases} \tag{3.80}$$

Next, we introduce the cosine average of temperature over the length of the nanobeam:

$$\bar{\theta}(t) := \frac{2}{L} \int_0^L \theta(x,t) \cos(2\pi x/L) dx. \tag{3.81}$$

Substituting θ from Eq. (3.76) into Eq. (3.81), we obtain

$$\bar{\theta}(t)/\Delta\theta_0 = T(t), \quad t \geq 0. \tag{3.82}$$

Similarly, we introduce the sine average of the x-component of heat flux vector:

$$\bar{q}(t) := \int_0^L q(x,t) \sin(2\pi x/L) dx. \tag{3.83}$$

Substituting q from Eq. (3.78) into Eq. (3.83), we obtain

$$\bar{q}(t)/\pi\Delta\theta_0 = Q(t) + k_1 e^{-t/\tau_q}, \quad t \geq 0. \tag{3.84}$$

[3] It can be shown that despite the change in the integration bounds, the Jeffreys-type model in Eq. (2.38) is still obtained by differentiating Eq. (3.77) with respect to time t.

The CV model has similar solutions for $\bar{\theta}(t)$ and $\bar{q}(t)$ as in Eqs. (3.82) and (3.84) with different coefficients λ_i; $i = 1, 2, 3$ obtained by setting $\tau_\theta = 0$ in Eq. (3.75). For the Fourier model, we have

$$\bar{\theta}(t)/\Delta\theta_0 = e^{-\omega^2\alpha t}, \quad t \geq 0, \tag{3.85}$$

$$\bar{q}(t)/\pi\Delta\theta_0 = ke^{-\omega^2\alpha t}, \quad t \geq 0, \tag{3.86}$$

where $\omega = 2\pi/L$.

The binning procedure in Section 3.1.9 is used to obtain the temperature and heat flux of each bin at discrete time intervals. The resulting spatio-temporal temperature and heat flux profiles are used to calculate $\bar{\theta}(t)$ and $\bar{q}(t)$ using Eqs. (3.81) and (3.83). Then, the nonlinear function $T(t; \lambda_i)$ in Eq. (3.74) is fit to the calculated dependent variable $y = \bar{\theta}(t)/\Delta\theta_0$ appearing in Eq. (3.82) to calculate the model parameter vector $\boldsymbol{\lambda} = (\lambda_1, \lambda_2, \lambda_3)$. Thus we have y_m at each time $t_m = m\Delta_t$ $(m = 1, 2, \ldots, N_{\text{profiles}})$, where N_{profiles} is the number of stored temperature profiles. Assuming the parameters $\boldsymbol{\lambda}$ are constant over the range of temperatures being explored, the following relationship exists between y_m and t_m,

$$y_m = T(t_m; \boldsymbol{\lambda}) + R_m, \tag{3.87}$$

where R_m are residual terms representing the noise in the data. In order to obtain the parameters $\boldsymbol{\lambda}$, a nonlinear regression method is used to minimize the sum of the square of the residuals:

$$\min_{\boldsymbol{\lambda}} \sum_m R_m(\boldsymbol{\lambda})^2 = \min_{\substack{\boldsymbol{\lambda} \\ \forall i=1,2,3}} \sum_m (y_m - T_i(t_m; \boldsymbol{\lambda}))^2, \tag{3.88}$$

where $T_i(t_m)$; $i = 1, 2, 3$, corresponds to $T(t)$ for the three different cases of Eq. (3.74) depending upon whether λ_2^2 is positive, negative or zero. The value of λ_2 is unknown a priori, therefore we minimize the sum of residuals for all three cases and select the λ_2 value for which the sum of residuals is minimal.

Once the parameters λ_i are known, Eq. (3.75) provides a system of two equations for the three unknowns $\alpha = k/\gamma$, τ_θ and τ_q. If we are fitting the CV model, then $\tau_\theta = 0$, and we can solve for the remaining coefficients:

$$k = \gamma(\lambda_1^2 + \lambda_2^2)\frac{\tau_q}{\omega^2}, \quad \tau_q = -\frac{1}{2\lambda_1}. \tag{3.89}$$

For the Jeffreys-type model, we can solve for k and τ_θ in terms of τ_q:

$$k = \gamma(\lambda_1^2 + \lambda_2^2)\frac{\tau_q}{\omega^2}, \quad \tau_\theta = -\frac{1 + 2\tau_q\lambda_1}{(\lambda_1^2 + \lambda_2^2)\tau_q}. \tag{3.90}$$

Substituting these relations and the values of λ_i into Eq. (3.80), we rewrite $Q = \widehat{Q}(t;\tau_q)$ in terms of τ_q. Thus Eq. (3.84) becomes

$$\bar{q}(t;\tau_q)/\pi\Delta\theta_0 = \tilde{Q}(t;\tau_q), \quad t \geq 0, \tag{3.91}$$

where $\tilde{Q}(t;\tau_q) = \widehat{Q}(t;\tau_q) - \gamma\frac{1+2\tau_q\lambda_1}{\omega^2\tau_q}e^{-t/\tau_q}$. In order to determine the parameter τ_q, we fit the nonlinear function $\tilde{Q}(t;\tau_q)$ to the dependent variable $z = \bar{q}/\pi\Delta\theta_0$ appearing in Eq. (3.91). This leads to the following relation,

$$z_m = \tilde{Q}(t_m;\tau_q) + \tilde{R}_m, \tag{3.92}$$

where z_m is the value of the dependent variable at time $t_m = m\Delta_t$ ($m = 1, 2, \ldots, N_{\text{profiles}}$), and $\tilde{R}_m$ is the corresponding residual term. Since the λ_i values and the form of $\tilde{Q}$ are known, τ_q can be solved using a nonlinear regression method:

$$\min_{\tau_q} \sum_m \tilde{R}_m(\tau_q)^2 = \min_{\tau_q} \sum_m (z_m - \tilde{Q}(t_m;\tau_q))^2, \tag{3.93}$$

subject to the constraint $(\tau_q, k, \tau_\theta) \geq (0, 0, 0)$. Finally, Eq. (3.90) is used to calculate k and τ_θ.

3.3 Summary

To summarize, we have first provided the nuts and bolts of the equilibrium and nonequilibrium molecular dynamics. Then we propose different methods to compute the thermal conductivity of the system. We also develop a novel method to compute the conductivity as well as time lag parameters for the non-Fourier models with the help of the sinusoidal temperature and flux profiles.

Chapter 4

Numerical results

In order to test the methods described in Chapter 3, MD and NEMD simulations were carried out on argon nanobeams. The atomic interactions were modeled using a LJ pair potential [85, 86] with LJ parameters [118] $\sigma = 3.4$ Å and $\epsilon = 0.01025423$ eV, and a simple truncation cutoff, i.e., $\phi(r) = 0$ for $r \geq r_{\text{cut}}$, archived in OpenKIM [119, 120, 121]. The cutoff radius was taken to be $r_{\text{cut}} = 4.5\sigma = 15.3$ Å. Temperature BCs were applied using either a Nosé-Hoover chain thermostat [88, 107, 108, 109, 110, 111] or a Langevin thermostat [100, 122] using a definition for the temperature which is invariant with respect to rigid-body motions due to Jellinek and Li [93]. The parallel MD code LAMMPS [123, 124] was used to integrate the equations of motion with the following modifications: (a) temperature calculations employed the Jellinek and Li [93] approach mentioned above; (b) the binning procedure of Section 3.1.9 was used instead of a similar feature in LAMMPS called "layers"[1] ; and (c) heat-flux was computed for each bin after removing rigid-body translation.[2]

[1] In the LAMMPS implementation the number of layers (bins) changes during the simulation, which is undesirable for the TPI approach.

[2] It was observed that the removal of rigid-body rotation did not significantly affect the temperature and heat-flux values; therefore in order to save computational time only rigid-body translation was removed in most cases.

4.1 Initialization

All simulations begin with an initialization stage during which the system is equilibrated to the initial target temperature θ_0 and allowed to expand to its equilibrium volume. The argon nanobeam has an fcc structure and is oriented so that the x, y and z axes coincide with the crystallographic [100], [010] and [001] directions. A nanobeam of size $n_x a_0 \times n_y a_0 \times n_z a_0$ (with $n_y = n_z$) is constructed, where $a_0 = 5.26$ Å is the zero-temperature equilibrium constant for argon. Periodic BCs are applied in all directions. The initial momenta of all the atoms are selected from a Maxwell-Boltzmann distribution for twice the target temperature ($2\theta_0$). This is done because approximately half of the initial kinetic energy is transformed to potential energy due to the equipartition of energy, and so the final temperature after equilibration will be about θ_0. The velocities of the atoms are adjusted to ensure that the system has zero linear and angular momentum. After assigning the initial velocities, the nanobeam is evolved subject to NPT conditions with the pressure set to zero and the temperature set to θ_0. A coupled Nosé-Hoover chain thermostat (chain length = 3) and barostat as described in Shinoda et al. [125] were used. This method combines the hydrostatic equations of Tobias et al. [126] with the strain energy proposed by Parrinello and Rahman [127]. The method is implemented within the LAMMPS code. The damping times defined by LAMMPS for the thermostat and barostat were taken to be 100 fs and 400 fs, respectively. The system is evolved for a total of 3×10^6 MD steps with a time step size $\Delta t_{\mathrm{MD}} = 2$ fs. The lattice constant at the target temperature θ_0 is determined by computing the average volume $\bar{V}$ over the final 10^4 MD steps, then $a = [\bar{V}/(n_x n_y n_z)]^{1/3}$. The averaging is necessary because under NPT conditions the volume fluctuates about the mean value. Lattice constants at different temperatures obtained using this procedure are presented in Table 4.1.

Table 4.1: Lattice constants a (Å) at different temperatures θ_0 (K).

θ_0	a	θ_0	a	θ_0	a	θ_0	a	θ_0	a
5	5.262	10	5.267	15	5.278	20	5.284	25	5.291
30	5.312	40	5.338	50	5.364	60	5.394	70	5.430

4.2 Green-Kubo method

Following the equilibration procedure of the previous section, an NVT simulation is performed for 2×10^6 MD steps followed by an NVE simulation for 6×10^6 MD steps, with a time step size of $\Delta t_{\text{MD}} = 1$ fs. The lack of a thermostat means that the system temperature will oscillate about the target temperature, however, this approach ensures that perturbations caused by thermostats do not affect the computation of the heat current autocorrelation function. The NVE data is divided into six groups each corresponding to 1 ns of simulation time. The thermal conductivity tensor for each group, as a function of the integration time τ_I is computed using Eq. (3.59) with the first 5×10^5 steps excluded. The statistical error is estimated using the approach described in Ref. [40]. The thermal conductivity k of the system is taken to be the average of the diagonal components of the ensemble average of the tensor. This value oscillates about a plateau within a range of τ_I (see Fig. 4.1). Finally, a mean of all thermal conductivities computed within this range along with the maximum standard error is reported. (See the tabulated results presented below.)

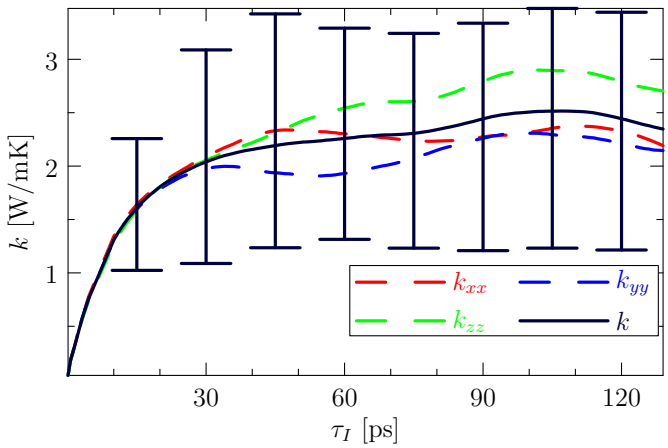

Figure 4.1: Thermal conductivity tensor diagonal components and their average, k, as a function of the integration time τ_I for a beam of size $33 \times 4 \times 4$ unit cells at $\theta_0 = 15$ K subject to periodic BCs. Within the range 50 ps $\leq \tau_I \leq$ 100 ps, k oscillates around a plateau.

4.3 Direct method

In the direct method, a temperature gradient is imposed along the length of the beam by thermostatting certain regions of the beam. The beam is partitioned into bins by the method described in the Section 3.1.9. As a typical example, consider a beam of size $123 \times 4 \times 4$ unit cells with $\theta_L = \theta_R = 12.5$ K and $\theta_M = 17.5$ K. The beam is divided into $N_{bins} = 41$ bins with each bin consisting of 192 atoms. The bins at the two ends and in the middle are thermostatted by Langevin dynamics [122]. The initial lattice parameter is taken to be the average of values computed for the end bins and middle bin temperatures (see Table 4.1). Figure 4.2 presents the temperature and heat current profiles at steady state for different damping times used in the Langevin dynamics. The damping time t_{damp} is akin to a relaxation time which is normally inversely proportional to the viscosity of the medium. A damping time with a value of 1.0 means that during the thermostatting process, temperature is relaxed over a time span of roughly 1 ps.

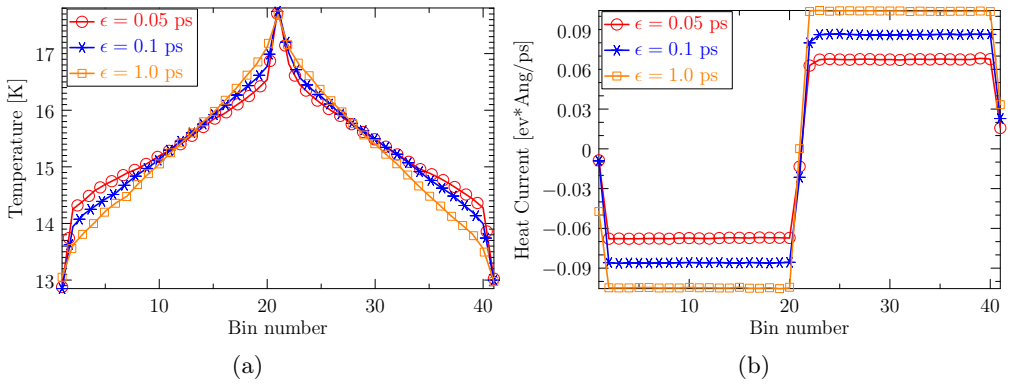

Figure 4.2: Profiles of steady-state (a) temperature and (b) heat current along the length of the beam for different damping times under periodic BCs for an argon beam of size $123 \times 4 \times 4$ unit cells.

From Fig. 4.2(a) it is clear that the temperature profiles are piecewise linear with discontinuous jumps between thermostatted and adjacent unthermostatted bins. These jumps are due to the Kapitza effect discussed in the introduction. Standard errors in thermal conductivity are calculated using the method of Zhou et al. [116]. Details are given below.

Following the application of thermostats, steady state conditions are typically achieved

after about 10^6 MD steps with a step size of $\Delta t_{\mathrm{MD}} = 2$ fs. We run each simulation for a total time of 6×10^6 MD steps, and discard the initial 10^6 time steps, which is equivalent to 2 ns. The remaining simulation time is uniformly divided into $\mathcal{N}$ blocks. For example, if we take $\mathcal{N} = 10$, each block corresponds to 5×10^5 MD steps, which is equivalent to 1000 ps of data. The heat flux and temperature are averaged for each bin during this time block. The temperature gradient is calculated by fitting a straight line over the steady state temperature profile of all bins except the thermostatted bins and the adjacent two bins to the thermostats. So the temperature of bin n in time block j is given by

$$\langle \theta_n \rangle_j = \langle \theta_{n=4} \rangle_j + \left\langle \frac{\Delta\theta}{\Delta x} \right\rangle_j (n-4), \tag{4.1}$$

where $n \in [4, N_{\mathrm{bins}} - 3]$ and $j \in [1, \mathcal{N}]$. The corresponding thermal conductivities, k_j, are given by

$$k_j = \langle \langle q \rangle \rangle_j \left\langle \frac{\Delta\theta}{\Delta x} \right\rangle_j^{-1}. \tag{4.2}$$

The standard deviations of the thermal conductivities, σ_n^s, are first calculated with respect to $\mathcal{N}$ blocks by

$$\sigma^s = \sqrt{\frac{\sum_{j=1}^{\mathcal{N}} (k_j - \langle k \rangle)^2}{\mathcal{N} - 1}}, \tag{4.3}$$

where

$$\langle k \rangle = \frac{\sum_{j=1}^{\mathcal{N}} k_j}{\mathcal{N}}. \tag{4.4}$$

To calculate the standard deviations over long runs the following formula is used:

$$\sigma_n = \frac{\sigma_n^s}{\sqrt{\mathcal{N}}}. \tag{4.5}$$

4.4 Thermal parameter identification method

We illustrate the TPI method for a beam of size $153 \times 4 \times 4$ unit cells. The initialization stage is first performed as outlined in Section 4.1 to bring the beam to steady state at the target temperature of $\theta_0 \approx 15$ K. Then binning is performed with a total number

of $N_{\text{bins}} = 51$ bins such that each bin contains 192 atoms (see Section 3.1.9). Next the sinusoidal temperature distribution in Eq. (3.67) is applied by setting the temperature of n-th bin to

$$\theta_n = \theta_0 + \Delta\theta_0 \cos(2\pi n/N_{\text{bins}}), \quad 1 \leq n \leq N_{\text{bins}}, \tag{4.6}$$

where $\Delta\theta_0 = 0.1\theta_0$, using a Langevin thermostat with a damping time of 1 ps. Thus N_{bins} thermostats with same damping time (but different temperatures) are employed. The system is run for 2×10^6 MD steps with a time step of $\Delta t_{\text{MD}} = 2$ fs. Having attained the sinusoidal temperature distribution, the system is run for another 5×10^5 MD steps, during which the positions and momenta of all atoms are stored at intervals of 10^4 MD steps. Thus 50 independent realizations satisfying the initial conditions described by Eq. (4.6) are obtained for further relaxation of the system. For each realization, the thermostats are switched off and the system is left to evolve under *NVE* conditions for another 56×10^4 MD steps with a time step of $\Delta t_{\text{MD}} = 1$ fs. The temperature and x-component of the heat flux current for each bin, θ_n and J_{xn}, are recorded, using Eqs. (3.54) and (3.60), and averaged over $\Delta_t = 1.4$ ps using Eq. (3.55). Thus $N_{\text{profiles}} = 400$ temperature and heat current profiles are collected. We vary Δ_t for different lengths so that before reaching the steady-state we collect enough profiles to analyze the nonsteady relaxation behavior of the system. Thermal fluctuations are further reduced by averaging over multiple realizations. Averaging over all 50 realizations, the temperature and heat current profiles are shown in Fig. 4.3. Next, we calculate $\bar{\theta}(t)$ and $\bar{q}(t)$ using Eqs. (3.81) and (3.83) for these profiles,[3] and perform the nonlinear least square fitting of functions $\bar{\theta}/\Delta\theta_0$ and $\bar{q}(t)/\pi\Delta\theta_0$ as defined in Eqs. (3.88) and (3.93), respectively. The plots of these functions are shown in Fig. 4.4. The expression of $\bar{\theta}(t)/\Delta\theta_0$ in Eq. (3.82) is same for both the CV and the Jeffreys-type model, and these models successfully capture the NEMD data. However, we note that the NEMD data includes a short wave length oscillation with a periodicity of about 50 ps. In order to investigate the origin of this oscillation, we calculate the cosine average of the stress

[3] We have explored the effect of the number of profiles used in computing Eqs. (3.81) and (3.83). We found that increasing the number of bins had only a small effect (less than the standard errors) on the final values of the parameters.

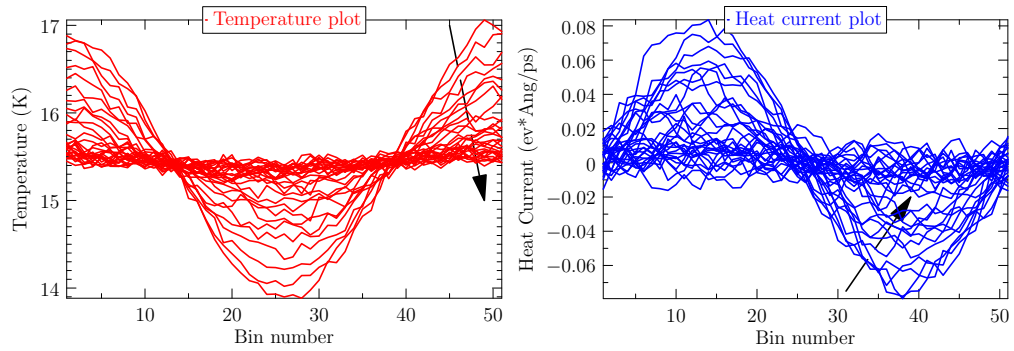

Figure 4.3: Temperature and heat current profiles for an argon beam of size $153 \times 4 \times 4$ unit cells with the base temperature $\theta_0 \approx 15$ K and the amplitude of sinusoidal perturbation $\Delta\theta_0 \approx 1.5$ K. Each profile is an average of 14 ps of data. The black arrows show the direction of time.

component σ_{xx} over length of the beam:

$$\bar{\sigma}_{xx}(t) = \frac{2}{L}\int_0^L \sigma_{xx}(x,t)\cos(2\pi x/L)dx. \tag{4.7}$$

The plot of $\bar{\sigma}_{xx}(t)$ with respect to time t and its periodogram power spectral density (PSD) are shown in Fig. 4.5. The PSD has a dominant spike at a frequency of 0.018 ps^{-1}, which suggests that the system has a stress wave of period 55.14 ps. This is very close to the oscillation period present in the $\bar{\theta}(t)/\Delta\theta_0$ plot. Moreover, the longitudinal speed of sound in solid argon at 15 K is around [128] 1600 m/s, thus a stress wave at this speed will travel the length of the nanobeam in about 50.5 ps. This time is also very close to the oscillation period. Hence we conclude that the system develops a very low stress wave, of the order of a few bars in magnitude, that affects $\bar{\theta}(t)/\Delta\theta_0$ through thermomechanical coupling and leads to the observed oscillations.

We also tried fitting the NEMD $\bar{\theta}(t)/\Delta\theta_0$ data with the Fourier model given in Eq. (3.85). The results in Fig. 4.4(a) may suggest that the Fourier model adequately captures the NEMD data. However, it is clear in Fig. 4.4(b) that the exponentially increasing part of the $\bar{q}(t)/\pi\Delta\theta_0$ curve (near $t = 0$) cannot be captured by the exponentially decaying expression for the Fourier model in Eq. (3.86). In contrast, the expression for the Jeffreys-type model given in Eq. (3.84) provides a good fit to the NEMD data.

The volumetric heat capacity γ appearing in Eqs. (3.89) and (3.90) is computed in

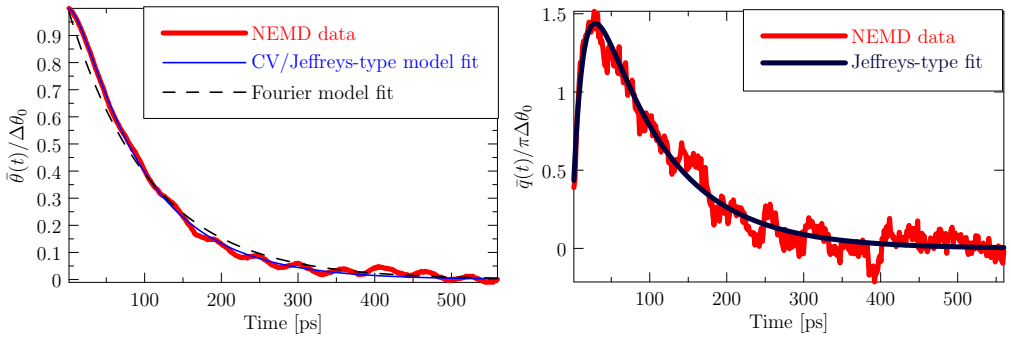

Figure 4.4: (a) Plot of $\bar{\theta}(t)/\Delta\theta_0$ with respect to time t for the beam under study. The red, blue and black lines correspond to NEMD data, CV/Jeffreys-type model and Fourier model, respectively. (b) Plot of $\bar{q}(t)/\pi\Delta\theta_0$ with respect to time t. The red and dark blue lines correspond to NEMD data and Jeffreys-type model, respectively.

a separate calculation. The entire beam is brought to steady state at $\theta = 15$ K with a Langevin thermostat for 2×10^6 MD steps with a time step size $\Delta t_{\text{MD}} = 2$ fs. The beam continues to be thermostatted for another 3×10^5 MD steps and the energy of the beam is recorded at each MD step. Then γ is related to the average energy fluctuations through the following relation [90]:

$$k_{\text{B}}\theta^2\gamma V = \left\langle E^2 \right\rangle - \left\langle E \right\rangle^2, \tag{4.8}$$

where k_{B} is Boltzmann's constant. Using Eq. (4.8), we obtain $\gamma = 7.14 \pm 0.04 \times 10^{-6}$ eV/(Å^3 K). We find that γ does not change significantly with system size. Substituting γ into Eqs. (3.89) and (3.90), the following results are obtained for the CV parameters of argon, $k^{\text{CV}} = 1.72$ W/mK and $\tau_q^{\text{CV}} = 12.11$ ps, and the Jeffreys parameters for argon, $k = 1.75$ W/mK, $\tau_q = 12.33$ ps, and $\tau_\theta = 1.94$ ps. In order to calculate standard errors in these parameters, we partition all 50 realizations into 4 sets and perform the nonlinear least square fitting over each set separately.

Table 4.2 presents the values of the thermal conductivity for different temperatures and beam lengths under periodic BCs obtained by the Green-Kubo and NEMD direct methods. Tables 4.3-4.5 present the thermal parameters for the Fourier, CV and Jeffreys-type models obtained using the TPI method. We see that the thermal conductivities obtained for all three models are nearly the same, but the relaxation times vary.

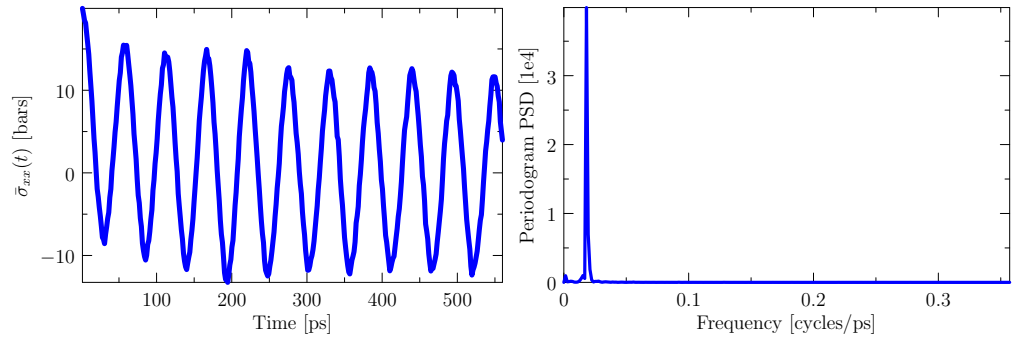

Figure 4.5: (a) $\bar{\sigma}_{xx}(t)$ vs time t, (b) Periodogram power spectral density estimate of the signal $\bar{\sigma_{xx}}(t)$ about its mean value.

A striking result is that at a given temperature, the thermal parameters obtained using the direct and TPI methods are length (size) dependent. After a critical length [117], the dependence of thermal conductivity k on length L takes the following form [40, 52, 117]:

$$\frac{1}{k} = \frac{1}{k_\infty} + \frac{c}{L}, \tag{4.9}$$

where c is a constant dependent on the method of calculation, and k_∞ is the bulk value. Fig. 4.6(a) presents a plot of $1/k$ versus $1/L$ at $\theta_0 = 15$ K for three different methods: (i) Green-Kubo method, (ii) direct method, (iii) TPI method for the Jeffreys-type model. Fitting the data in this plot to the relation in Eq. (4.9), yields k_∞ values for the three methods which are in good agreement: 2.32 ± 0.10, 2.39 ± 0.06, 2.57 ± 0.14 W/mK. The uncertainty reported for the bulk thermal conductivity for each method is taken as the maximum over the standard errors of the length-dependent thermal conductivities computed using that method, i.e. it is the L^∞-norm. Not shown in Fig. 4.6(a), the TPI results for the Fourier and CV models give k_∞ values that are very close to that of the TPI method for the Jeffreys-type model. The temperature dependence of the bulk thermal conductivity obtained using these three methods is shown in Fig. 4.7. The computed values are in good agreement with each other and with the MD simulation results of Kaburaki et al. [129].

Non-Fourier relaxation times also exhibit a length dependence as shown in Fig. 4.6(b). This effect can be understood by considering the contributions to the relaxation time

Table 4.2: Thermal conductivity k in W/mK obtained using the Green-Kubo and direct method for different beam lengths L in unit cells and different temperature. Values in parentheses are the standard errors of the thermal conductivities.

Green-Kubo method under periodic BCs					
	Temp (K)				
L	15	25	35	45	55
33	2.34 (1.10)	1.06 (0.52)	0.72 (0.20)	0.51 (0.31)	0.35 (0.09)
63	2.67 (2.48)	1.14 (0.44)	0.74 (0.20)	0.47 (0.20)	0.36 (0.17)
93	2.58 (1.24)	1.10 (0.61)	0.73 (0.29)	0.47 (0.18)	0.35 (0.19)
153	2.89 (1.85)	1.07 (0.21)	0.81 (0.26)	0.46 (0.13)	0.36 (0.10)
303	2.28 (1.69)	1.08 (0.79)	0.70 (0.23)	0.51 (0.40)	0.34 (0.11)
603	2.52 (1.91)	1.09 (0.65)	0.74 (0.25)	0.51 (0.31)	0.35i (0.15)
Direct method under periodic BCs					
	Temp (K)				
L	15	25	35	45	55
33	1.82 (0.06)	0.73 (0.02)	0.61 (0.04)	0.40 (0.01)	0.32 (0.02)
63	2.06 (0.02)	1.05 (0.04)	0.65 (0.01)	0.49 (0.03)	0.34 (0.04)
93	2.16 (0.02)	1.12 (0.01)	0.68 (0.03)	0.50 (0.01)	0.37 (0.04)
153	2.22 (0.03)	1.11 (0.03)	0.68 (0.03)	0.50 (0.02)	0.41 (0.03)
303	2.33 (0.04)	1.18 (0.01)	0.69 (0.02)	0.50 (0.02)	0.39 (0.04)
603	2.34 (0.06)	1.13 (0.03)	0.70 (0.03)	0.50 (0.02)	0.40 (0.04)

due to normal and Umklapp processes of intrinsic phonon-phonon scattering phenomena [66], and applying the Matthiesen rule which assumes that all scattering mechanisms are independent. This leads to a linear relationship between $1/\tau$ and $1/L$ (where τ is either τ_q or τ_θ) similar to that obtained for thermal conductivity [117, 130]:

$$\frac{1}{\tau} = \frac{1}{\tau_\infty} + \frac{c_\tau}{L}. \tag{4.10}$$

Here c_τ is a constant dependent on the model. Fitting to the data presented in Fig. 4.6(b), we find at $\theta_0 = 15$ K that the bulk values τ_∞ for the Jeffreys-type relaxation times τ_q and τ_θ are 120.36 ± 7.35 ps and 6.88 ± 4.21 ps, respectively, and the bulk value for τ_q in the CV model is 96.65 ± 10.92 ps. Again, the bulk value uncertainty is taken to be the L^∞-norm (maximum) of the standard errors in the length-dependent data.

Table 4.3: The Fourier thermal conductivity k in units of W/mK at different temperatures obtained using the TPI method by nonlinear fitting of the expression for $\bar{\theta}(t)/\Delta\theta_0$ in Eq. (3.85). Values in parentheses are the standard errors of the parameters.

	Fourier thermal conductivity			
	Temp (K)			
Length	15	25	35	45
33	0.75 (0.06)	0.46 (0.02)	0.36 (0.05)	0.29 (0.02)
63	0.99 (0.07)	0.65 (0.03)	0.48 (0.03)	0.36 (0.07)
93	1.19 (0.03)	0.83 (0.07)	0.50 (0.01)	0.38 (0.02)
153	1.71 (0.08)	0.87 (0.04)	0.56 (0.02)	0.44 (0.04)
303	2.09 (0.09)	1.06 (0.05)	0.60 (0.01)	0.47 (0.03)
603	2.32 (0.03)	1.24 (0.03)	0.75 (0.03)	0.51 (0.02)

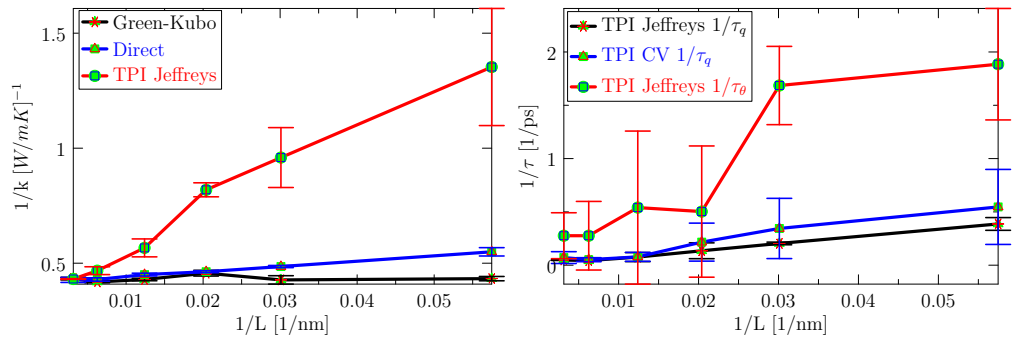

(a) (b)

Figure 4.6: Plots at $\theta_0 = 15$ K of (a) $1/k$ versus $1/L$ for the Green-Kubo method, direct method, and the TPI method with the Jeffreys-type model, (b) $1/\tau$ vs $1/L$ for the TPI method with CV and Jeffreys-type models.

4.5 Heat waves

In this section, we study the propagation of heat pulses as originally done by Tsai and MacDonald [41]. The introduction of a heat pulse generates several waves that propagate at different speeds corresponding to different phonon modes, second sound waves, and diffusive components [41, 43, 131]. An argon beam of size $303 \times 4 \times 4$ is divided into 101 bins, where each bin consists of 243 atoms. Periodic BCs are employed. The beam temperature is initially set to 0 K. The middle bin is then subjected to a heat pulse while the rest of the beam evolves under *NVE* conditions. The heat pulse is introduced

Table 4.4: The CV model parameters at different temperatures obtained using the TPI method by nonlinear fitting of the expression for $\bar{\theta}(t)/\Delta\theta_0$ in Eq. (3.82). For each length, the two rows are the values of thermal conductivity k^{CV} in W/mK and the relaxation time τ_q^{CV} in ps. Values in parentheses are the standard errors of the parameters.

	CV parameters			
	Temp (K)			
Length	15	25	35	45
	0.75 (0.15)	0.47 (0.02)	0.37 (0.04)	0.29 (0.02)
33	1.83 (1.18)	0.63 (0.84)	2.00 (2.59)	2.43 (2.24)
	1.00 (0.09)	0.65 (0.03)	0.48 (0.03)	0.36 (0.07)
63	2.90 (2.38)	1.21 (1.42)	4.07 (4.43)	3.56 (3.71)
	1.20 (0.03)	0.83 (0.07)	0.50 (0.01)	0.38 (0.02)
93	4.62 (3.81)	5.58 (2.06)	6.35 (2.35)	3.29 (2.87)
	1.73 (0.09)	0.89 (0.01)	0.56 (0.02)	0.44 (0.04)
153	12.79 (6.81)	9.02 (8.31)	7.41 (6.08)	17.69 (8.49)
	2.09 (0.10)	1.06 (0.05)	0.60 (0.01)	0.47 (0.04)
303	19.40 (7.09)	11.26 (8.88)	39.23 (11.01)	12.45 (8.91)
	2.33 (0.03)	1.24 (0.04)	0.78 (0.03)	0.51 (0.03)
603	14.03 (10.92)	13.03 (8.01)	10.45 (8.11)	14.51 (8.51)

by rescaling the temperature of the middle bin at each MD time step ($\Delta t_{\mathrm{MD}} = 2$ fs). For the first 100 MD steps the temperature is linearly increased from 0 K to 20 K. It is then maintained at 20 K for another 500 MD steps and then linearly decreased from 20 K to 0 K over 100 MD steps. The temperature rescaling is done by adjusting the momenta of all the atoms in the middle bin by

$$\tilde{\boldsymbol{p}}_i(t+\Delta_t) = \tilde{\boldsymbol{p}}_i(t)\sqrt{\frac{\theta_0}{\theta(t)}}, \tag{4.11}$$

where θ_0 is the target temperature, $\theta(t)$ is the instantaneous temperature, and $\tilde{\boldsymbol{p}}(t)$ is the adjusted momentum after removing the total linear and angular momentum of the middle bin. This is equivalent to adding or subtracting an energy $\Delta E = \Delta E_{\mathrm{kin}}$ to the middle bin:

$$\Delta E_{\mathrm{kin}} = \sum_{i=1}^{N} \frac{1}{2m_i}\left(\tilde{\boldsymbol{p}}_i^2(t+\Delta t) - \tilde{\boldsymbol{p}}_i^2(t)\right), \tag{4.12}$$

where N is the total number of atoms in the middle bin and m_i is the mass of the i-th atom.

Table 4.5: Parameters at different temperatures obtained with the TPI method by nonlinear fitting of the expression for $\bar{\theta}(t)/\Delta\theta_0$ in Eq. (3.82) and $\bar{q}(t;\tau_q)/\pi\Delta\theta_0$ in Eq. (3.91). The first column is the beam length in unit cells. For each length, the three rows are the values of thermal conductivity k in W/mK and the two time lags τ_θ and τ_q in ps. Values in parentheses are the standard errors of the parameters.

	Jeffreys-type parameters			
	Temp (K)			
Length	15	25	35	45
	0.74 (0.14)	0.49 (0.09)	0.36 (0.06)	0.33 (0.03)
33	0.53 (0.45)	0.15 (0.10)	1.55 (1.15)	1.93 (2.13)
	2.59 (0.40)	1.90 (1.23)	5.27 (0.05)	4.69 (2.15)
	1.04 (0.14)	0.70 (0.08)	0.48 (0.03)	0.35 (0.03)
63	0.59 (0.13)	1.49 (1.23)	0.66 (0.58)	4.84 (3.45)
	4.90 (0.30)	3.81 (2.41)	2.76 (1.35)	4.98 (4.39)
	1.22 (0.05)	0.86 (0.08)	0.52 (0.02)	0.40 (0.03)
93	1.99 (2.43)	2.09 (1.90)	4.06 (3.58)	2.43 (2.16)
	7.40 (4.06)	5.79 (2.21)	6.33 (4.36)	5.71 (1.90)
	1.77 (0.12)	0.92 (0.01)	0.59 (0.03)	0.46 (0.06)
153	1.85 (2.46)	6.22 (3.81)	9.40 (4.56)	19.54 (11.54)
	13.15 (7.35)	13.67 (6.45)	12.85 (3.28)	22.79 (5.08)
	2.14 (0.08)	1.08 (0.07)	0.63 (0.01)	0.48 (0.06)
303	3.62 (4.21)	9.11 (4.48)	39.69 (5.09)	21.45 (12.21)
	23.17 (1.14)	16.38 (4.07)	40.73 (11.55)	25.87 (6.81)
	2.32 (0.01)	1.25 (0.05)	0.78 (0.03)	0.51 (0.03)
603	3.62 (2.82)	12.88 (6.79)	12.42 (4.23)	23.55 (11.89)
	20.34 (1.90)	20.45 (5.90)	20.81 (4.28)	26.56 (5.11)

Following the application of the heat pulse, the system is left to evolve under *NVE* conditions for 3×10^4 MD steps with a step size of $\Delta t_{\mathrm{MD}} = 2$ fs. The simulation is repeated six times with different initial velocities drawn from a Maxwell-Boltzmann distribution for the initial temperature. Figure 4.8 shows a plot of the temperature along the length of the beam as function of time following the heat pulse. The temperature data are an average of 100 MD time steps and six ensembles corresponding to different initial velocities.

The presence of waves is clear in Fig. 4.8, where L indicates the longitudinal stress wave, and there are five distinct heat waves ranging from H_1 and H_5. Stress and heat

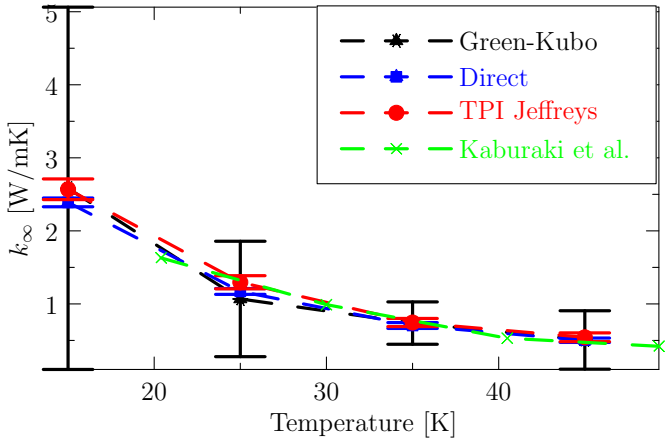

Figure 4.7: Bulk thermal conductivity versus temperature obtained by fitting Eq. (4.9) using data from the Green-Kubo method, direct method, and the TPI method with the Jeffreys-type model.

waves are distinguished by comparing the longitudinal x and transverse y and z components of temperature; heat waves have nearly the same longitudinal and transverse components whereas for stress waves these components differ. Since the disturbances propagate in straight lines, we can calculate their speeds. The calculated speed of the stress-wave L is 1608 m/s and the calculated average speed of the heat waves from H_1 to H_5 is approximately 630 m/s. Feldman and Klein [132] report the longitudinal speed of sound c_l for solid argon at 0 K, computed using a LJ potential, as

$$\rho c_l^2 \approx 49\,\text{kbar} = 4.9\,\text{GPa}, \tag{4.13}$$

where ρ is the mass density of crystal. The density in our case is $\rho = 2307.225$ kg/m^3. Then from Eq. (4.13), we have $c_l \approx 1457$ m/s, which is in reasonable agreement (within 9.4%) of the longitudinal stress-wave computed from Fig. 4.8, thus confirming the validity of the calculation. Theoretically, the average speed of heat waves is [41] $c_{\text{av}}/\sqrt{3}$, where c_{av} is the average speed of sound appropriate to a Debye solid. Taking [41] $c_{\text{av}} = 0.731 c_l$, the theoretical average speed of the heat wave is $c_{\text{av}}/\sqrt{3} \approx 678$ m/s, which is comparable to the calculated average speed found above. Thus the existence of second sound in solid argon is confirmed.

It is of interest to see whether the Jeffreys-type model with parameters obtained using TPI is able to describe the heat pulse problem discussed above. This would validate

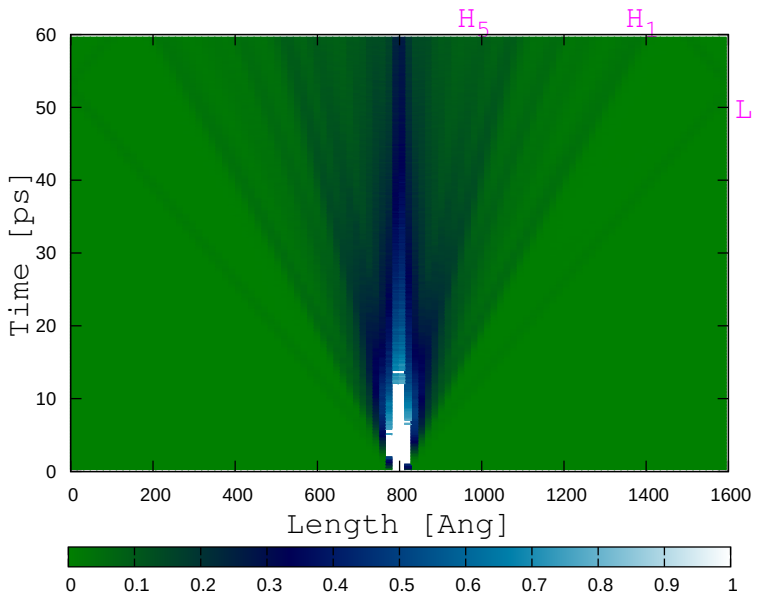

Figure 4.8: A plot of the temperature along the length of the beam as a function of time showing the following modes: L and H_1 to H_5. The displayed temperatures are limited to a range of 0 to 1 K to make the presence of the waves more clear. (Any temperature larger than 1 K appears white.)

the TPI approach and demonstrate that the Jeffreys-type model provides an adequate description for the thermal response of solid argon and is transferable to different thermal problems. Using the TPI approach we obtain the thermal parameters for a beam (of the same size as the heat pulse beam) with periodic BCs and $\theta_0 = 2.5$ K. Taking an experimental value [133] for γ at 2.5 K, the estimated parameter values are $k = 0.013 \pm 0.001$ W/mK, $\tau_\theta = 6.21 \pm 1.03$ ps, and $\tau_q = 15.57 \pm 3.47$ ps. The heat wave speed predicted by the Jeffreys-type model is $c = \sqrt{k/(\gamma\tau_q)} = 596.62 \pm 70.72$ m/s. This value is comparable to the speeds calculated above from the heat pulse simulation. Figure 4.9 compares NEMD temperature profiles with the numerical solution of the Jeffreys-type model. We see that the Jeffreys-type model with parameters obtained using the TPI method successfully describes the propagation of heat waves associated with the spreading of a thermal pulse. A similar analysis using a Fourier model (not shown) was not able to capture the sharp peaks of the temperature profiles.

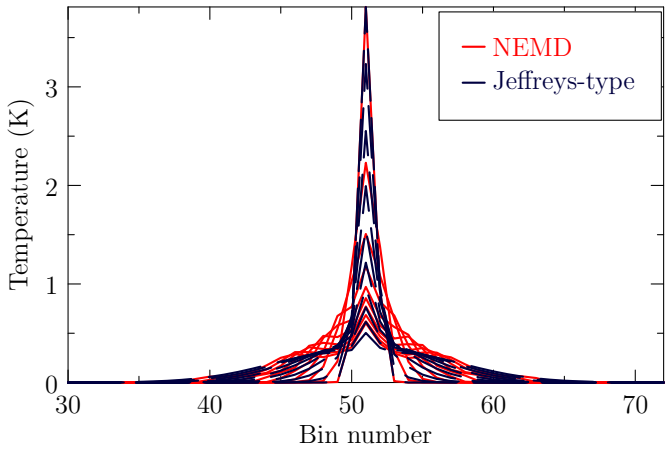

Figure 4.9: Comparison between NEMD data and the Jeffreys-type continuum model with thermal parameters computed using the TPI method. Each NEMD temperature profile is an average of 2 ps of NEMD data.

4.6 Summary

A new simple TPI method has been proposed for extracting the thermal non-Fourier (Jeffreys-type) parameters k, τ_θ and τ_q from a sequence of NEMD temperature and heat-flux profiles. An initial sinusoidal temperature distribution is applied using thermostats to a nanobeam. The thermostat are then removed, and the nanobeam temperature decays to a constant average value under constant energy conditions. The thermal parameters are obtained by fitting analytical solutions for scalars obtained as cosine and sine-averages of the temperature and heat flux, respectively, to the NEMD data during the decay process. (Implementations of the TPI approach in MATLAB are available in the supplementary online material.)

The TPI method was applied to argon nanobeams of various sizes at different temperatures. The values of the thermal conductivity k were found to be in good agreement with those computed using the Green-Kubo and direct NEMD methods. In addition, the TPI method provides the relaxation times τ_q and τ_θ, which cannot be obtained using the other methods. The TPI approach also has the advantage that no thermostats are used during the calculation of the thermal parameters. It is therefore unaffected by issues, such as the Kapitza effect, that corrupt direct method results.

It was found that a Jeffreys-type model with three parameters was better able to reproduce NEMD temperature profiles in thermal problems than a simple Fourier model. This was demonstrated by performing an NEMD simulation of the spreading of a heat pulse applied to the center of a nanobeam. The heat propagates out in waves, confirming the existence of second sound in argon. A Jeffreys-type model with parameters obtained using the TPI approach predicts heat wave speeds in agreement with the NEMD simulations and reproduces the temperature profiles to good accuracy.

Chapter 5

Kapitza effect

In experimental and computational studies of heat transfer, thermal boundary conditions (BCs) must be applied to the system. For example, in an experiment, a constant temperature BC can be applied by exposing a portion of the body to a large heat bath which maintains a constant temperature. This is demonstrated schematically in Fig. 5.1(a), where the left end ABC of a long solid beam $OABCO'$ is exposed to a hot fluid at temperature θ_{L} that serves as the heat bath. The insulator LL' prevents contact between the hot fluid and the rest of the beam. Heat is transferred from the fluid to the solid beam through the surfaces A, B and C, and from there it can flow along the length of the beam. This setup ensures that a temperature close to θ_{L} is maintained at cross-section D.

In a nonequilibrium molecular dynamics (NEMD) study of heat transfer, the experimental setup in Fig. 5.1(a) is typically modeled by applying a numerical thermostat, such as Langevin or Nosé-Hoover, to the region ABC shown shaded in Fig. 5.1(b). Such thermostats maintain the average temperature at a desired level while correctly reproducing the fluctuations expected from equilibrium statistical mechanics (see for example Ref. [84]). Unfortunately, it is well-known that applying thermostats in this manner leads to artificial discontinuous jumps in the temperature between the thermostatted and unthermostatted regions (interface D in Fig. 5.1(b)), which depend on the system size and thermostat parameters [46].

Temperature jumps across *real* material interfaces were first observed by Kapitza [134] in 1941 in experimental studies of the superfluidity of helium II. Kapitza measured the

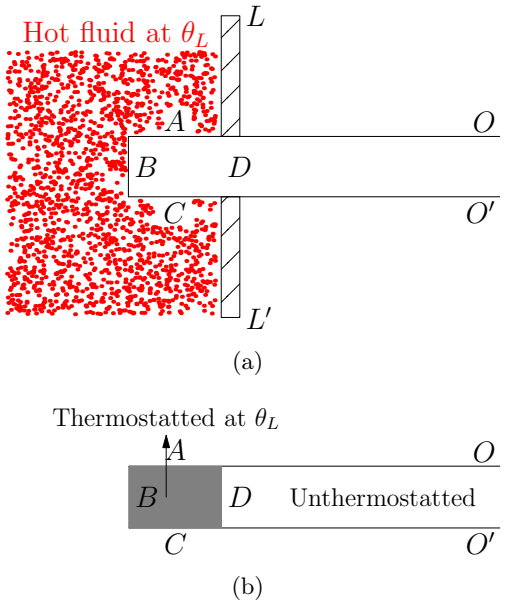

Figure 5.1: (a) Physical system: The left end ABC of a solid beam $OABCO'$ is immersed in the hot fluid at temperature θ_{L}, which is separated from the rest of the beam by an insulator LL'. (b) An NEMD model where the region to the left of D is thermostatted (shown dark gray).

distribution of temperature in the neighborhood of a heated metal surface freely suspended in helium II. He observed temperature discontinuities across the metal–helium II interface with a corresponding thermal flux [135]. This behavior suggested the existence of an interfacial thermal resistance R_{k}, which is now known as *Kapitza resistance* [136]. This term was originally reserved for solid–liquid helium II interfaces, but has since been generalized to thermal boundary resistance for arbitrary solid–solid and solid–liquid interfaces.

Different theories have been proposed to explain Kapitza resistance, most notably the Khalatnikov model, which is based on acoustic mismatch theory [135, 136, 137]. The basic idea is that due to the change in acoustic properties at the interface, some phonons will reflect there reducing the total thermal transport. The interface thus acts as a thermal barrier, which can support a temperature jump [138]. Referring back to the physical system in Fig. 5.1(a), we may expect to observe Kapitza resistance at the interfaces A, B and C between the beam and the fluid, however not across D which

is an internal interface in the beam. In contrast, as noted above, Kapitza resistance *does* exist across D in the NEMD system (Fig. 5.1(b)). The reason for this is that the thermostat interferes with the dynamics of region ABC and thus effectively changes the material properties which in turn leads to (an artificial) Kapitza resistance. Specifically, the thermostat reduces correlation effects between atoms and consequently reduces the heat flux. This poses a problem when NEMD simulations are used to compute physical properties, such as thermal conductivity, that are affected by the presence of artificial Kapitza resistance. We contrast this with NEMD simulations that are designed to measure actual Kapitza resistance at physical material interfaces (see for example Refs. [139, 140, 141, 142]).

A standard approach for computing the thermal conductivity k of a material is the NEMD "direct method" [40, 116, 143] described in Section 3.2.2 and Section 4.3. A common solution to dealing with artificial Kapitza resistance in NEMD simulations is to compute the thermal conductivity from the slope of a linear function fit to the temperature profile away from the thermostatted regions [40]. The objective in such simulations is to obtain bulk thermal conductivity. In order to remove finite size effects, a series of simulations is carried out of increasing system size and the results are extrapolated to infinity. This convergence can be slow and therefore requires simulations of very large systems that is computationally very expensive. In this chapter, we take a different approach, and introduce a phenomenological model that explicitly includes the effect of the numerical thermostat and associated Kapitza resistance. This makes it possible to obtain the bulk thermal conductivity to a desired level of accuracy without having to go to very large system sizes. Instead a set of simulations is performed in which both the system size and thermostat parameters are varied. This significantly reduces the computational cost of the calculations. In addition, including the thermostat in the model may make it possible in future work to design the thermostat to mimic real physical boundary conditions as opposed to being a numerical artifact that must be removed.

5.1 Kapitza effects in thermal conductivity measurements

Figure 4.2 shows the temperature and heat current (heat flux times bin volume) profiles at steady state for different values of the Langevin thermostat damping time ϵ. The

abrupt changes in temperature at the interface between the thermostatted and unthermostatted bins due to the Kapitza effect are clear in Fig. 4.2(a). It is important to point out that the change in temperature across the interface is not a discontinuous jump, but involves a nonlinear variation on the scale of the phonon mean free path. In argon this is about [144] 4.8 nm, which is on the same scale as the 1.6 nm bin size in the simulations. As a result most of the nonlinearity is smoothed out by bin averaging. Irrespective of this nonlinearity, a discontinuous jump in temperature can be defined by fitting a straight line to the temperature profile away from the thermostat and extrapolating to the end [49]. The magnitude of this jump is reduced by increasing ϵ, or by increasing the length of the simulated beam. The former is understandable since increasing the damping time reduces the effect of the thermostat on the dynamics of the system. However, increasing the damping time also reduces the ability of the thermostat to maintain the target temperature; thus a trade-off is involved. The reason that increasing the beam length reduces the Kapitza effect is that the jump in temperature is proportional to the temperature gradient [49] and the gradient is decreased by increasing the length. Both effects are captured by the phenomenological model described below.

5.1.1 Phenomenological model

As discussed in Section 3.2.2 and Section 4.3, the left and right ends of the nanobeam are thermostatted at the same temperature ($\theta_{\mathrm{L}} = \theta_{\mathrm{R}}$), and the middle bin is maintained at a temperature θ_{M}. Under conditions where the difference between θ_{L} and θ_{M} is small, the thermal conductivity k can be assumed to be constant, and the heat equation for steady-state conditions leads to the following relation:

$$\frac{\partial^2 \theta}{\partial x^2} = 0, \quad x \in [0, L_m]. \tag{5.1}$$

Here $x = 0$ and $x = L_m$ correspond to the centers of the first and middle bins. Solving for θ, we obtain a linear temperature profile for the left half of the beam,

$$\theta(x) = a_1 x + a_2, \tag{5.2}$$

where a_1 and a_2 are constants. (The right half of the beam has a similar relation.) Due to the Kapitza effect, the linear temperature profile in Eq. (5.2) associated with the bins

away from the thermostats does not agree with the temperatures set by the thermostats when the profile is extended to the thermostatted bins, i.e.

$$\theta(0) \neq \theta_{\mathrm{L}}, \quad \theta(L_m) \neq \theta_{\mathrm{M}}. \tag{5.3}$$

Instead, we represent the interaction of the nanobeam with the thermostatted bins through *convection* BCs:

$$-k\theta_{,x}(0) = h[\theta_{\mathrm{L}} - \theta(0)], \tag{5.4}$$

$$-k\theta_{,x}(L_m) = h[\theta(L_m) - \theta_{\mathrm{M}}], \tag{5.5}$$

where $\square_{,x}$ indicates differentiation with respect to x, and $h = R_{\mathrm{k}}^{-1}$ is the (a priori unknown)"Kapitza conductance." Equations (5.4) and (5.5), relate the convective heat transfer of the interface, modeled as a fictitious "gas", to the thermal conductivity in the adjacent unthermostatted bins. This reasoning leads to a form similar to the approach of Pitaveskii and Lifshitz [49, pages 51–53], who proposed the following phenomenological model for the jump in temperature due to the Kapitza effect,

$$\theta(0) - \theta_{\mathrm{L}} = \eta_{\mathrm{jump}}\theta_{,x}(0), \tag{5.6}$$

where η_{jump} is called the temperature discontinuity coefficient. Comparing Eqs. (5.5) and (5.6), we have $\eta_{\mathrm{jump}} = k/h$.

Substituting Eq. (5.2) into Eqs. (5.4) and (5.5), and solving for a_1 and a_2, we obtain

$$a_1 = \frac{\Delta\theta}{2k/h + L_m}, \quad a_2 = \frac{(k/h + L_m)\theta_{\mathrm{L}} + (k/h)\theta_{\mathrm{M}}}{2k/h + L_m}, \tag{5.7}$$

where $\Delta\theta = \theta_{\mathrm{M}} - \theta_{\mathrm{L}}$. Substituting these values back into Eq. (5.2), and evaluating at $x = 0$ and $x = L_m$, we obtain

$$\theta_L^* \equiv \theta(0) = a_2, \tag{5.8}$$

$$\theta_M^* \equiv \theta(L_m) = a_1 L_m + a_2. \tag{5.9}$$

The star superscripts indicate that these are the extrapolated temperatures at the ends of the left half of the nanobeam and not the values set by the thermostats. The heat flux through the nanobeam under steady-state conditions is

$$q_{\mathrm{ss}} = -k\theta_{,x} = -k\frac{\Delta\theta^*}{L_m}, \tag{5.10}$$

where $\Delta\theta^* = \theta_M^* - \theta_L^*$. Using Eqs. (5.2) and (5.4), the above equation can also be written as

$$q_{\text{ss}} = -ka_1 = h[\theta_{\text{L}} - \theta(0)]. \tag{5.11}$$

The thermal conductivity k increases with increasing beam length [40, 52] and approaches the bulk value k_∞ as the length goes to infinity, i.e.,

$$k_\infty = \lim_{L_m \to \infty} k(L_m). \tag{5.12}$$

The physical reason for this size dependence is due to the availability of acoustic phonons of longer mean free paths. Long wavelength phonons on the scale of hundreds of lattice constants carry significant heat. As a phonon's mean free path approaches the beam length L_m, its contribution to the thermal conductivity reduces. Moreover, phonons with longer mean free paths travel ballistically along the beam without diffusing through multiple collisions. This allows them to enter the periodic system multiple times and interfere with the system randomly, which is another reason for the size dependent reduction in the values of computed thermal conductivities [145]. The dependence of k on beam length is also affected by the choice of thermostat and its parameters. A separate issue is whether the size dependence is linear or nonlinear. This will be addressed below.

Our objective is to obtain the physical, limiting value, k_∞ defined in Eq. (5.12). In principal, one can perform simulations of increasing beam length until the value of k appears to converge. However, in practice, this convergence is very slow and the computational expense of the simulations becomes prohibitive. As an alternative, we propose the following phenomenological relation for the steady-state heat flux, relating it to the temperature difference across the nanobeam (exclusive of the thermostats) $\Delta\theta^*$, and the thermostat damping time ϵ:

$$q_{\text{ss}} = -\frac{\Delta\theta^*}{c_0 L_m + c\epsilon^\alpha}, \tag{5.13}$$

where c_0, c and α are constants. The power law dependence for ϵ is motivated by our numerical simulations.

The expression in Eq. (5.13) makes it possible to fit the model (and hence predict the bulk thermal conductivity) by performing a set of simulations with different lengths

and ϵ values without having to go to the large lengths needed by the standard NEMD direct approach. The result is a significant reduction in computation time.

The functional form in Eq. (5.13) ensures that as $L_m \to \infty$, the steady state heat flux is independent of ϵ and tends to zero (since $\Delta\theta^*$ tends to $\Delta\theta$ as L_m tends to infinity). Equating Eqs. (5.10) and (5.13), we have

$$\frac{1}{k} = \frac{1}{k_\infty} + \frac{c\epsilon^\alpha}{L_m}, \tag{5.14}$$

where we have set $1/c_0 = k_\infty$ to ensure that Eq. (5.12) is satisfied.

The linear dependence of $1/k$ on $1/L_m$ in Eq. (5.14) has been put into question by recent studies. Sellan et al [117] find that the linear model is only accurate when the minimum length used in the simulations is comparable to the largest mean free paths of the phonons that dominate the thermal transport. They proposed adding to Eq. (5.14) a higher-order dependence on $1/L_m$. Allen [145] concluded that the extrapolation procedure should include fractional powers of $1/L_m$ based on a model that includes a nonlocal dependence of the heat current on the temperature gradient. In our simulations of solid argon, the heat current appears nearly constant away from the thermostats (see Figure 4.2) suggesting that nonlocal effects would be small. Nevertheless, it is of interest to explore the change in temperature gradient and heat current along the beam to make contact with the nonlocal model of Allen [145]. Figure 5.2 presents the absolute values of the temperature gradient and thermal conductivity for bins away from thermostats for the case of $\epsilon = 1.0$ ps shown in Fig. 4.2. Comparing Fig. 5.2(b) in this work and Fig. 3 in Allen [145], we note some similarities. This suggests that the nonlocal model may be a promising approach, in particular in case where the temperature gradients vary significantly.

In order to later test whether the higher-order effects of Sellan et al [117] or the fractional dependence of Allen [145] are important for argon, we consider an alternative model to Eq. (5.14):

$$\frac{1}{k} = \frac{1}{k_\infty} + \frac{c\epsilon^\alpha}{L_m^{p_1}} + \frac{d}{L_m^{p_2}}, \tag{5.15}$$

where $d \leq 0$ is a fitting constant and p_1, p_2 are power law coefficients to be selected. We explore the differences in the prediction of the linear model in Eq. (5.14) and the nonlinear model in Eq. (5.15) in Section 5.2.

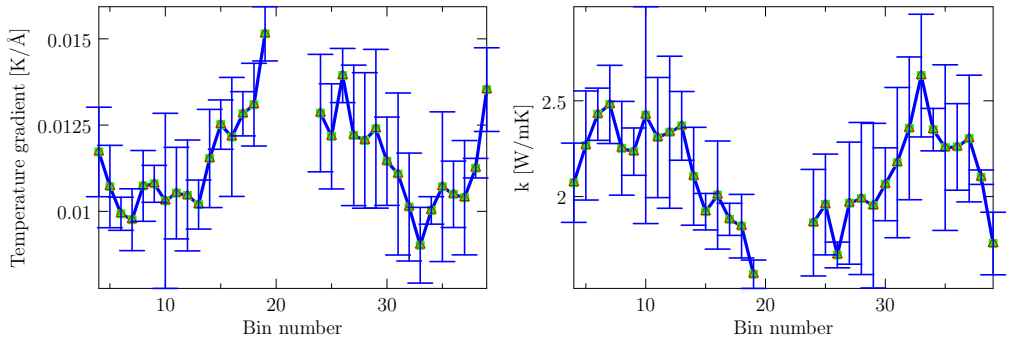

Figure 5.2: (a) Temperature gradients, $|\partial\theta/\partial x|_n = |(\theta_{n+1} - \theta_{n-1})/(x_{n+1} - x_{n-1})|$, and (b) thermal conductivities, $k_n = q_n|\partial\theta/\partial x|_n^{-1}$, where the subscript n refers to the bin number. Only bins away from the thermostats have been included. The argon beam is of size $123 \times 4 \times 4$ unit cells with $\theta_{\rm L} = \theta_{\rm R} = 12.5$ K and $\theta_{\rm M} = 17.5$ K, and $\epsilon = 1.0$ ps.

In addition to thermal conductivity, we can obtain an expression for the Kapitza resistance $R_{\rm k}$ at the interface between the thermostatted and unthermostatted regions. Using Eqs. (5.7), (5.8) and (5.11), we have

$$R_{\rm k} = -\frac{1}{2}\left(\frac{\Delta\theta}{q_{\rm ss}} + \frac{L_m}{k}\right). \tag{5.16}$$

Moreover, substituting $q_{\rm ss}$ from Eq. (5.13) and k from Eq. (5.14) into Eq. (5.16) and using $c_0 = 1/k_\infty$, $R_{\rm k}$ can be written as

$$R_{\rm k} = -\frac{1}{2}\left(1 - \frac{\Delta\theta}{\Delta\theta^*}\right)\left(\frac{L_m}{k_\infty} + c\epsilon^\alpha\right). \tag{5.17}$$

Finally, the temperature jump due to the Kapitza effect $\delta\theta$ can be obtained from Eqs. (5.4) and (5.5). Noting from Eq. (5.2) that $\theta_{,x} = a_1$ and using the solution for a_1 in Eq. (5.7), we find that the temperature jump is equal on both ends, $\delta\theta = \theta_L^* - \theta_{\rm L} = \theta_{\rm M} - \theta_M^*$, and given by

$$\delta\theta = \frac{\Delta\theta}{2 + L_m\left(kR_{\rm k}\right)^{-1}}. \tag{5.18}$$

5.1.2 Procedure for obtaining bulk thermal conductivity

To summarize, the procedure for obtaining the bulk thermal conductivity k_∞ is as follows:

(I) The thermal conductivity k is calculated for different beam lengths (L_m) and thermostat damping times (ϵ) using using the NEMD direct method.

(II) The data for different k, L_m and ϵ are fit to Eq. (5.14) or Eq. (5.15) to obtain the k_∞.

5.2 Results for argon with Langevin thermostatting

In order to explore whether the phenomenology of the previous section is adequate, we apply it to results from NEMD simulations of argon nanobeams for different lengths ranging from 45 to 603 unit cells and Langevin thermostats damping times, at $\theta_{\rm L} = 12.5$ K and $\theta_{\rm M} = 17.5$ K. Figure 5.3(a) shows the plots of $|q_{\rm ss}|$ versus ϵ for different lengths of the nanobeam (not all computed lengths are shown), and Fig. 5.3(b) shows the inverse thermal conductivity versus inverse length for different damping parameters. We see that the $1/k$ versus $1/L_m$ curves converge to the same value of $1/k_\infty$ with different slopes that depend on ϵ. The key result is in Fig. 5.3(c), which shows that the results in Fig. 5.3(b) largely collapse onto a single curve when the relation in Eq. (5.14) is used with the following parameters obtained by fitting the data to the curve: $c = 17.37 \pm 1.13$ ps$^{1-\alpha}$m^{2}K/Joules, $\alpha = 0.20 \pm 0.04$, and $k_\infty = 2.35 \pm 0.03$ W/mK with a 95% confidence interval. The goodness of fit measured by the adjusted R^2 is 0.97. These parameters quantify the dependence of the bulk thermal conductivity on the nanobeam length and Langevin damping time at the given temperature, $\bar{\theta} = (\theta_{\rm L} + \theta_{\rm M})/2 = 15$ K. This makes it clear that the length dependence is not just due to physical effects, but also depends on the details of the thermostatting. Only the limiting value, k_∞, is a physical material property. This value is in good agreement with the MD simulations of Kaburaki et al [129] which give 2.38 ± 0.09 W/mK, and with the theoretical prediction of 2.20 W/mK reported in Table II of Christen and Pollack [146].

Fitting the data with the nonlinear model in Eq. (5.15) with $p_1 = 1$ and $p_2 = 2$, we obtain $k_\infty = 2.36 \pm 0.05$ W/mK, $c = 18.73 \pm 4.47$ ps$^{1-\alpha}$m^{2}K/Joules, $\alpha = 0.18 \pm 0.06$, and $d = (-140.1 \pm 49.1) \times 10^{-20}$ m^{3}K/W, with adjusted R^2 = 0.97. In order to test a fractional order model, we set $d = 0$ and $p_1 = 0.5$ in Eq. (5.15). Fitting the data, we obtain $k_\infty = 2.67 \pm 0.09$ W/mK with adjusted R^2 = 0.93. This result is significantly different from the Green-Kubo and experimental results and therefore we conclude that

this model is not suitable. We also checked other fractional and higher-order models, but in all cases found that they either provided similar k_∞ as obtained by fitting the linear model in Eq. (5.14), or they deviated significantly from Green-Kubo values. Based on this we conclude that nonlinear effects are not significant for argon. However preliminary results for silicon (not reported here) reveal that there the linear model is inadequate. These observations are consistent with those of Sellan et al [117], who argued that the thermal conductivity of solid argon is dominated by phonons with mean free paths that are spread over a small range (0.5–3 nm at 40 K), and therefore phonon properties can be approximated reasonably by an average mean free path. This leads to a linear dependence of $1/k$ on $1/L_m$. The spread in phonon mean free paths is much greater for silicon, and hence the linear dependence breaks down.

An advantage of using Eq. (5.14) or Eq. (5.15) compared with the standard NEMD direct method that does not account for thermostat damping is that good results can be obtained with smaller system sizes. To demonstrate this we include only those data for which $45 \leq L \leq 105$ unit cells. Fitting to the linear model in Eq. (5.14), we obtain $k_\infty = 2.35 \pm 0.08$ W/mK, which is identical to the result obtained with lengths up to 603 unit cells at a significantly lower computational cost.

The plots of R_k and $\delta\theta$ versus ϵ, computed using Eqs. (5.17) and (5.18), respectively, for different lengths of the nanobeam are presented in Fig. 5.4. It is clear from Fig. 5.4(a) that the Kapitza resistance depends strongly on the damping parameter but is insensitive to the length of the beam. This is not surprising since this resistance is a local effect that depends primarily on the physics occurring close to the interface. In contrast, the temperature jump, $\delta\theta$, depends on both the damping parameter and beam length. Figure 5.4(b) shows that the jump is decreased either by increasing the length of the beam or the damping time ϵ up to a value of about 0.5 ps (beyond this value the temperature jump slowly increases with ϵ).

The simulations were repeated for different temperatures and similar trends were observed. Figure 5.5 shows the dependence of k_∞ and the phenomenological coefficients c and α appearing in Eq. (5.14) on the temperature. We see that the bulk thermal conductivity decreases with increasing temperature. This is an expected physical effect, since the mean free path decreases with increasing temperature [129, 146]. The coefficient c increases with increasing temperature, whereas the exponent α is insensitive to

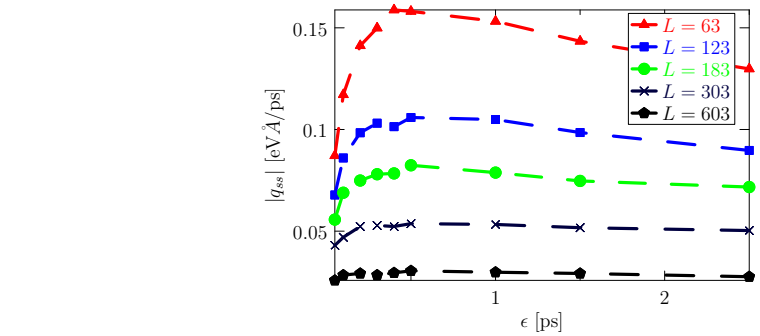

(a)

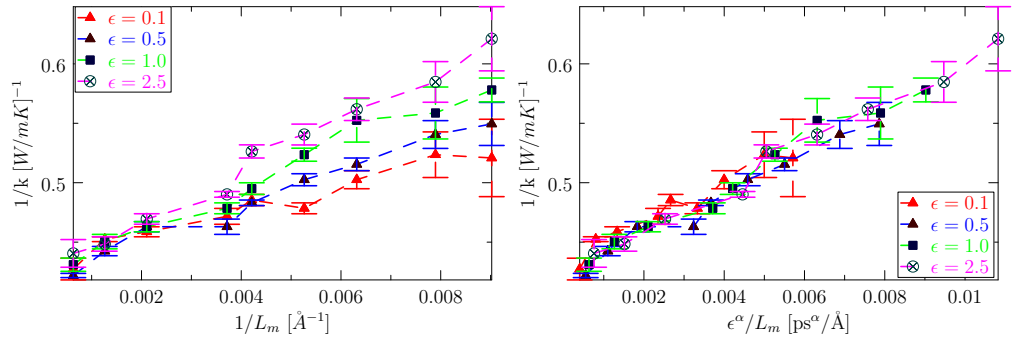

(b) (c)

Figure 5.3: For $\theta_{\mathrm{L}} = 12.5$ K and $\theta_{\mathrm{R}} = 17.5$ K: (a) Plots of $|q_{\mathrm{ss}}|$ versus ϵ for $L = 63, 123, 183, 303, 603$ unit cells; Plots of (b) $1/k$ versus ϵ/L_m and (c) $1/k$ versus ϵ^α/L_m for different damping times and various lengths.

temperature. It may be possible to extend the proposed phenomenology by postulating a functional form for the temperature dependence of c and assuming a constant α, but we have not attempted to do so here.

5.3 Summary

In the NEMD direct method, thermal conductivity is computed by applying a temperature gradient across a system by thermostatting the ends to different temperatures and measuring the steady state heat flux. The thermal conductivity then follows from

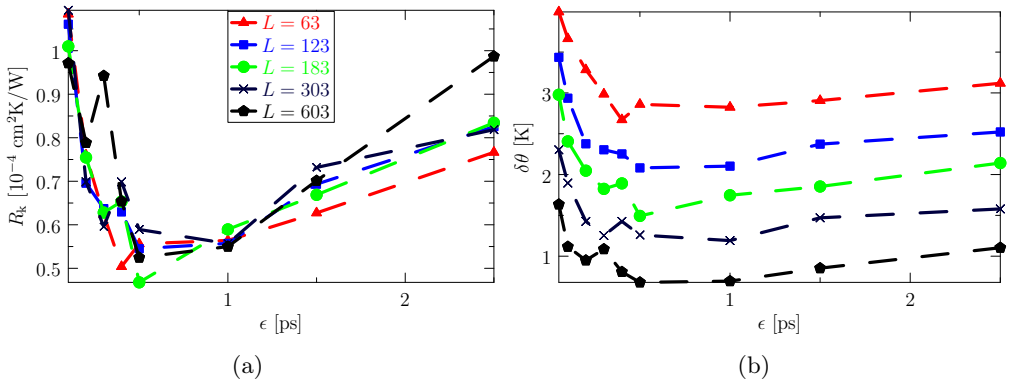

(a) (b)

Figure 5.4: Plots of (a) $R_{\rm k}$ versus ϵ, and (b) $\delta\theta$ versus ϵ for $L = 63, 123, 183, 303, 603$ unit cells, for $\theta_{\rm L} = 12.5$ K and $\theta_{\rm R} = 17.5$ K.

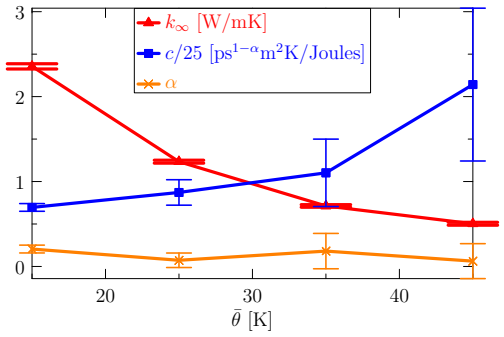

Figure 5.5: Plots of k_∞, c and α versus $\bar{\theta}$.

Fourier's law. A problem with this approach is that due to an artificial Kapitza resistance at the interfaces between the thermostatted and unthermostatted regions, there is an abrupt change between the temperature maintained by a thermostat and the temperature experienced by the system across the interface. As a result, the thermal conductivity obtained from the NEMD direct method depends on the length of the system, the thermostatting algorithm, and its parameters. In this chapter, we have proposed linear and nonlinear phenomenological models in Eqs. (5.14) and (5.15), which account for the dependence of the thermal conductivity on these variables. These relations make it possible to compute the system-independent bulk thermal conductivity by performing a number of simulations at different lengths and with different thermostat parameters, and fitting to either Eq. (5.14) or Eq. (5.15). The main advantage of the approach is that by

explicitly accounting for the thermostat parameters, good results can be obtained with smaller system sizes than needed to obtain converged results with the standard direct NEMD approach.

Chapter 6

Hybrid KMC-continuum modeling in silicon nanobeams

The Si(001) surface attracts much attention since most silicon devices are fabricated on it. This surface is known to undergo a simple reconstruction that involves the formation of rows of dimers along $\langle 110 \rangle$ directions [147]. Historically, Schlier and Farnsworth [148] using low-energy electron diffraction (LEED) measurements first discovered the $p(2 \times 1)$ structure, which involves 2×1 periodic cells of the ideal surface structure. Later LEED experiments detected a $c(4 \times 2)$ pattern [149, 150]. Scanning tunneling microscopy (STM) studies of the Si(001) surface at room temperature show both symmetric and asymmetric $p(2 \times 1)$ reconstructions [151]. The ground state configuration of the Si(001) surface at low temperature is still an issue of debate with arguments made for symmetric $p(2 \times 1)$ [152], asymmetric $p(2 \times 1)$ [153], $c(4 \times 2)$ [154], and a mixture of $c(4 \times 2)$, $p(2 \times 2)$ and asymmetric $p(2 \times 1)$ [155, 156, 157]. Several authors [158, 159, 160, 161, 162] have studied the energetics of silicon surface reconstruction and provide estimates for the latent heat released per dimer from the ideal unreconstructed structure to the symmetric $p(2 \times 1)$, asymmetric $p(2 \times 1)$, $c(4 \times 2)$ and other reconstructions.

In this chapter, we study how the released latent heat, which is delivered to the material as a localized heat pulse, can cause a significant increase in temperature in nanostructures. To motivate this, Fig. 6.1 shows the results of a non-equilibrium molecular dynamics (NEMD) simulation of a silicon nanobeam with exposed $\{001\}$ surfaces

modeled using the Stillinger-Weber (SW) potential [115]. The nanobeam temperature is initially 10 K and then the temperatures of both ends are raised to 30 K and maintained at this level. The figure shows a series of temperature profiles at increasing time. The interior of the beam gradually heats up, but rather than stabilizing at 30 K as expected, a dramatic overshooting in temperature that exceeds 200 K occurs due to release of latent heat that accompanies dimer formation in the reconstruction process. The maximum temperature is reached after 231 ps after which the temperature gradually decreases back to 30 K as the excess heat is absorbed at the ends.

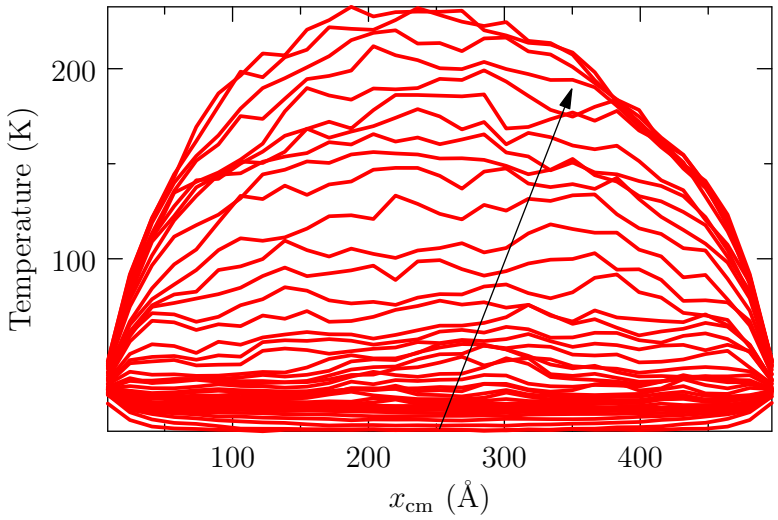

Figure 6.1: NEMD temperature profiles at increasing time for a silicon nanobeam of size $505 \times 16.3 \times 16.3$ Å with an initial temperature of 10 K and with the ends held at 30 K. Each profile is an average over 3 ps. The arrow indicates the direction of increasing time.

To model this phenomenon we use a continuum partial differential equation (PDE) for non-Fourier heat transfer [2] parametrized using a novel thermal parameter identification (TPI) scheme based on an iteratively reweighted least squares (IRLS) regression method [56]. The injection of energy due to the latent heat released by dimerization is modeled using a stochastic Kinetic Monte Carlo (KMC) algorithm [57] that is coupled to the continuum PDE through the source term. The KMC rates are estimated using harmonic transition state theory (h-TST) with the activation barrier for dimer formation computed from the atomistic model using the climbing-image nudged elastic band (CI-NEB) method [58].

The structure of the chapter is as follows. In Section 6.1, we begin with a brief overview of Fourier and non-Fourier heat conduction models. In Section 6.2, we describe the TPI-IRLS procedure for extracting thermal parameters from the NEMD temperature profiles obtained prior to surface reconstruction. The results of applying TPI-IRLS to silicon are described in Section 6.3. In Section 6.4, the surface reconstruction on the Si(001) surface and activation barriers for dimerization are studied. In Section 6.5, we describe the hybrid continuum-KMC method that models the latent heat released during the surface reconstruction process and predicts the evolution of the temperature profiles. We conclude in Section 6.6 with a summary and suggestions for future work. [1]

6.1 Fourier and non-Fourier heat transfer models

The simplest theory of heat conduction assumes Fourier's law. For a one-dimensional (1D) homogeneous body, this can be written as

$$q = -k(\theta)\frac{\partial \theta}{\partial x}, \tag{6.1}$$

where $q = q(\boldsymbol{x}, t)$ and $\theta = \theta(\boldsymbol{x}, t)$ are the heat flux and temperature, respectively, at position x in the current configuration at time t, and $k(\theta)$ is the temperature-dependent thermal conductivity.

The energy equation for a rigid solid body without heat sources is (see for example Section 10.2 in Ref. [1])

$$\frac{\partial e}{\partial t} = \gamma \frac{\partial \theta}{\partial t} = -\frac{\partial q}{\partial x}, \tag{6.2}$$

where $e = e(\boldsymbol{x}, t)$ is the internal energy per unit volume and $\gamma = \partial e/\partial \theta$ is the volumetric heat capacity. Substituting the expression for $q(\boldsymbol{x}, t)$ in Eq. (6.1) into Eq. (6.2), we obtain Fourier's heat equation for a temperature-dependent thermal conductivity:

$$\gamma \frac{\partial \theta}{\partial t} = k'(\theta)\left(\frac{\partial \theta}{\partial x}\right)^2 + k(\theta)\frac{\partial^2 \theta}{\partial x^2}, \tag{6.3}$$

where $k' = dk/d\theta$. This is a parabolic PDE that describes heat transfer as a diffusive process and assumes infinite speed of heat propagation.

[1] Some miscellaneous works were also done. More prominent among them is the analysis of phonons on silicon nanobeams. The readers are suggested to contact the author to know more about the work.

In order to account for wavelike heat propagation at finite speed, Cattaneo [7, 8] and Vernotte [9, 10] introduced a relaxation time τ_q into the heat flux constitutive relation in Eq. (6.1). This leads to a non-Fourier model for heat flux:

$$\tau_q \frac{\partial q}{\partial t} + q = -k(\theta)\frac{\partial \theta}{\partial x}. \tag{6.4}$$

Taking the derivative of Eq. (6.4) with respect to x and substituting in the energy equation in Eq. (6.2), yields the Cattaneo-Vernotte (CV) wave equation,

$$\gamma\tau_q \frac{\partial^2 \theta}{\partial t^2} + \gamma \frac{\partial \theta}{\partial t} = k'(\theta)\left(\frac{\partial \theta}{\partial x}\right)^2 + k(\theta)\frac{\partial^2 \theta}{\partial x^2}. \tag{6.5}$$

An alternative non-Fourier model for heat transfer was proposed by Joseph and Preziosi [2] based on earlier work by Gurtin and Pipkin [67] and Nunziato [68]. They refer to their model as a "Jeffreys-type" heat flux constitutive relation due to an analogy with a stress model developed by Jeffreys [163]. The Jeffreys-type model has the form [143]:

$$\tau_q \frac{\partial q}{\partial t} + q = -k(\theta)\frac{\partial \theta}{\partial x} - \tau_\theta k(\theta)\frac{\partial^2 \theta}{\partial x \partial t}, \tag{6.6}$$

where τ_θ is an additional relaxation time. Following the procedure outlined above leads to a Jeffreys-type equation for the temperature:

$$\gamma\tau_q \frac{\partial^2 \theta}{\partial t^2} + \gamma \frac{\partial \theta}{\partial t} = k'(\theta)\left(\frac{\partial \theta}{\partial x}\right)^2 + k(\theta)\frac{\partial^2 \theta}{\partial x^2} \tag{6.7}$$

$$+ \tau_\theta \left[k'(\theta)\frac{\partial \theta}{\partial x}\frac{\partial^2 \theta}{\partial x \partial t} + k(\theta)\frac{\partial^3 \theta}{\partial x^2 \partial t}\right]. \tag{6.8}$$

Assuming the following phenomenological relation for the thermal conductivity,

$$k(\theta) = k_0\big(\theta/\theta_0\big)^s, \tag{6.9}$$

where k_0 is the thermal conductivity at temperature θ_0, and s is a real exponent, the Jeffreys-type equation can be written as

$$\frac{\partial \theta}{\partial t} = -\tau_q \frac{\partial^2 \theta}{\partial t^2} + \frac{k_0}{\gamma}\left[\Big(\frac{\theta}{\theta_0}\Big)^s \left(\frac{s}{\theta}\Big(\frac{\partial \theta}{\partial x}\Big)^2 + \frac{\partial^2 \theta}{\partial x^2}\right)\right]$$

$$+ \frac{k_0 \tau_\theta}{\gamma}\left[\Big(\frac{\theta}{\theta_0}\Big)^s \left(\frac{s}{\theta}\frac{\partial \theta}{\partial x}\frac{\partial^2 \theta}{\partial x \partial t} + \frac{\partial^3 \theta}{\partial x^2 \partial t}\right)\right]. \tag{6.10}$$

The CV wave equation and the Fourier equation follow from this equation as special cases with $\tau_\theta = 0$ and $\tau_q = \tau_\theta = 0$, respectively.

6.2 Obtaining thermal parameters using the TPI-IRLS method

As a first step toward modeling the behavior in Fig. 6.1, we seek to obtain the thermal parameters appearing in the continuum models described in Section 6.1 by performing NEMD simulations of silicon nanobeams with free ideal (001) surfaces. We choose a slender nanobeam of length L and square cross-section of side W with $L \gg W$. Given the slender nanobeam geometry, we approximate the three-dimensional (3D) heat transfer problem as 1D consistent with the derivation in Section 6.1.

In order to apply temperature boundary conditions (BCs) for computing thermal parameters, the nanobeam is divided into N_{bins} bins of equal size as shown for example in Fig. 6.2(a) for $N_{\text{bins}} = 11$. The bins centers are located at $x_n = \Delta_x/2 + (n-1)\Delta_x$ $(n = 1, \ldots, N_{\text{bins}})$, where Δ_x is the bin length along the x-direction. The instantaneous temperature in a given bin is computed as a spatial average over the appropriate phase function across all atoms within it. The thermodynamic temperature of a bin is obtained as a time average of the instantaneous bin temperature over a predefined time interval of Δ_t (see details in Ref. [143]). In order to improve the statistics, simulations can be repeated multiple times with different initial conditions drawn from a distribution associated with the initial temperature. Bin averages are then computed over all realizations of a given bin.

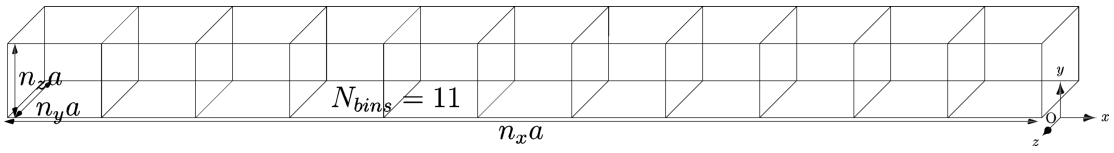

(a)

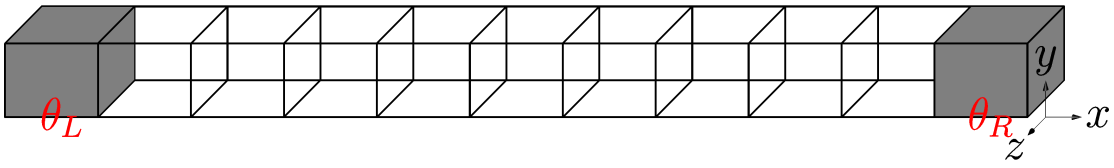

(b)

Figure 6.2: (a) Division of a nanobeam into bins in an NEMD simulation. (b) Thermal BCs applied to the beam for the TPI-IRLS method. Shaded regions are thermostatted.

Initially, at time $t = 0$, the nanobeam has a uniform temperature θ_0:

$$\theta(x, 0) = \theta_0, \qquad 0 < x < L. \tag{6.11}$$

Next the temperatures of the bins at the left and right ends of the nanobeam are set to new values, θ_{L} and θ_{R}:

$$\theta(0, t) = \theta_{\mathrm{L}}, \quad \theta(L, t) = \theta_{\mathrm{R}}. \tag{6.12}$$

In the NEMD simulations, the temperature BCs are applied to the bins at the ends of the nanobeam using a suitable thermostat as shown in Fig. 6.2(b).

In the TPI-IRLS approach, an NEMD simulation is performed starting with the initial condition in Eq. (6.11) and with the BCs specified in Eqs. (6.12). The resulting spatio-temporal temperature profiles after binning are then smoothed and a least squares regression method is used to determine the Jeffreys-type model parameters, k_0, τ_q and τ_θ, appearing in Eq. (6.10). (The same procedure can be applied to the Fourier or CV models to obtain their parameters.)[2] We assume that the volumetric heat capacity γ is constant over the temperature range of the simulation. We compute γ from a separate molecular dynamics simulation at a temperature equal to the average of initial and BC temperatures.

6.2.1 Temperature profile smoothing

The binning procedure described above yields the temperature θ_{mn} of bin n ($n = 1, \ldots, N_{\mathrm{bins}}$) at time $t_m = m\Delta_t$ ($m = 0, 1, \ldots, N_{\mathrm{profiles}}$), where N_{profiles} is the number of stored temperature profiles. In the following, we refer to the initial $m = 0$ profile as the "zeroth profile."

Although the bin temperatures θ_{mn} are obtained as an average over multiple NEMD simulations with different initial conditions, this data is still expected to be quite noisy due to the stochastic nature of NEMD and the small system size being studied. Therefore before attempting to fit this data to the continuum model in Eq. (6.10), it is necessary

[2] Note that the TPI-IRLS approach differs from the TPI method we describe in Ref. [143], where an analytical solution for a decaying initial sinusoidal temperature profile is used to extract thermal parameters. A different approach is needed because the TPI method assumes that the thermal conductivity is independent of temperature, whereas in the present case the change in temperature is large and this assumption is not valid.

to apply a suitable smoothing procedure. We follow Müller and Timmer [164] and seek a surface $\tilde{\theta}(x,t)$ in x–t space that "best" approximates the discrete bin data θ_{mn}.

Different choices for the form of $\tilde{\theta}(x,t)$ can be made. Schoenberg [165] and Reinsch [166] suggested that a natural cubic spline was optimal for smoothing noisy data. However, splines have the propensity to follow the data too closely. At the other extreme, a least squares linear fit captures the average slope of the data without tracking deviations from the mean. We adopt a method described by de Boor [167] that uses a "smoothing parameter" α to balance between smoothness and closeness to the data. In this approach, $\alpha = 0$ corresponds to a cubic spline and $\alpha = 1$ corresponds to a linear least squares fit, with intermediate values corresponding to a mixture of the two. By tuning the value of α in the range [0,1], the level of agreement with the data can be controlled. Since our data is discretized in both space x and time t, smoothing is performed with a two-dimensional surface spline in the directions x and t. The smoothing parameters in these directions are taken to be

$$\alpha_x = e_x/(1+e_x), \quad \alpha_t = e_t/(1+e_t), \tag{6.13}$$

where

$$e_x = ((\Delta_x)^3/16) \times 10^{a_p}, \quad e_t = ((\Delta_t)^3/16) \times 10^{a_p}.$$

The power a_p can vary from 1 to 10. A value of $a_p = 1$ was used in most of our calculations. Data from the thermostatted bins is excluded in the smoothing procedure.

6.2.2 Iteratively reweighted least squares regression (IRLS)

Next we turn to the least squares parameter extraction technique. The Jeffreys-type equation in Eq. (6.10) is assumed to hold at all points along the nanobeam at all time. It therefore holds at the bin centers x_n ($n = 2, \ldots, N_{\text{bins}} - 1$) at times t_m ($m = 1, 2, \ldots, N_{\text{profiles}}$). This provides a system of $N_{\text{data}} = (N_{\text{bins}}-2) \times N_{\text{profiles}}$ equations with which to determine the parameter vector $\boldsymbol{p} = (p_1, p_2, p_3)^T = (\tau_q, k_0/\gamma, k_0\tau_\theta/\gamma)^T$. Formally, we write

$$\partial_t\theta|_{mn} = f(\boldsymbol{p}, \partial_{tt}\theta|_{mn}, \partial_{xx}\theta|_{mn}, \partial_{xxt}\theta|_{mn}; s), \tag{6.14}$$

where $\partial_t\theta \equiv \frac{\partial\theta}{\partial t}$, $\partial_{tt}\theta \equiv \frac{\partial^2\theta}{\partial t^2}$, $\partial_{xx}\theta \equiv \left(\frac{\theta}{\theta_0}\right)^s\left(\frac{s}{\theta}\left(\frac{\partial\theta}{\partial x}\right)^2+\frac{\partial^2\theta}{\partial x^2}\right)$, and $\partial_{xxt}\theta \equiv \left(\frac{\theta}{\theta_0}\right)^s\left(\frac{s}{\theta}\frac{\partial\theta}{\partial x}\frac{\partial^2\theta}{\partial x\partial t}+\frac{\partial^3\theta}{\partial x^2\partial t}\right)$, for a given value of s (the thermal conductivity exponent defined in Eq. (6.9)). The notation $(\cdot)|_{mn}$ means that the argument is evaluated at position x_n at time t_m. So for example $\partial_{tt}\theta|_{mn} = (\partial^2\theta/\partial t^2)|_{(x_n,t_m)}$. Equation (6.14) is now approximated by replacing $\theta(x,t)$ with the function $\tilde{\theta}(x,t)$ obtained by the smoothing procedure described in the previous section:

$$\partial_t\tilde{\theta}|_{mn} = f(\boldsymbol{p}, \partial_{tt}\tilde{\theta}|_{mn}, \partial_{xx}\tilde{\theta}|_{mn}, \partial_{xxt}\tilde{\theta}|_{mn}; s). \tag{6.15}$$

The derivatives are computed from the surface spline function.

From a regression standpoint, we take the left-hand side of Eq. (6.15), $y_{mn} = \partial_t\tilde{\theta}|_{mn}$, to be the *dependent variable*, and the variables on the right, $\boldsymbol{X}_{mn} = (-\partial_{tt}\tilde{\theta}|_{mn}, \partial_{xx}\tilde{\theta}|_{mn}, \partial_{xxt}\tilde{\theta}|_{mn})^T$, to be the *regressors* (or "independent variables"). We now assume that the parameters $\boldsymbol{p}$ are constant over the range of temperatures being explored. We again emphasize that the regressors depend upon s, so that $\boldsymbol{p}$ is being estimated for a given value of s. We drop s in the formal representation for the sake of clarity.

Examining Eq. (6.10), we see that a linear relationship exists between y_{mn} and $\boldsymbol{X}_{mn}$,

$$y_{mn} = \boldsymbol{X}_{mn}\cdot\boldsymbol{p} + R_{mn}, \tag{6.16}$$

where R_{mn} are residual terms representing the noise in the data. The residuals are not known *a priori* and are obtained by inverting Eq. (6.16) for a given choice of $\boldsymbol{p}$,

$$R_{mn}(\boldsymbol{p}) = y_{mn} - \boldsymbol{X}_{mn}\cdot\boldsymbol{p}. \tag{6.17}$$

The N_{data} equations in Eq. (6.16) can be represented in compact form as

$$\boldsymbol{y} = \boldsymbol{X}\boldsymbol{p} + \boldsymbol{R}, \tag{6.18}$$

where $\boldsymbol{y} = \{y_{mn}\}$ and $\boldsymbol{R} = \{R_{mn}\}$ are $N_{\text{data}}\times 1$ vectors and $\boldsymbol{X} = \{\boldsymbol{X}_{mn}\}$ is an $N_{\text{data}}\times 3$ array. This system of equations is overdetermined since there are only three unknowns (the parameters p_1, p_2 and p_3) whereas the number of equations is $N_{\text{data}} \gg 3$. A coefficient inversion problem [168] must therefore be solved by minimizing the sum of

the square of the residuals

$$\begin{aligned}\Gamma(\boldsymbol{p}) &= \sum_{m,n} \left(R_{mn}(\boldsymbol{p})\right)^2 \\ &= \sum_{m,n} (y_{mn} - \boldsymbol{X}_{mn} \cdot \boldsymbol{p})^2 \equiv \|\boldsymbol{y} - \boldsymbol{X}\boldsymbol{p}\|_2^2. \end{aligned} \tag{6.19}$$

This is known as the l^2-norm least squares regression method. A limitation of this approach is that it *a priori* assumes that the system is *homoscedastic*, i.e., that the random noise variables R_{mn} all have the same variance. If this is not the case and the system is *heteroscedastic*, and the results obtained by minimizing $\Gamma(\boldsymbol{p})$ will be invalid. Instead, a method that corrects for heteroscedasticity by estimating the variance of the variables along with the parameters must be used. An example of such an approach is the IRLS (iteratively reweighted least squares) regression method. We follow the IRLS implementation of the hybrid l^2–l^1 norm adopted by Guitton and Verschuur [56], where the minimizing function is

$$\Gamma_W(\boldsymbol{p}) = \|\boldsymbol{W}(\boldsymbol{y} - \boldsymbol{X}\boldsymbol{p})\|_2^2, \tag{6.20}$$

and $\boldsymbol{W}$ is the following diagonal $N_{\text{data}} \times N_{\text{data}}$ weighting matrix:

$$\boldsymbol{W} = \text{diag}\left(\frac{1}{(1 + R_{mn}^2/\epsilon^2)^{1/4}}\right). \tag{6.21}$$

Here ϵ is a scaling constant that we take to be

$$\epsilon = \max \frac{|\boldsymbol{y}|}{100}. \tag{6.22}$$

With this choice of $\boldsymbol{W}$, minimizing $\Gamma_W(\boldsymbol{p})$ is equivalent to minimizing [56]:

$$\mathcal{Z}(\boldsymbol{p}) = \sum_{m,n} z(R_{mn}(\boldsymbol{p})) = \sum_{m,n} \left(\left[1 + R_{mn}(\boldsymbol{p})/\epsilon\right]^{1/2} - 1 \right), \tag{6.23}$$

where $R_{mn}(\boldsymbol{p})$ is given in Eq. (6.17). For a given residual R_{mn}, we have

$$z(R_{mn}) \approx \begin{cases} \frac{1}{2}\left(R_{mn}/\epsilon\right)^2 & \text{for small } |R_{mn}|/\epsilon, \\ |R_{mn}|/\epsilon, & \text{for large } |R_{mn}|/\epsilon. \end{cases} \tag{6.24}$$

Hence, we obtain an l^2 treatment for small residuals and an l^1 treatment for large residuals with a smooth transition between the two determined by the parameter ϵ.

The IRLS algorithm consists of iteratively recomputing the weights $\boldsymbol{W}$ and the parameters $\boldsymbol{p}$ until a convergence criterion is satisfied. The algorithm proceeds as follows. Given $\boldsymbol{p}^{(k)}$ (the parameters vector at iteration k) the residual at iteration k follows from Eq. (6.17) and the corresponding weighting matrix $\boldsymbol{W}^{(k)}$ from Eq. (6.21). The values of the parameters at iteration $k+1$ are then obtained by solving the weighted linear least squares problem:

$$\begin{aligned} \boldsymbol{p}^{(k+1)} &= \arg\min_{\boldsymbol{p}} \|\boldsymbol{W}^{(k)}\left(\boldsymbol{y}-\boldsymbol{X}\boldsymbol{p}\right)\|_2^2 \\ &= \left(\boldsymbol{X}^T\boldsymbol{W}^{(k)}\boldsymbol{X}\right)^{-1}\boldsymbol{X}^T\boldsymbol{W}^{(k)}\boldsymbol{y}. \end{aligned} \tag{6.25}$$

The algorithm is initialized by setting $\boldsymbol{W}^{(0)}$ to the identity matrix. This is equivalent to obtaining the first guess for the parameters, $\boldsymbol{p}^{(1)}$, through a standard least squares fitting procedure by minimizing $\Gamma(\boldsymbol{p})$ in Eq. (6.19). The iterations in Eq. (6.25) continue until the minimizer $\mathcal{Z}$ defined in Eq. (6.23) converges to a specified tolerance, i.e., $\left|\mathcal{Z}(\boldsymbol{p}^{(k+1)}) - \mathcal{Z}(\boldsymbol{p}^{(k)})\right| < \text{tol}$. In our case, the tolerance was set to $\text{tol} = 10^{-10}$.

The IRLS method described above is used to obtain the parameters $\boldsymbol{p}$ for a given value of s. To obtain s, we minimize the l^2-norm of the residual,

$$\min_s \sqrt{\Gamma(\boldsymbol{p};s)} = \min_s \|\boldsymbol{y}-\boldsymbol{X}(s)\boldsymbol{p}(s)\|_2, \tag{6.26}$$

and obtain $\boldsymbol{p}(\tilde{s})$, where $\tilde{s}$ is the minimizer of Eq. (6.26).

6.3 Numerical results for the thermal parameters

The boundary-value problem described at the start of Section 6.2 of a silicon nanobeam with thermal BCs is solved using NEMD. The nanobeam is modeled as a collection of N atoms that interact via the three-body SW interatomic potential [115] with parameters for silicon archived in OpenKIM [121, 169, 170]. For details on NEMD simulations, see for example Ref. [84].

Temperature BCs were applied using either a Nosé-Hoover chain thermostat [88, 107, 109, 111] or a Langevin thermostat [100, 122] using a definition for temperature invariant with respect to rigid-body modes due to Jellinek and Li [93]. The parallel molecular dynamics code LAMMPS [123, 124] was used to integrate the equations of motion with modifications suggested by Singh and Tadmor [143].

All simulations begin with an initialization stage during which the system is equilibrated to the initial target temperature θ_0 and allowed to expand to its equilibrium volume. The silicon nanobeam has a diamond structure and is oriented so that the x, y and z axes coincide with the crystallographic [100], [010] and [001] directions. A nanobeam of size $n_x a_0 \times n_y a_0 \times n_z a_0$ (with $n_y = n_z$) is constructed where $a_0 = 5.43$ Å is the zero-temperature equilibrium constant for argon. Periodic BCs are applied in all directions, so during the initial phase the "nanobeam" is actually a bulk system. The initial momenta of all the atoms are selected from a Maxwell-Boltzmann distribution for twice the target temperature ($2\theta_0$). This is done because approximately half of the initial kinetic energy is transformed to potential energy due to the equipartition of energy, and so the final temperature after equilibration will be about half the original value and hence close to θ_0. After assigning the initial velocities, the nanobeam is evolved subject to NPT conditions with the pressure set to $P = 0$ and the temperature to $T = \theta_0$. A coupled Nosé-Hoover chain thermostat (chain length = 3) and barostat as described in Shinoda et al. [125] were used. The method is implemented within the LAMMPS code. The system is evolved for a total of 2×10^6 MD steps with a time step of $\Delta t_{\mathrm{MD}} = 2$ fs. Following the NPT simulation, the periodicity along z axis is removed, and (001) and $(00\bar{1})$ surfaces are exposed. An NVT simulation follows for 2×10^6 MD steps with the same time step in which only temperature is controlled to complete the initialization process. This is necessary to allow the surfaces to relax to their equilibrium structure at the target temperature.

We illustrate the TPI-IRLS method for a beam of size $33 \times 3 \times 3$ unit cells. After the initialization stage with $\theta_0 \approx 10$ K. The number of bins is set to $N_{\mathrm{bins}} = 11$ each containing 216 atoms. Next the temperature BCs in Eq. (6.12) are enforced by setting the temperatures of the leftmost and rightmost bins to $\theta_{\mathrm{L}} = \theta_{\mathrm{R}} = 30$ K using a Langevin thermostat with a damping time of 0.5 ps. The system is run for 2×10^5 MD steps with a time step of $\Delta t_{\mathrm{MD}} = 1$ fs. Thermal fluctuations are reduced by running the simulation ten times with different initial momenta drawn from a Maxwell-Boltzmann distribution for $\theta_{\mathrm{L}} = \theta_{\mathrm{R}} = 30$ K. $N_{\mathrm{profiles}} = 200$ temperature profiles are stored by taking averages of instantaneous values over $\Delta_t = 1$ ps. This temporal averaging ensures the existence of local thermodynamic equilibrium conditions [143]. Since we are interested in extracting the thermal parameters prior to the initiation of surface reconstruction, we only take the

first 15 profiles (i.e. we only take temperature data from the first 15 ps of the simulation before any reconstructions are observed to occur). These profiles are spline smoothed according to the procedure outlined in Section 6.2.1, where the parameters a_p, Δ_t and Δ_x in Eq. (6.13) are equal to 1, 1 ps and 16.29 Å, respectively.

We apply the IRLS method described in Section 6.2.2 and obtain the estimated coefficients $\boldsymbol{p}$ with components $p_1 = \tau_q$, $p_2 = k_0/\gamma$, and $p_3 = k_0\tau_\theta/\gamma$. Only positive values of these coefficients are considered. Using the estimated parameters, the continuum Jeffreys-type model in Eq. (6.10) is numerically solved by employing the finite difference discretization scheme described in the Appendix B. We calculate the root-mean-square deviation (RMSD) in temperature values between the continuum model and the atomistic data. We obtain different $\boldsymbol{p}$ values for different subsets of profiles such as $m \in [0, 3]$, $m \in [1, 3]$, and so on, and select the $\boldsymbol{p}$ values for which the RMSD value is minimum.

The volumetric heat capacity γ appearing in p_2 and p_3 is computed using a separate calculation. The entire beam is brought to steady state at $\theta = 20$ K with a Langevin thermostat for 2×10^6 MD steps with a time step size $\Delta t_{\mathrm{MD}} = 2$ fs. The beam continues to be thermostatted for another 3×10^5 MD steps and the energy of the beam is recorded at each MD step. Using Eq. (4.8) we find $\gamma = 1.40 \pm 0.10 \times 10^{-5}$ eV/(Å^3 K). Substituting γ into p_2 and p_3, the following results are obtained for the Jeffreys parameters for silicon, $s = -1.5 \pm 0.1$, $k_0 = 16.36 \pm 1.25$ W/mK, $\tau_q = 5.18 \pm 0.36$ ps, $\tau_\theta = 1.50 \pm 0.45$ ps. The error bars on the parameters are obtained using a statistical t-test procedure and all coefficients are estimated at a 5% statistical significance level [171]. The t-test provides the standard errors $\mathrm{SE_{p_1}}, \mathrm{SE_{p_2}}, \mathrm{SE_{p_3}}$, for the three components of the parameter vector $\boldsymbol{p}$. The standard errors of k_0, τ_q, τ_θ, i.e., $\mathrm{SE_{k_0}}, \mathrm{SE_{\tau_q}}, \mathrm{SE_{\tau_\theta}}$, are computed from $\mathrm{SE_{p_1}}, \mathrm{SE_{p_2}}, \mathrm{SE_{p_3}}$, γ and its standard deviation σ_γ using the following relations:

$$\begin{aligned} \mathrm{SE}_{\tau_\mathrm{q}} &= \mathrm{SE}_{\mathrm{p}_1}, \\ \frac{\mathrm{SE}_{\mathrm{k}0}^2}{k_0^2} &= \frac{\mathrm{SE}_{\mathrm{p}_2}^2}{p_2^2} + \frac{\sigma_\gamma^2}{\gamma^2}, \\ \frac{\mathrm{SE}_{\tau_\theta}^2}{\tau_\theta^2} &= \frac{\mathrm{SE}_{\mathrm{p}_3}^2}{p_3^2} + \frac{\mathrm{SE}_{\mathrm{p}_2}^2}{p_2^2}, \end{aligned} \tag{6.27}$$

which are derived based on the assumption that the covariance terms between p_2, p_3 and γ are zero.

The TPI-IRLS procedure was also applied to the CV model (Eq. (6.5)) and the

Fourier model (Eq. (6.3)) for the same size beam. We obtain $s = -1.9 \pm 0.1$, $k_0 = 24.85 \pm 1.63$ W/mK, $\tau_q = 2.42 \pm 0.20$ ps for the CV model and $s = -1.9 \pm 0.1$, $k_0 = 28.43 \pm 1.64$ W/mK, for the Fourier model. Figure 6.3 shows a comparison between the NEMD temperature profiles and the continuum profiles for the Fourier, CV and Jeffreys-type models.

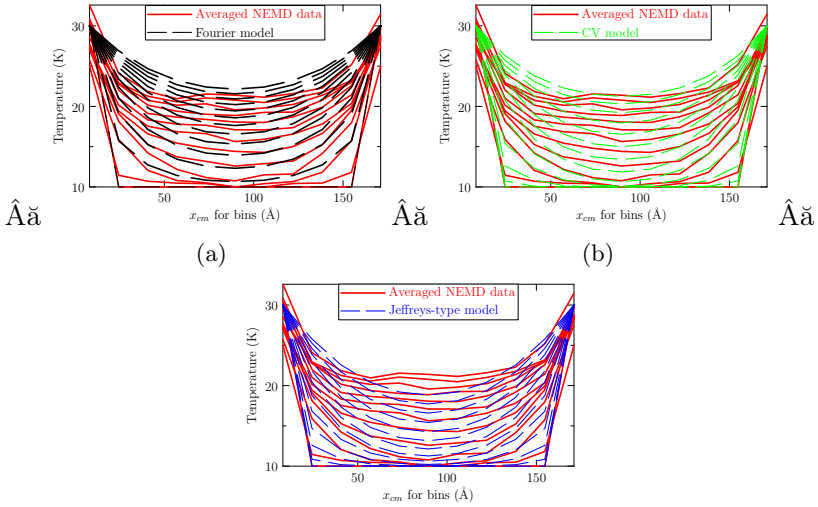

Figure 6.3: Comparison of the smoothed NEMD temperature profiles and the continuum models for (a) Fourier, (b) CV, and (c) Jeffreys-type thermal models for a silicon nanobeam of size $33 \times 3 \times 3$ unit cells prior to surface reconstruction. The initial beam temperature is $\theta_0 = 10$ K and the boundary temperatures are set to 30 K. Profiles are separated by 3 ps and each profile corresponds to an average of 1 ps of data. The zeroth profile is also shown.

Close examination of Fig. 6.3 and statistical testing reveal that the CV and the Jeffreys-type models are in better agreement with the NEMD data. In particular, the RMSD in temperature for the Fourier model is 2.41 as opposed to 2.03 for the Jeffreys-type model and 1.57 for the CV model. For systems with different sizes we obtain similar results. Thus we find that the CV model provides the best fit for the atomistic data for silicon nanobeams. We therefore choose the CV model for further analysis.[3] Results

[3] We also note that Jeffreys-type parameters obtained using the TPI-IRLS procedure are not unique, whereas they are for the Fourier and CV models. Unique Jeffreys-type parameters can be obtained by including heat flux profiles in the fitting procedure [143]. This is another reason why we have chosen CV over the Jeffreys-type model for the present work.

for the CV model for three different nanobeam sizes needed for the continuum-KMC calculations in Section 6.5.3 are given in Table 6.1.

Table 6.1: The CV parameters for three different nanoslab sizes along x-axis in unit cell. The size along the y and z axis is 3 unit cells. Values in parentheses are the standard errors of the parameters.

size	k_0 [W/mK]	τ_q [ps]	s
33	24.85 (1.63)	2.42 (0.20)	-1.9 (0.1)
63	33.38 (1.43)	4.29 (0.33)	-1.9 (0.1)
93	36.15 (1.34)	3.59 (0.68)	-1.9 (0.1)

In order to check the validity of the fitting scheme, we test whether the parameters obtained for one set of BCs can be used to describe a problem with different BCs. Figure 6.4 shows a comparison between atomistic NEMD data and the CV model for a different boundary-value problem with $\theta_{\mathrm{R}} = 30$ K and $\theta_{\mathrm{L}} = \theta_0 = 10$ K using the parameters obtained from the problem in Fig. 6.3(b). The agreement is quite good. This suggests that CV provides a good model for thermal transport in silicon nanobeams and is transferable to different loading conditions.

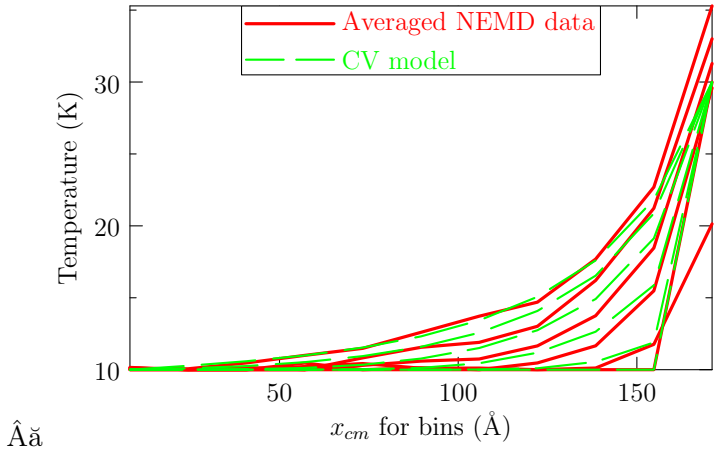

Âă Âă

Figure 6.4: Comparison of the NEMD temperature profiles with the predictions of the continuum CV model using the thermal parameters obtained from the temperature profiles in Fig. 6.3(b). The initial beam temperature is $\theta_0 = 10$ K and the temperature of the rightmost bin is increased to 30 K. In all simulations, NEMD profiles are an average of ten runs with different initial momenta. Except for the zeroth profile, each profile is an average of 1 ps of data.

6.4 Surface Reconstruction

In the fitting process described in Section 6.3, temperature profiles from only the first 15 ps were used (see Fig. 6.3 and accompanying discussion). This is because at later times the surfaces of the nanobeam begin to reconstruct as the temperature rises. In this section we explore the energetics of the reconstruction process of an exposed (001) surface in a vacuum. We start with an ideal unreconstructed (001) surface as shown in Fig. 6.5(a). The rows of dangling bonds, which are clearly visible in the figure, are less energetically favorable than the reconstructed states described below. For the SW potential, we find that dangling bonds on the surface rotate to form dimers along the $[\bar{1}10]$ direction as shown in Fig. 6.5(b) (3D view) and Fig. 6.5(c) (plan view). This reconstruction is different from the experimentally observed structures discussed in the beginning of this chapter. Rather than the commonly observed $p(2 \times 1)$ reconstruction, the SW potential predicts a structure consisting of rows of dimers along the $[\bar{1}10]$ direction separated by a row of dangling bonds. We refer to this as the *symmetric* $p(3 \times 1)$ reconstruction. For the SW potential, the symmetric $p(2 \times 1)$ and symmetric $p(3 \times 1)$ structures have surface energies of 246.4 meV/Å^2 and 259.3 meV/Å^2, respectively. This means that the $p(2 \times 1)$ structure is more favorable than the $p(3 \times 1)$. However, as we show below, a small energy barrier exists for the formation of dimers. For SW, this barrier is a little higher for creating an adjacent dimer in the $p(2 \times 1)$ structure (22.5 meV) than for creating a dimer separated by a row of dangling bonds in the $p(3 \times 1)$ structure (20.8 meV). This difference is the reason that the SW potential favors the $p(3 \times 1)$ structure at low temperature. At higher temperatures, the system has more energy to overcome energy barriers and can more fully explore its configuration space. Due to entropic effects, a mixture of $p(2 \times 1)$ and $p(3 \times 1)$ structures is observed, with the fraction of $p(2 \times 1)$ increasing with temperature. This is clear in Figs. 6.5(d) and 6.5(e) that show the reconstructed surfaces predicted by SW at at 300 K and 1100 K. The high temperature results are in agreement with other molecular dynamics simulations using the SW potential [172, 173].

The fact that dimerization is not observed at very low temperatures (over the duration of an NEMD simulation) but does occur at elevated temperature, suggests that it

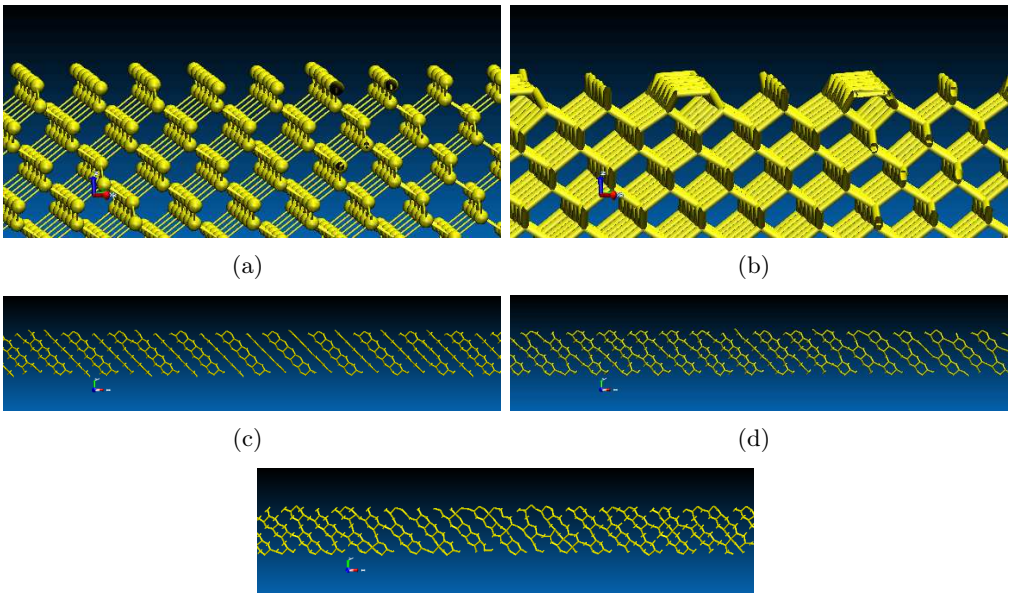

Figure 6.5: (a) 3D view of the ideal unreconstructed (001) surface, and (b) the reconstructed surface at 30 K of the silicon nanobeam of size $33 \times 3 \times 3$ unit cells. The top layer of the reconstructed (001) surface seen from above at (c) 30 K, (d) 300 K, (e) 1100 K.

is an activated process. The h-TST transition rate R for dimer formation is

$$R = \nu_d \exp\left(-\Delta E_b / k_{\mathrm{B}}\theta\right), \tag{6.28}$$

where ν_d is the attempt frequency, θ is the local temperature, k_{B} is Boltzmann's constant, and ΔE_b is the energy barrier separating the undimerized and dimerized states.

We use the CI-NEB method of Henkelman et al. [58] to obtain the energy barrier ΔE_b and the energy released during dimerization ΔE_r. We start with a nanobeam of size $33 \times 3 \times 3$ unit cells equilibrated at 10 K as discussed in Section 6.3 and focus on a single bin along the $[\bar{1}10]$ direction. Taking the ideal unreconstructed (001) surface as the first configuration C1, we displace the two atoms in the front towards each other by 0.13 Å and minimize the total energy to obtain the second configuration C2 with one dimer formed. We repeat the process for the next two atoms in the row to obtain the third configuration C3 with two dimers formed, and so on to obtain configurations C4 and C5 as shown in Fig. 6.6. Our intention in creating this sequence of configurations is to

see whether the barrier and energy release for dimer formation is affected by previously formed dimers in the vicinity. We apply the CI-NEB procedure with C1 as the initial state and C2 as the final state with a total of 16 replicas along the band generated by linear interpolation. We repeat the process for C2 and C3, and so on. Figure 6.6(f) presents the energy along the minimum energy path for the resulting series of transitions. We find that the energy barrier ΔE_b for the first dimer formation is approximately 22 meV and the energy released during this process is $\Delta E_r \approx 1.65$ eV. The energy barrier and energy released in all subsequent dimerizations is about the same with $\Delta E_b \approx 6.8$ meV and $\Delta E_r \approx 1.71$ eV. It is noteworthy that the barrier for the first dimerization is about three times higher than for subsequent dimerizations. Thus it is easier to dimerize after the process begins.

Instead of the process described above where all dimers form in a single row, it is also possible for dimers to form in alternate rows. A corresponding series of configurations C1–C2–C3′–C4′–C5′ for this alternate process are shown in Fig. 6.7 (configurations C1 and C2 are the same ones shown in Figs. 6.6(a) and 6.6(b)). The energy along the corresponding minimum energy path obtained by CI-NEB is shown in Fig. 6.7(d). Three types of transitions are observed in this process:

Type I The first dimer formed on an ideal surface (C1–C2) has $\Delta E_b = 22$ meV and $\Delta E_r = 1.65$ eV (as also reported in Fig. 6.6).

Type II A dimer formed on an alternate row to an adjacent one (C2–C3′ and C3′–C4′) has $\Delta E_b = 33$ meV and $\Delta E_r = 1.61$ eV.

Type III A dimer formed on the same row as an adjacent dimer (C4′–C5′) has $\Delta E_b = 6.8$ meV and $\Delta E_r = 1.71$ eV (as also reported in Fig. 6.6(f)).

These results indicate that dimer formation is easiest along the same row. The energy barrier for alternate dimerization is more than four times higher. In addition to the above, CI-NEB calculations were carried out for several other systems with free (001) surfaces for different system sizes ($3\times3\times4, 6\times6\times4, 33\times4\times4$, and others) and different dimer configurations. In all cases, only Type I, II and III transitions were observed.

We calculated the attempt frequency ν_d appearing in Eq. (6.28) using the Vineyard

equation [174]:

$$\nu_d = \frac{\prod_{j=1}^{3N} \nu_j}{\prod_{j=1}^{3N-1} \nu_j^{\ddagger}} \tag{6.29}$$

where ν and $\nu^{\ddagger}$ are normal frequencies of vibration at the initial and saddle point states, respectively, and N is the total number of atoms in the system. We find $\nu_d = 50.1$, 1.5, and 0.16 ps^{-1} for Type I, II and III transitions, respectively. These numbers are comparable to the values found by other workers [175, 176].

6.5 Hybrid continuum-KMC model

In this section we describe the hybrid continuum-KMC method developed to model the heating of a nanobeam due to surface reconstruction.

6.5.1 The continuum model

In Section 6.3, we demonstrated that the continuum CV model in Eq. (6.5) provides a good description of temperature evolution in silicon nanobeams. However, a stochastic source term $r(\boldsymbol{x}, t)$ must be added to the energy equation in Eq. (6.30) to model the latent heat released per unit time during the dimerization process:[4]

$$\frac{\partial e}{\partial t} = -\frac{\partial q}{\partial x} + r. \tag{6.30}$$

Using the constitutive CV model for the heat flux in Eq. (6.4), the energy equation in Eq. (6.30) and the thermal conductivity k in Eq. (6.9), yields the CV wave equation with a source term:

$$\frac{\partial \theta}{\partial t} = -\tau_q \frac{\partial^2 \theta}{\partial t^2} + \frac{k_0}{\gamma}\left[\left(\frac{\theta}{\theta_0}\right)^s \left(\frac{s}{\theta}\left(\frac{\partial \theta}{\partial x}\right)^2 + \frac{\partial^2 \theta}{\partial x^2}\right)\right] + r/\gamma. \tag{6.31}$$

To simplify the model, we assume that the thermal conductivity k becomes constant for

[4] See for example Section 10.2 in Ref. [1].

temperatures exceeding the boundary values:[5]

$$k(\theta) = \begin{cases} k_0\big(\theta/\theta_0\big)^s, & \text{if } \theta \le \theta_L, \\ k(\theta = \theta_L), & \text{otherwise,} \end{cases} \tag{6.32}$$

where k_0 is the thermal conductivity at initial temperature θ_0, s is a real exponent and θ_L is the boundary temperature. We choose the value of τ_q obtained from the TPI-IRLS method described in Section 6.3.

We employ the explicit 1D finite difference discretization schemes described in the appendix to numerically solve the PDE in Eq. (6.31). The spatial grid size is taken equal to the bin size in the NEMD simulations, so that the continuum grid points along the x-axis are located at x_n ($n = 1, \ldots, N_{\text{bins}}$) (the geometric centers of the NEMD bins) as defined in Section 6.2. The discretization time step is taken to be $\Delta t = 0.001$ ps to ensure that the explicit scheme satisfies the Courant-Friedrichs-Lewy condition [177] for numerical stability.[6]

The heat source term $r = r(\boldsymbol{x}, t)$ appearing in Eq. (6.31) accounts for the latent heat that is released whenever a dimer is formed. A dimerization event at position x_n ($n = 2, \ldots, N_{\text{bins}} - 1$) and time t is modeled as a uniform heat pulse of duration Δt_R. Thus over the time interval $[t, t + t_R]$, we have

$$r(x_n, t) = \dot{Q}_e, \tag{6.33}$$

where $\dot{Q}_e$ is the energy released per unit volume per unit time. Since the volume associated with a grid point is V_{bin} (volume of a bin) and a dimerization event releases ΔE_r energy, we have

$$\dot{Q}_e = \frac{1}{V_{\text{bin}}} \frac{\Delta E_r}{\Delta t_R}. \tag{6.34}$$

[5] Adopting a temperature-dependent thermal conductivity as in Eq. (6.9) beyond the boundary temperatures requires the thermal parameter extraction process described in Section 6.2 to be done for temperatures exceeding 30 K. This means taking into account the surface reconstruction process and would require a significant modification to the TPI-IRLS method. Moreover, it becomes difficult to handle the PDE with temperature dependent thermal conductivity due to the instabilities introduced by the presence of the stochastic term. In addition, the highly nonequilibrium nature of latent heat release leads to large sudden changes in the temperature gradients. This suggest the need for a *nonlocal* dependence of thermal conductivity on the temperature gradient field [54, 145]. For these reasons, we have opted to use a simple constant thermal conductivity in this analysis for temperatures above the boundary temperature, reserving more complex models for future work.

[6] The time step violating the CFL condition for all cases in the present work is greater than 0.1 ps.

The energy ΔE_r for the dimerization types being considered is given in Section 6.4.

We estimate the time interval Δt_R over which the latent heat energy is absorbed in a bin based on the following heuristic argument. Consider a constant heat source $\dot{Q}_e$ located at the origin of an infinite medium. Assuming Fourier's model, the axisymmetric temperature field at a radial distance ξ is given by [178]

$$\theta(\xi, t) = \frac{\dot{Q}_e}{4\pi k \xi} \text{erfc}\left(\frac{\xi}{\sqrt{4\alpha t}}\right), \tag{6.35}$$

where $\alpha = k/\gamma$ is the thermal diffusivity and erfc is the error function. We identify Δt_R with the time at which the temperature reaches 90% of its steady-state value at $\xi = \Delta_x/2$ corresponding to the distance from a heat source at a bin center to its edges, i.e.

$$\begin{aligned} \theta(\Delta_x/2, \Delta t_R) &= 0.9 \lim_{t\to\infty} \theta(\Delta_x/2, t), \\ \implies \text{erfc}\left(\frac{\Delta_x/2}{\sqrt{4\alpha \Delta t_R}}\right) &= 0.9. \end{aligned} \tag{6.36}$$

The interval Δt_R is an estimate for the time that a localized heat pulse generated by a dimerization event is uniformly distributed across the enclosing bin. For a nanobeam of size $33 \times 3 \times 3$ unit cells, $\Delta_x = 3a_0 = 16.29$ Å. The thermal diffusivity for a nanobeam of this size follows from the results of Section 6.3 as $\alpha = k/\gamma = 157.18$ Å^2 ps, where $k = k_0(\theta/\theta_0)^s = 28.43(30/10)^{-1.9} = 3.53$ W/mK and $\gamma = 1.40 \times 10^{-5}$ eV/(Å^3 K). Using these values in Eq. (6.36), we obtain $\Delta t_R = 0.08$ ps. The value of Δt_R depends on the nanobeam size because thermal conductivity is size dependent. For systems of size $63 \times 3 \times 3$ and $93 \times 3 \times 3$, we find $\Delta t_R = 0.06$ and 0.05 ps, respectively.

The numerical formulation for solving the PDE is now complete except for the determination of the dimerization events. This is a stochastic process that we model using the KMC algorithm described in the next section.

6.5.2 The KMC method and the algorithm

The source term $r(\boldsymbol{x}, t)$ in Eq. (6.31) represents dimerization events on the surfaces of a nanobeam that inject heat pulses into the system. Since dimerization is a random activated process, we use a stochastic KMC algorithm to determine the locations and waiting times for dimerization events.

In the KMC method, a catalog (rate table) of all possible events is prepared at a given time. In our case, the events correspond to the formation of dimers at grid points associated with internal bin centers ($n = 2, \ldots, N_{\text{bins}} - 1$). We make several assumptions to simplify the formulation and make it computationally tractable:

1. Each grid point is associated with a bin in the original NEMD simulation and therefore has a finite number of possible dimerizations $d_{\max}$, which depends on the top and bottom bin surface area. In the simulations reported below the bin surfaces are 3×3 unit cells, for which $d_{\max} = 12$ on average. Once all 12 dimers are formed, further dimerization is not possible in that bin.

2. The first dimer on the upper and lower (001) surfaces of each bin has to be of Type I as described in Section 6.4. Once a type I dimer forms, a maximum of five dimers of either Type II or Type III can form on that surface. However, to simplify the formulation we require two Type I dimers to form first, and then ten dimers of either Type II or Type III can be formed.

3. Only one grid point can undergo dimerization at a time. This greatly reduces the computational intensity of the KMC computations. This is a reasonable approximation since dimerization events are independent and the probability of two or more dimers forming simultaneously is negligible in comparison to single dimer formation. This is an important assumption since it reduces the number of events to $O(N_{\text{bins}})$ making the calculation tractable.

A continuum-KMC formulation consistent with the above assumptions is given in Algorithm 1. Between dimerization events, the PDE in Eq. (6.31) is integrated without a source term. When a dimerization event occurs the PDE is integrated for a period Δt_R (computed in the previous section) with the constant source term $\dot{Q}_e$ given in Eq. (6.34). The dimerization events and the times they occur are determined using a KMC algorithm for time-dependent transition rates due to Prados et al.[179]. (A time-dependent algorithm must be used because the temperature along the nanobeam is changing during the KMC process and hence the rates are changing.) The average waiting time Δt_{KMC} between events is obtained by solving

$$\int_0^{\Delta t_{\text{KMC}}} R_{\text{tot}}(t')dt' \leq -\ln u, \tag{6.37}$$

where u is a uniform random number in the range $[0,1]$, $R_{\text{tot}}(t) = \sum_{i=1}^{N_p} R_i(t)$ is the total transition rate at time t, N_p is the number of events (all possible dimerization events at all grid points that can occur during the time interval Δt_{KMC}), and R_i $(i = 1, \ldots, N_p)$ are the rates for forming the dimers. We assume that at each grid point two dimers of Type I form first (one on the top surface and one on the bottom) followed by ten dimers of either Type II or III.[7] Thus the number of dimers d_n at grid point n ranges from 0 to 12. The rate R_i for an event occurring at grid point x_n is computed from Eq. (6.28) with $\theta = \theta_n(t)$, and the attempt frequency ν_d and activation barrier ΔE_b for a Type I, Type II, Type III dimer given in Section 6.4. Once the time to the next event Δt_{KMC} has been obtained by solving Eq. (6.37), the rate table at that time is constructed and the event that happens is randomly selected in standard KMC fashion as described in Algorithm 1. Once all dimerization sites are exhausted, the KMC algorithm is no longer applied and the PDE in Eq. (6.31) is integrated without a source term from then on.

6.5.3 Numerical results

We now revisit the problem described in the beginning of this chapter and the results shown in Fig. 6.1. A silicon nanobeam with exposed $\{001\}$ surfaces is equilibrated at 10 K and then its ends are heated to 30 K and maintained at this temperature as a fixed thermal BC. As the temperature of the interior begins to rise, dimerization events begin to occur that due to the latent heat released cause the nanobeam temperature in the center to dramatically overshoot the BC temperature.

In this section, we simulated this problem using the continuum-KMC model outlined in Algorithm 1 using the thermal parameters for the CV model obtained using the TPI-IRLS method described in Section 6.3. Three different nanobeam sizes are studied: $33 \times 3 \times 3$, $63 \times 3 \times 3$, and $93 \times 3 \times 3$. The models contain 2574, 4914 and 7254 atoms respectively. NEMD simulations were carried out on a parallel cluster using LAMMPS with 24 cores. Simulation times for the three systems were 2.2, 4.5 and 8 hours, respectively. The continuum-KMC calculations were carried out using the CV

[7] This is clearly an approximation. A more accurate approach would track the topology of dimer formation on the surface and include all possible events. (For example Type II dimers should only form adjacent to Type I dimers, and more than two Type I dimers can in principle form.) However this would greatly increase the complexity of the code and its computational expense and it was felt that the simpler more approximate approach was consistent with the overall level of accuracy of the model.

parameters given in Table 6.1. The results comparing the NEMD profiles (red) and continuum-KMC predictions (blue) are shown in Fig. 6.8. (Note that the results shown in Fig. 6.1, correspond to Fig. 6.8(c) here.) The plots show a series of temperature profiles at increasing time. Clearly the continuum-KMC results are in good overall agreement with the NEMD results, correctly capturing the thermal overshooting. Although not apparent in the figure, the temperature first rises to reach the maximum temperature profile and then cools down to the BC temperature of 30 K as heat is dissipated through the thermostatted ends. The times it takes the nanobeams to reach the maximum temperature profile and then cool back down to the BC temperature are: 110 ps/300 ps ($33 \times 3 \times 3$), 220 ps/600 ps ($63 \times 3 \times 3$), and 234 ps/900 ps ($93 \times 3 \times 3$). These times may be sensitive to the damping parameter used in the thermostatted bins at the ends of the nanobeam.

Having established the validity of the continuum-KMC model for smaller system sizes it is of interest to explore its predictions for larger systems that are difficult to simulate using NEMD due to the computational cost. Figure 6.9 shows the results for a nanobeam of length 603 unit cells (0.327 μm). The CV parameters were estimated as $k_0 = 303.13$ W/mK, $\tau_q = 6.11$ ps, $s = -1.9$. The dimer latent heat absorption time is taken to be $\Delta t_R = 0.0065$ ps. The thermal overshooting in this case is even more significant.

In general, we find that the degree of overshooting, characterized by the maximum temperature along the beam,

$$\theta_{\max} = \max\{\theta(x,t) | 0 \le x \le L, 0 \le t < \infty\}, \tag{6.38}$$

increases with increasing nanobeam length L as shown in Fig. 6.10(a). The same data is plotted on a semi-log plot in Fig. 6.10(b). A linear fit of the form,

$$\theta_{\max}(L) = a \ln L - b, \tag{6.39}$$

where $a = 75.91 \pm 3.79$ K/ln nm, $b = 1.93 \pm 1.07$ K with $\theta_{\max}$ in K and L in nm provides a good fit to the data above a length of 123 unit cells ($L = 123 \times 0.543 = 66.8$ nm). The deviation from the logarithmic fit can be understood by considering the length-dependence of the thermal conductivity and time lag shown in Figs. 6.11(a) and 6.11(b). Above about 123 unit cells ($1/L = 0.015$ nm^{-1}), the dependence of thermal conductivity

k_0 on length L takes the following form [54, 117]:

$$\frac{1}{k_0} = \frac{1}{k_\infty} + \frac{c}{L}, \tag{6.40}$$

where c is a constant and k_∞ is the bulk value at 10 K. Below 123 unit cells the fit breaks down, which explains the deviation seen in Fig. 6.10(b). Fitting the data in in Fig. 6.11(a) to the relation in Eq. (6.40), yields $k_\infty = 2676.70 \pm 124.84$ W/mK, which is close to the experimental result of Thompson and Younglove [180]. The dependence of τ_q on L takes a similar form [117, 143]:

$$\frac{1}{\tau_q} = \frac{1}{\tau_\infty} + \frac{c_\tau}{L}, \tag{6.41}$$

were c_τ is a constant dependent on the thermostat parameters.[54] Fitting to the data in Fig. 6.11(b), we find that the bulk value τ_∞ is 8.67 ± 0.37 ps.

The logarithmic divergence of the overshooting temperature with nanobeam length seen in Fig. 6.10 can be understood from an analysis of the spatially non-dimensionalized form of Eq. (6.31),

$$\frac{\partial\theta}{\partial t} = -\tau_q \frac{\partial^2\theta}{\partial t^2} + \frac{k_0(L)}{\gamma L^2}\left[\left(\frac{\theta}{\theta_0}\right)^s \left(\frac{s}{\theta}\left(\frac{\partial\theta}{\partial x'}\right)^2 + \frac{\partial^2\theta}{\partial x'^2}\right)\right] + r'/\gamma, \tag{6.42}$$

where $x' = x/L$, and $r'(x', t)$ is the dimensionless source term. As the length of the nanobeam increases, the diffusion term coefficient $k_0(L)/\gamma L^2$ tends to zero. The wave term does not play an important role due to the small value of τ_q in this system. As a result heat is transported at a slower rate as the nanobeam length increases. At the same time, the source term $r'(x', t)$ tends to infinity as the number density of surface dimerization sites increase over the unit length. Basically as the length of the nanobeam increase more heat is generated and the ability of the nanobeam to diffuse the heat away decreases. This trend will continue until the maximum temperature reaches the melting point. From Eq. (6.39) and the melting point of Si ($\theta_\mathrm{m} \approx 1700$ K), the length required for this to happen is about 5.45 m.

6.6 Summary

Silicon nanobeams with free {001} surfaces undergo a surface reconstruction process in NEMD simulations. This involves dimer formation along ⟨110⟩ directions on the exposed

surfaces resulting in the release of latent heat, which can lead to a significant increase in the temperature. For example, NEMD simulations using the SW potential show that a silicon nanobeam of size $505 \times 16.3 \times 16.3$ Å that is initially at 10 K and then heated at the ends to 30 K, exhibits thermal overshooting reaching above 200 K at its center. The overshooting temperature diverges logarithmically with beam length until the melting temperature is reached.

A hybrid continuum-KMC method is proposed to model the thermal overshooting behavior. In this method, thermal transport is modeled using a non-Fourier continuum model in which heat propagates as a wave with a finite velocity. (This is in contrast to Fourier's model that predicts diffusive heat transfer with infinite propagation speed). In the first part of the chapter, non-Fourier thermal parameters are obtained from NEMD simulations with the SW potential using a novel TPI-IRLS regression method. Results for the non-Fourier CV and Jeffreys-type models, as well as for Fourier's model, for different nanobeam sizes are given in Section 6.3. Based on these results, it is determined that the CV model is best able to capture thermal transport observed in NEMD simulations of silicon nanobeams.

In the second part of the chapter, the CV wave equation is augmented with a source term to account for the energy injected into the system by the latent heat released during dimer formation accompanying surface reconstruction. The dimerization process is stochastic and is modeled using a KMC algorithm for time-dependent transition rates that is coupled to the continuum CV equation. The rates needed for the KMC algorithm are estimated using h-TST with activation barriers obtained using CI-NEB and attempt frequencies computed using Vineyard's equation. The resulting continuum-KMC method is described in Algorithm 1. The predictions of the method are found to be in good agreement with the NEMD simulation results mentioned above that show dramatic thermal overshooting.

Although the phenomenon observed here is somewhat academic since it is predicted to occur for silicon at very low temperatures in a vacuum, it can have technological applications for other material systems where reconstructions occur at higher temperatures under ambient conditions. For example, Zheng et al [181] observed superheating of Cu_2S nanorods due to phase transformations from a low-chalcocite to a high-chalcocite phase induced by electron beam heating. The TPI-IRLS and continuum-KMC methods

described in this chapter can be applied to this problem and to an entire class of physical phenomena of similar nature. These are promising areas for future research.

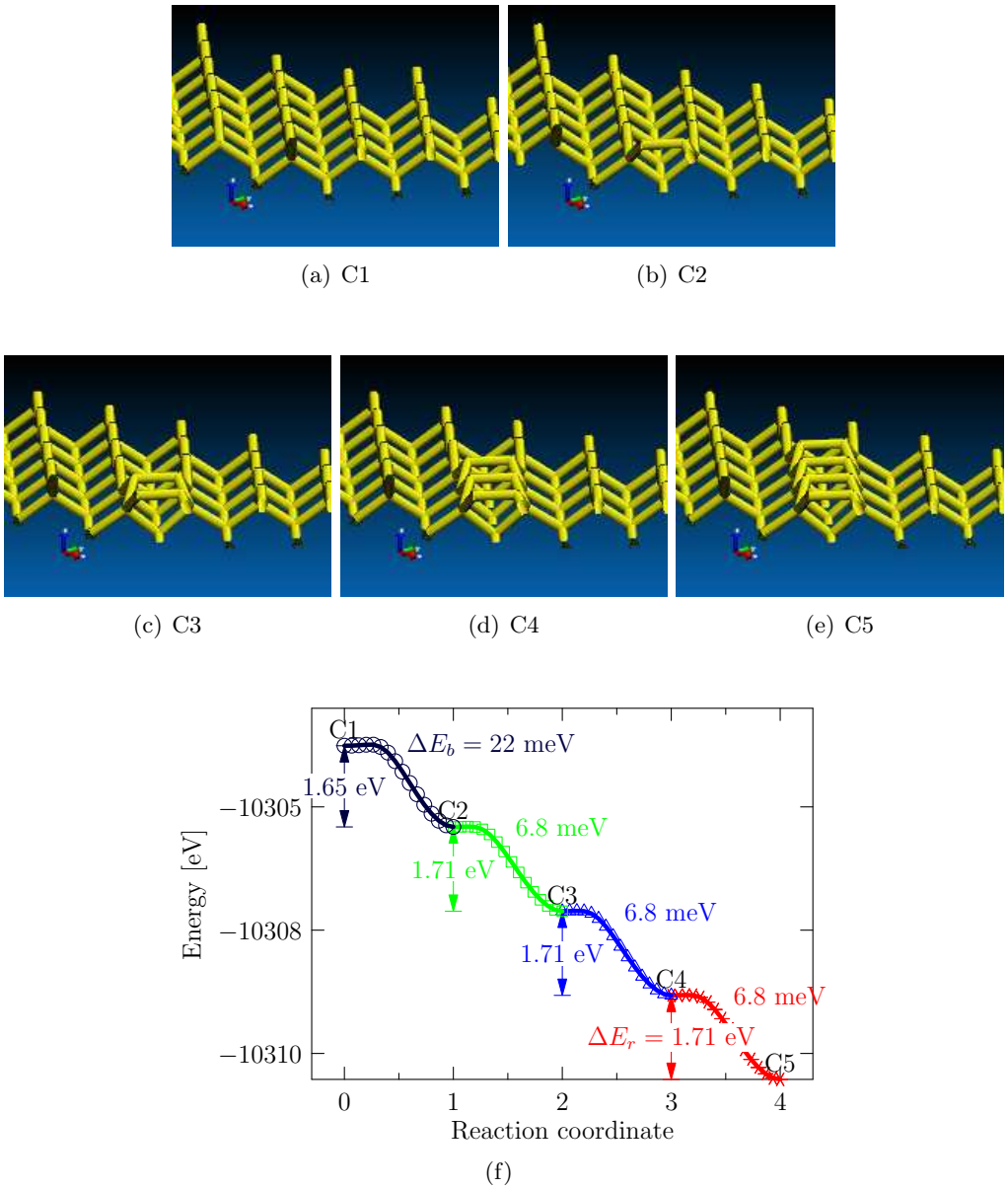

Figure 6.6: (a) Configuration C1 associated with the unreconstructed (001) surface, (b)–(e) configurations C2, C3, C4 and C5 with one, two, three and four dimers, respectively, and (f) the minimum energy path for the series of transitions from C1 to C5 indicated by different colors. The number on the left of each curve is the energy released ΔE_r and the number on the right is the energy barrier ΔE_b.

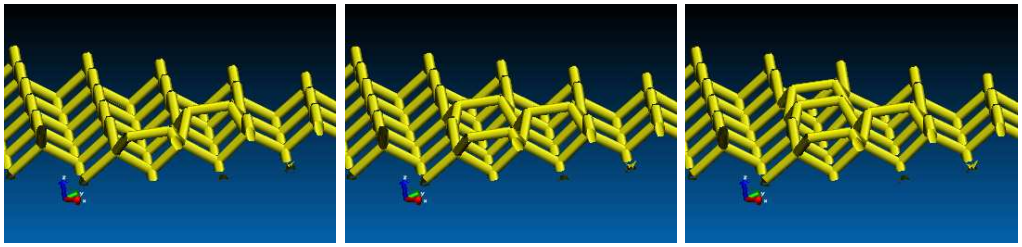

(a) C3′ (b) C4′ (c) C5′

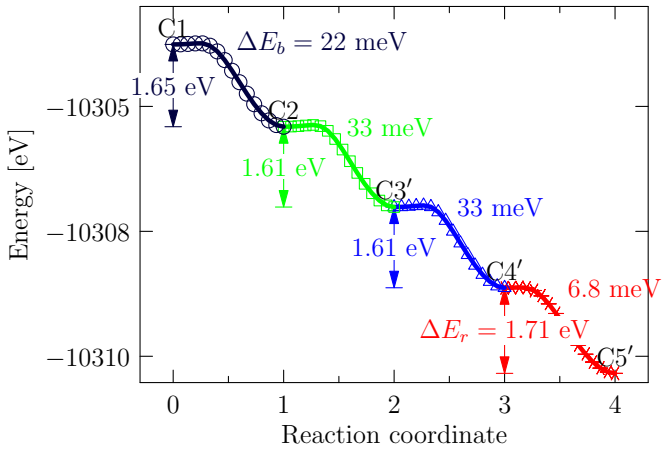

(d)

Figure 6.7: (a)–(c) show the configurations C3′, C4′, and C5′ with two, three and four dimers along two adjacent rows, and (d) The minimum energy path for C1–C5′ transition. The black, green, blue and red curves are the minimum energy paths for C1–C2, C2–C3′, C3′–C4′ and C4′–C5′ transitions. The numbers to the left of each curve is the energy released ΔE_r and the number to the right is the energy barrier ΔE_b.

Algorithm 1 Continuum-KMC method for nanobeam temperature evolution in the presence of surface reconstructions.

$t := 0$
$d_n := 0$ $(n = 2, \ldots, N_{\text{bins}})$
$dimers\_exhausted :=$ false
while $t < t_{\text{final}}$ **do**
  $u :=$ uniform random number $\in [0, 1]$
  $\Delta t_{\text{KMC}} := 0$
  $I := 0$ [I is the left-hand side of Eq. (6.37)]
  while $I \leq -\ln u$ & $dimers\_exhausted =$ false **do**
    Construct rate table:
    $N_p := 0$
    for $n = 2$ to N_{bins} **do**
      if $d_n < 2$ **then**
        Add to rate table $2 - d_n$ rates for Type I dimer
        $N_p := N_p + 2 - d_n$
      else if $d_n < d_{\max}$ **then**
        Add to rate table $d_{\max} - d_n$ rates for Type II dimers
        Add to rate table $d_{\max} - d_n$ rates for Type III dimers
        $N_p := N_p + 2(d_{\max} - d_n)$
      end if
    end for
    if $N_p \neq 0$ **then**
      Compute rates $R_i (i = 1, \ldots, N_p)$
      $R_{\text{tot}} := \sum_{i=1}^{N_p} R_i$
      $I := I + R_{\text{tot}}\, \Delta t$
      Integrate the PDE in Eq. (6.31) for one discretization time step with zero source term
      $t := t + \Delta t$
      $\Delta t_{\text{KMC}} := \Delta t_{\text{KMC}} + \Delta t$
    else
      $dimers\_exhausted :=$ true
    end if
  end while
  if $dimers\_exhausted =$ false **then**
    $\widetilde{R}_i := \sum_{j=1}^{i} R_j$
    u := uniform random number $\in [0, 1]$
    Select event i for which $\widetilde{R}_{i-1} < u\widetilde{R}_{N_p} \leq \widetilde{R}_i$
    $d_n := d_n + 1$ [where n is bin associated with event i]
    Integrate the PDE in Eq. (6.31) for Δt_R time with constant heat source $\dot{Q}_e$ given in Eq. (6.34)
    $t := t + \Delta t_R$
  else
    Integrate the PDE in Eq. (6.31) for one discretization time step with zero source term
    $t := t + \Delta t$
  end if
end while

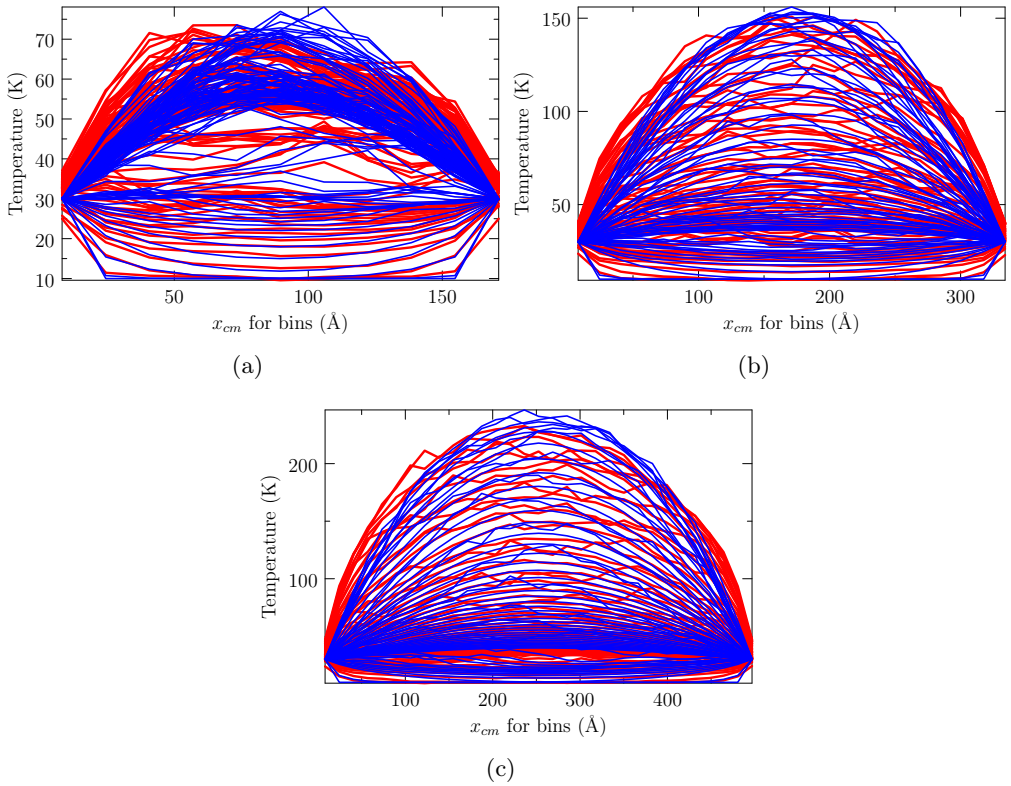

Figure 6.8: Comparison of the NEMD temperature profiles (red) with the predictions of a hybrid continuum-KMC CV model (blue) for silicon nanobeams of size (a) $33 \times 3 \times 3$, (b) $63 \times 3 \times 3$, and (c) $93 \times 3 \times 3$ unit cells with free (001) surfaces. The initial beam temperature is $\theta_0 = 10$ K and the boundary temperatures are set to 30 K. In all simulations, NEMD profiles are averaged over ten different initial momenta distribution. The hybrid continuum-KMC profiles are averaged over five simulations with different seeds for the pseudo random number generator used by the KMC calculations. Each profile is an average of 1 ps 2 ps and 3 ps of data for three different sizes, respectively. For the sake of clarity every alternate profile for case (a), every two consecutive profiles for case (b) and (c) have been omitted.

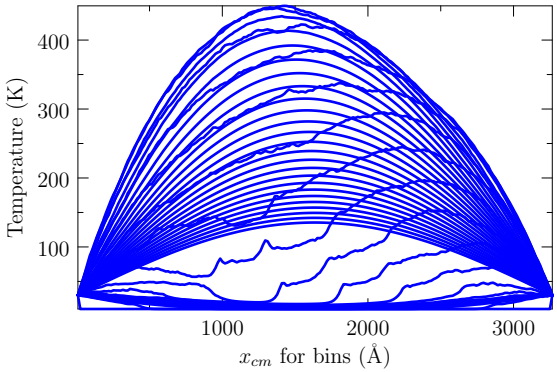

Figure 6.9: Hybrid continuum-KMC temperature profiles for a silicon nanobeam of size $603 \times 3 \times 3$ unit cells when the initial temperature $\theta_0 = 10$ K and the boundary temperatures were raised to $\theta_L = \theta_R = 30$ K. The thermal parameters are $k_0 = 303.13$ W/mK, $\tau_q = 6.11$ ps, $s = -1.9$, and $\Delta t_R = 0.0065$ ps.

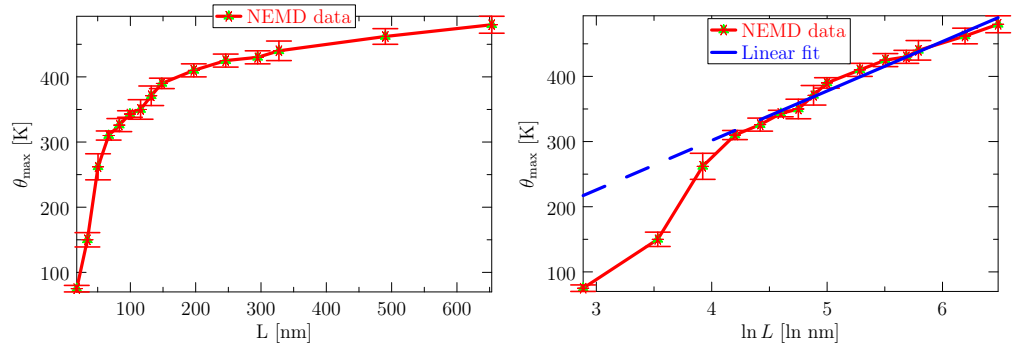

Figure 6.10: (a) Plot of $\theta_{\max}$ versus L. The maximum value for a given length is obtained by averaging over ten different ensembles. The error bars are the standard deviations in the bin temperature over these ensembles. (b) Plot of $\theta_{\max}$ versus the natural log of L. The data for lengths smaller than 123 unit cells ($\ln L = 4.2$, where $L = 123 \times 0.543 = 66.8$ nm) were not included in the curve fitting. The dashed line shows the extension of the fit to smaller lengths.

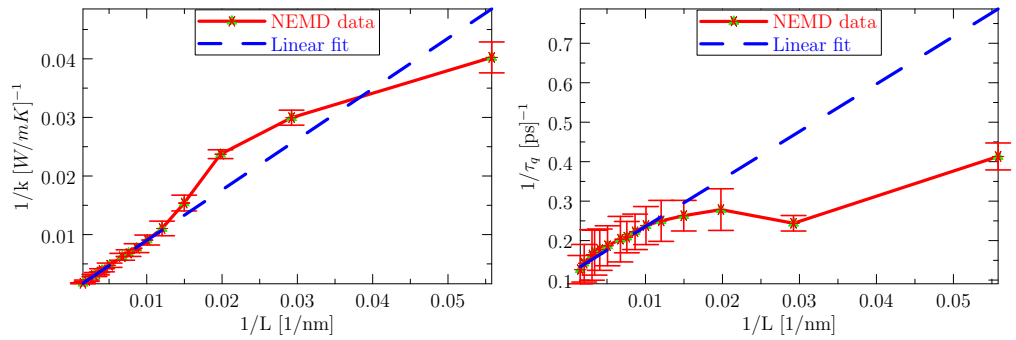

Figure 6.11: Plots of (a) $1/k_0$ versus $1/L$, (b) $1/\tau_q$ versus $1/L$, where data for lengths smaller than 123 unit cells ($1/L > 0.015$ nm^{-1}) are not included in the linear fit.

Chapter 7

Conclusion

A new simple TPI method has been proposed for extracting the thermal non-Fourier (Jeffreys-type) parameters k, τ_θ and τ_q from a sequence of NEMD temperature and heat-flux profiles. An initial sinusoidal temperature distribution is applied using thermostats to a nanobeam. The thermostat are then removed, and the nanobeam temperature decays to a constant average value under constant energy conditions. The thermal parameters are obtained by fitting analytical solutions for scalars obtained as cosine and sine-averages of the temperature and heat flux, respectively, to the NEMD data during the decay process. We apply the method on the argon nanobeams and we find that a Jeffreys-type model with three parameters was better able to reproduce NEMD temperature profiles in thermal problems than a simple Fourier model. This was demonstrated by performing an NEMD simulation of the spreading of a heat pulse applied to the center of a nanobeam.

Then we suggest a modification in NEMD direct method to reduce the artificial Kapitza resistance at the interfaces between the thermostatted and unthermostatted regions. We propose linear and nonlinear phenomenological models to account for the dependence of the thermal conductivity on variables such as length of the beam and damping parameters of the thermostat. The main advantage of the approach is that by explicitly accounting for the thermostat parameters, good results can be obtained with smaller system sizes than needed to obtain converged results with the standard direct NEMD approach.

A hybrid continuum-KMC method is proposed to model the thermal overshooting

behavior in silicon nanobeams with free {001} surfaces. In this method, thermal transport is modeled using a non-Fourier continuum model in which heat propagates as a wave with a finite velocity. The non-Fourier thermal parameters are obtained from NEMD simulations with the SW potential using a novel TPI-IRLS regression method. Based on the results of this method, it is determined that the CV model is best able to capture thermal transport observed in NEMD simulations of silicon nanobeams. This CV wave equation is augmented with a source term to account for the energy injected into the system by the latent heat released during the dimer formation accompanying surface reconstruction. The dimerization process is stochastic and is modeled using a KMC algorithm that is coupled to the continuum CV equation. The rates needed for the KMC algorithm are estimated using h-TST with activation barriers obtained using CI-NEB and attempt frequencies computed using Vineyard's equation. Although the phenomenon observed here is somewhat academic since it is predicted to occur for silicon at very low temperatures in a vacuum, it can have technological applications for other material systems where reconstructions occur at higher temperatures under ambient conditions. For example, Zheng et al [181] observed superheating of Cu_2S nanorods due to phase transformations from a low-chalcocite to a high-chalcocite phase induced by electron beam heating. The TPI-IRLS and continuum-KMC methods described in this chapter can be applied to this problem and to an entire class of physical phenomena of similar nature. These are promising areas for future research.

Bibliography

[1] E. B. Tadmor, R. E. Miller, and R. S. Elliott. *Continuum Mechanics and Thermodynamics*. Cambridge University Press, Cambridge, 2012. (Cited on pages 1, 8, 87, and 102.)

[2] D. D. Joseph and L. Preziosi. Heat waves. *Rev. Mod. Phys.*, 61(1):41–73, 1989. (Cited on pages 1, 3, 7, 13, 18, 22, 28, 86, and 88.)

[3] C. L. Tien and G. Chen. Challenges in microscale conductive and radiative heat transfer. *J. Heat Transfer*, 116:799–807, 1994. (Cited on pages 1, 2, and 8.)

[4] C. L. Tien and J. H. Lienhard. *Statistical Thermodynamics*. McGraw-Hill, New York, revised edition, 1979. (Cited on page 2.)

[5] D. Y. Tzou. *Macro- to Microscale Heat Transfer*. Taylor & Francis, Washington, DC, US, 1st edition, 1997. (Cited on pages 2, 8, and 13.)

[6] M. Chester. Second sound in solids. *Phys. Rev.*, 131(5):2013–2015, 1963. (Cited on pages 2 and 5.)

[7] C. Cattaneo. Sulla conduzione del calore. *Atti. Sem. Mat. Fis. Univ. Modena*, 3:83–101, 1948. (Cited on pages 3 and 88.)

[8] C. Cattaneo. Sur une forme de l'equation de la chaleur eliminant le paradoxe d'une propagation instantanée. *C. R. Acad. Sci. Paris*, 247:431–433, 1958. (Cited on pages 3 and 88.)

[9] P. Vernotte. Les paradoxes de la theorie continue de l'equatioin de la chaleur. *C. R. Acad. Sci.*, 246:3154–3155, 1958. (Cited on pages 3 and 88.)

[10] P. Vernotte. La véritable équation de la chaleu. *C. R. Acad. Sci.*, 247:2103–2105, 1958. (Cited on pages 3 and 88.)

[11] B. Straughan. *Heat Waves*. Springer, New York, 2011. (Cited on pages 3 and 4.)

[12] W. Kaminski. Hyperbolic heat conduction equation for materials with a nonhomogeneous inner structure. *J. Heat Transfer*, 112:555–560, 1990. (Cited on page 3.)

[13] K. Mitra, S. Kumar, A. Vedavarz, and M. K. Moallemi. Experimental evidence of hyperbolic heat conduction in processed meat. *J. Heat Trans.*, 117:568–573, 1995. (Cited on page 3.)

[14] H. Herwig and K. Beckert. Fourier versus non-Fourier heat conduction in materials with a nonhomogeneous inner structure. *J. Heat Transfer*, 122:363–365, 2000. (Cited on page 3.)

[15] E. P. Scott, M. Tilahun, and B. Vick. The question of thermal waves in heterogeneous and biological materials. *J. Biomech. Eng.*, 131:074518, 2009. (Cited on page 3.)

[16] C. L. Tien, A. Majumdar, M. I. Flik, S. Kotake, K. Hijikata, and Y. Hayashi. Molecular and microscale transport phenomena: A report of the Japan-U.S. joint seminar. *Ann. Rev. Heat Transfer*, 6:355–377, 1995. (Cited on page 3.)

[17] M. Asheghi. Microscale heat transfer. `http://www.electronics-cooling.com/2007/02/microscale` (Cited on page 3.)

[18] M. Asheghi, M. N. Touzelbaev, K. E. Goodson, Y. K. Leung, and S. S. Wong. Temperature-dependent thermal conductivity of single-crystal silicon layers in SOI substrates. *J. Heat Transfer*, 120:30–36, 1998. (Cited on page 3.)

[19] D. G. Cahill, W. K. Ford, K. E. Goodson, G. D. Mahan, A. Majumdar, H. J. Maris, R. Merlin, and S. R. Philpot. Nanoscale thermal transport. *J. Appl. Phys.*, 93:793–818, 2003. (Cited on page 3.)

[20] N. J. Pilgrim, W. Batty, R. W. Kelsall, and C.M. Snowden. Nanoscale electrothermal co-simulation: compact dynamic models of hyperbolic heat transport and self-consistent device Monte Carlo. *Microelectronics Journal*, 35:823–830, 2004. (Cited on page 3.)

[21] W. B. Lor and H. S. Chu. Hyperbolic heat conduction in thin-film high Tc superconductors with interface thermal resistance. *Cryogenics*, 39:739–750, 1999. (Cited on page 3.)

[22] G. J. Wagner, R. E. Jones, J. A. Templeton, and M. L. Parks. An atomistic-to-continuum coupling method for heat transfer in solids. *Comput. Methods Appl. Mech. Engrg.*, 197:3351–3365, 2008. (Cited on page 4.)

[23] D. E. Glass, M. N. Özişik, and B. Vick. Non-Fourier effects on transient temperature resulting from periodic on-off heat flux. *Int. J. Heat Mass Transfer*, 30(8):1623–1631, 1987. (Cited on page 4.)

[24] M. Human. Non-Fourier heat transfer in laser heated metal surfaces. In J. H. Kim et al., editor, *Heat Transfer: Korea-USA Seminar*, pages 521–533. 1986. (Cited on page 4.)

[25] D. Y. Tzou. The resonance phenomenon in thermal waves. *Int. J. Eng. Sci.*, 29:1167–1177, 1991. (Cited on pages 4 and 28.)

[26] D. Y. Tzou. Resonance of thermal waves under frequency excitations. *Fundamental in Conduction, ASME HTD*, 173:11–27, 1991. (Cited on pages 4 and 28.)

[27] D. Y. Tzou. Thermal resonance under frequency excitations. *J. Heat Transfer*, 114(2):310–316, 1992. (Cited on pages 4 and 28.)

[28] D. Y. Tzou. Damping and resonance phenomenon of thermal waves. *J. Appl. Mech.*, 59(4):862–867, 1992. (Cited on pages 4 and 28.)

[29] M.I. Flik and C. L. Tien. Size effects on the thermal conductivities of high-Tc thin-film superconductors. *J. Heat Transfer*, 112:872–881, 1990. (Cited on page 4.)

[30] G. Espinosa-Paredes and E. G. Espinosa-Martinez. Fuel rod model based on non-Fourier heat conduction equation. *Annals of Nuclear Energy*, 36:680–693, 2009. (Cited on page 4.)

[31] P. Galenko and D. Jou. Diffuse-interface model for rapid phase transformations in nonequilibrium systems. *Phys. Rev. E*, 71:046125–, 2005. (Cited on page 4.)

[32] J. Jiang. Convergence to equilibrium for a fully hyperbolic phase-field model with Cattaneo heat flux law. *Math. Meth. Appl. Sci.*, 32:1156–1182, 2009. (Cited on page 4.)

[33] S. Bargmann, R. Greve, and P. Steinmann. Simulation of cryovolcanism on Saturn's moon Enceladus with the Green-Naghdi theory of thermoelasticity. *Bulletin of Glaciological Research*, 26:23–32, 2008. (Cited on page 4.)

[34] L. Herrera and N. Falcón. Heat waves and thermohaline instability in a fluid. *Physics Letters A*, 201:33–37, 1995. (Cited on page 4.)

[35] Y. Dolak and T. Hillen. Cattaneo models for chemosensitive movements. *J. Math Biology*, 46:460–478, 2003. (Cited on page 4.)

[36] J. Liu. Preliminary survey on the mechanisms of the wave-like behaviors of heat transfer in living tissues. *Forschung in Ingenieurwesen*, 66:1–10, 2000. (Cited on page 4.)

[37] A. B. Duncan and G. P. Peterson. Review of microscale heat transfer. *Appl. Mech. Rev.*, 47(9):397–428, 1994. (Cited on page 4.)

[38] M. N. Özişik and D. Y. Tzou. On the wave theory in heat conduction. *J. Heat Transfer*, 116:526–535, 1994. (Cited on page 4.)

[39] A. J. C. Ladd, B. Moran, and W. G. Hoover. Lattice thermal conductivity: A comparison of molecular dynamics and anharmonic lattice dynamics. *Phys. Rev. B*, 34(8):5058–5064, 1986. (Cited on pages 4 and 48.)

[40] P. K. Schelling, S. R. Phillpot, and P. Keblinski. Comparison of atomic-level simulation methods for computing thermal conductivity. *Phys. Rev. B*, 65(14):144306, 2002. (Cited on pages 4, 6, 47, 49, 57, 63, 74, and 77.)

[41] D. H. Tsai and R. A. MacDonald. Molecular-dynamical study of second sound in a solid excited by a strong heat pulse. *Phys. Rev. B*, 14(10):4714–4723, 1976. (Cited on pages 5, 65, and 68.)

[42] S. Volz, J. B. Saulnier, M. Lallemand, B. Perrin, P. Depondt, and M. Mareschal. Transient Fourier-law deviation by molecular dynamics in solid argon. *Phys. Rev. B*, 54(1):340–347, 1996. (Cited on pages 5 and 47.)

[43] M. A. Osman and D. Srivastava. Molecular dynamics simulations of heat pulse propagation in single-wall carbon nanotubes. *Phys. Rev. B*, 72(12):125413, 2005. (Cited on pages 5 and 65.)

[44] J. Shiomi and S. Maruyama. Non-Fourier heat conduction in a single-walled carbon nanotube: Classical molecular dynamics simulations. *Phys. Rev. B*, 73(20):205420, 2006. (Cited on page 5.)

[45] Q. Liu, P. Jiang, and H. Xiang. Molecular dynamics simulations of non-Fourier heat conduction. *Prog. Nat. Sci.*, 18:999–1007, 2008. (Cited on page 5.)

[46] S. P. A. Gill. Nonequilibrium molecular dynamics and multiscale modeling of heat conduction in solids. In T. Dumitrica, editor, *Trends in Computational Nanomechanics*, volume 9, pages 85–134. Springer, 2010. (Cited on pages 6 and 72.)

[47] A. Tenenbaum, G. Ciccotti, and R. Gallico. Stationary nonequilibrium states by molecular dynamics. *Phys. Rev. A*, 25(5):27778–2787, 1982. (Cited on page 6.)

[48] K. Aoki and D. Kusnezov. Bulk properties of anharmonic chains in strong thermal gradients: non-equilibrium phi4 theory. *Phys. Lett. A*, 265(4):250–256, 2000. (Cited on page 6.)

[49] L. P. Pitaevskii and E. M. Lifshitz. *Physical Kinetics*. Butterworth-Heinenann, Oxford, UK, 1995. (Cited on pages 6, 75, and 76.)

[50] D. A. Young and H. J. Maris. Lattice-dynamical calculations of the Kapitza resistance between fcc lattices. *Phys. Rev. B*, 40:3685–3693, 1989. (Cited on page 6.)

[51] A. V. Savin and O. V. Gendelman. Heat conduction in one-dimensional lattices with on-site potential. *Phys. Rev. E*, 67(4):041205–1–041205–12, 2003. (Cited on page 6.)

[52] S. Lepri, R. Livi, and A. Politi. Thermal conduction in classical low-dimensional lattices. *Physics Reports*, 377:1–80, 2003. (Cited on pages 6, 63, and 77.)

[53] K. Jolley and S. P. A. Gill. Modelling transient heat conduction in solids at multiple length and time scales: a coupled non-equilibrium MD-continuum approach. *J. Comput. Phys.*, 228(19):7412–7425, 2009. (Cited on page 6.)

[54] A. Singh and E. B. Tadmor. Removing artificial kapitza effects from bulk thermal conductivity calculations in direct molecular dynamics. *J. Appl. Phys.*, 117:185101–1–185101–7, 2015. (Cited on pages 6, 103, and 108.)

[55] B. C. Daly, H. J. Maris, K. Imamura, and S. Tamura. Molecular dynamics calculation of the thermal conductivity of superlattices. *Phys. Rev. B*, 66:024301, 2002. (Cited on pages 6 and 50.)

[56] A. Guitton and D. J. Verschuur. Adaptive subtraction of multiples using the l1-norm. *Geophysical Prospecting*, 52(1):27–38, 2004. (Cited on pages 7, 86, and 93.)

[57] A. Chatterjee and D. G. Vlachos. An overview of spatial microscopic and accelerated kinetic Monte Carlo methods. *J. Comput.-Aided Mater. Des.*, 14(2):253–308, 2007. (Cited on pages 7 and 86.)

[58] G. Henkelman, B. P. Uberuaga, and H. Jónsson. A climbing image nudged elastic band method for finding saddle points and minimum energy paths. *J. Chem. Phys.*, 113:9901–9904, 2000. (Cited on pages 7, 86, and 100.)

[59] Sadik Kakac and Yaman Yener. *Heat Conduction*. Taylor & Francis, Washington, DC, US, 3rd edition, 1993. (Cited on page 8.)

[60] D. Y. Tzou. A unified field approach for heat conduction from macro- to micro-scales. *J. Heat Transfer*, 117(1):8–16, 1995. (Cited on pages 9, 22, and 28.)

[61] D. Y. Tzou. An engineering assessment to the relaxation-time in thermal wave-propagation. *Int. J. Heat Mass Transfer*, 36(7):1845–1851, 1993. (Cited on pages 9, 22, and 28.)

[62] M. I. Kaganov, I. M. Lifshitz, and L. V. Tanatarov. Relaxation between electrons and crystalline lattices. *Sov. Phys. JETP*, 4:173–178, 1957. (Cited on page 11.)

[63] S. I. Anisimov, B. L. Kapeliovich, and T. L. Perelḿan. Electron emission from metal surfaces exposed to ultra-short laser pulses. *Sov. Phys. JETP*, 39:375–377, 1974. (Cited on page 11.)

[64] T. Q. Qiu and C. L. Tien. Heat transfer mechanisms during short-pulse laser heating of metals. *J. Heat Transfer*, 115(4):835–841, 1993. (Cited on page 11.)

[65] T. Q. Qiu and C. L. Tien. Short-pulse laser heating on metals. *Int. J. Heat Mass Transfer*, 35(3):719–726, 1992. (Cited on page 11.)

[66] R. A. Guyer and J. A. Krumhansl. Solution of the linearized Boltzmann equation. *Phys. Rev.*, 148(2):766–778, 1966. (Cited on pages 12 and 64.)

[67] M. E. Gurtin and A. C. Pipkin. A general theory of heat conduction with finite wave speeds. *Arch. Rational Mech. Anal.*, 31(22):113–126, 1968. (Cited on pages 13 and 88.)

[68] J. W. Nunziato. On heat conduction in materials with memory. *Quart. Appl. Math.*, 29(2):187–204, 1971. (Cited on pages 13, 17, and 88.)

[69] B. D. Coleman. Thermodynamics of materials with memory. *Arch. Rational Mech. Anal.*, 17(1):1–46, 1964. (Cited on page 13.)

[70] B. D. Coleman and W. Noll. An approximation theory of functionals, with applications in continuum mechanics. *Arch. Rational Mech. Anal.*, 6(1):355–370, 1960. (Cited on page 13.)

[71] W. M. Rohsenow, J. P. Hartnett, and Y. I. Cho. *Handbook of Heat Transfer*. McGraw-Hill, New York, NY, US, 3rd edition, 1998. (Cited on page 19.)

[72] N. Metropolis, A. W. Rosenbluth, M. N. Rosenbluth, A. H. Teller, and E. Teller. Equation of state calculations by fast machines. *J. Chem. Phys.*, 21(6):1087–1092, 1953. (Cited on pages 30 and 36.)

[73] E. Fermi, J. Pasta, and S. Ulam. Studies of nonlinear problems. *Document LA-1940*, 1955. (Cited on page 30.)

[74] E. Fermi, E. Amaldi, H. L. Anderson, E. Persico, F. Rasetti, C. S. Smith, A. Wattenberg, and E. Segrè. *The Collected Papers of Enrico Fermi: Volume II.* University of Chicago Press, Chicago, IL, US, 1965. (Cited on page 30.)

[75] B. J. Alder and T. E. Wainwright. Phase transition for a hard sphere system. *J. Chem. Phys.*, 27(5):1208–1209, 1957. (Cited on page 30.)

[76] B. J. Alder and T. E. Wainwright. Studies in molecular dynamics. I. general method*. *J. Chem. Phys.*, 31(2):459–466, 1959. (Cited on page 30.)

[77] A. Rahman. Correlations in the motion of atoms in liquid argon. *Phys. Rev.*, 136(2 A):405–411, 1964. (Cited on page 30.)

[78] L. Verlet. Computer "experiments" on classical fluids. I. Thermodynamical properties of Lennard-Jones molecules. *Phys. Rev.*, 159(1):98–103, 1967. (Cited on pages 30, 33, and 37.)

[79] W. K. Liu, E. G. Karpov, S. Zhang, and H. S. Park. An introduction to computational nanomechanics and materials. *Comput. Methods Appl. Mech. Eng.*, 193:1529–1578, 2004. (Cited on pages 30, 31, and 32.)

[80] G. C. Maitland, M. Rigby, E. B. Smith, and W. A. Wakeham. *Intermolecular forces: their origin and determination.* Clarendon Press, Oxford, 1981. (Cited on page 31.)

[81] C. G. Gray and K. E. Gubbins. *Theory of molecular fluids. 1. Fundamnetals.* Clarendon Press, Oxford, 1984. (Cited on page 31.)

[82] A. J. Stone. *The Theory of Intermolecular Forces.* Clarendon Press, Oxford, 1996. (Cited on page 31.)

[83] S. Yip. *Handbook of Material Modelling*. Springer, Dordrecht, The Netherlands, 2005. (Cited on page 31.)

[84] E. B. Tadmor and R. E. Miller. *Modeling Materials*. Cambridge University Press, Cambridge, 2011. (Cited on pages 31, 46, 72, and 94.)

[85] J. E. Jones. On the determination of molecular fields. I. From the variation of the viscosity of a gas with temperature. *Proc. Roy. Soc. A*, 106:441–462, 1924. (Cited on pages 31 and 55.)

[86] J. E. Jones. On the determination of molecular fields. I. From the equation of state of a gas. *Proc. Roy. Soc. A*, 106:463–477, 1924. (Cited on pages 31 and 55.)

[87] L. Verlet. Computer "experiments" on classical fluids. II. Equilibrium correlation functions. *Phys. Rev.*, 165(1):201–214, 1968. (Cited on page 33.)

[88] Dan Frenkel and Berend Smit. *Understanding Molecular Simulation*. Academic Press, San Diego, CA, US, 2nd edition, 2002. (Cited on pages 33, 35, 36, 45, 55, and 94.)

[89] W. C. Swope, H. C. Andersen, P. H. Berens, and K. R. Wilson. A computer simulation method for the calculation of equilibrium constants for the formation of physical clusters of molecules: application to small water clusters. *J. Chem. Phys.*, 76(1):637–649, 1982. (Cited on pages 33 and 34.)

[90] M. P. Allen and D. J. Tildesley. *Computer Simulation of Liquids*. Oxford University Press, New York, 1987. (Cited on pages 35, 36, 37, 39, and 62.)

[91] D. Janežič and B. Orel. Implicit Runge-Kutta method for molecular dynamics integration. *J. Chem. Inf. Comput. Sci.*, 33(2):252–257, 1993. (Cited on page 35.)

[92] D. Ruelle. *Statistical Mechanics*. W. A. Benjamin, Inc., New York, US, 1969. (Cited on page 35.)

[93] J. Jellinek and D. H. Li. Separation of the energy of overall rotation in any N-body system. *Phys. Rev. Lett.*, 62(3):241–244, 1989. (Cited on pages 38, 46, 55, and 94.)

[94] D. C. Rapaport. *The Art of Molecular Dynamics Simulation*. Cambridge University Press, New York, US, 2nd edition, 2004. (Cited on page 39.)

[95] H. C. Andersen. Molecular dynamics simulations at constant pressure and/or temperature. *J. Chem. Phys.*, 72(4):2384–2393, 1980. (Cited on pages 39 and 40.)

[96] H. C. Andersen, M. P. Allen, A. Bellemans, J. Board, J. H. R. Clarke, M. Ferrario, J. M. Haile, S. Nosé, J. V. Opheusden, and J. P. Ryckaert. New molecular dynamics methods for various ensembles. *Rapport d'Activite Scientifique du CECAM, Orsay, France*, 9:82–115, 1984. (Cited on page 39.)

[97] H. J. C. Berendsen, J. P. M. Postma, W. F. VanGunsteren, A. DiNola, and J. R. Haak. Molecular dynamics with coupling to an external bath. *J. Chem. Phys.*, 81(8):3684–3690, 1984. (Cited on page 40.)

[98] W. G. Hoover, A. J. C. Ladd, and B. Moran. High-strain-rate plastic flow studied via nonequilibrium molecular dynamics. *Phys. Rev. Lett.*, 48(26):1818–1820, 1982. (Cited on page 40.)

[99] D. J. Evans. Molecular dynamics simulations at constant pressure and/or temperature. *J. Chem. Phys.*, 78(6):3297–3302, 1983. (Cited on page 40.)

[100] D. J. Evans and G. Morriss. *Statistical Mechanics of Nonequilibrium Liquids*. Cambridge University Press, New York, US, 2nd edition, 2008. (Cited on pages 40, 41, 47, 55, and 94.)

[101] H. Mori. Transport, collective motion, and Brownian motion. *Progr. Theor. Phys.*, 33(3):423–455, 1965. (Cited on page 41.)

[102] H. Mori. A continued-fraction representation of the time-correlation functions. *Progr. Theor. Phys.*, 34(3):399–416, 1965. (Cited on page 41.)

[103] R. Zwanzig. Ensemble method in the theory of irreversibility. *J. Chem. Phys.*, 33(5):1338–1241, 1960. (Cited on page 41.)

[104] R. Zwanzig. Statistical mechanics of irreversible processes. *Lectures in Theor. Phys.*, 3:106–141, 1961. (Cited on page 41.)

[105] R. Zwanzig. Memory effects in irreversible thermodynamics. *Phys. Rev.*, 124(4):983–992, 1961. (Cited on page 41.)

[106] S. Chandrasekhar. Stochastic problems in physics and astronomy. *Rev. Mod. Phys.*, 15(1):1–89, 1943. (Cited on page 43.)

[107] S. Nosé. A unified formulation of the constant temperature molecular dynamics methods. *J. Chem. Phys.*, 81(1):511–519, 1984. (Cited on pages 44, 55, and 94.)

[108] S. Nosé. A molecular dynamics method for simulations in the canonical ensemble. *Mol. Phys.*, 52(2):255–268, 1984. (Cited on pages 44 and 55.)

[109] W. G. Hoover. Canonical dynamics: Equilibrium phase-space distributions. *Phys. Rev. A*, 31(3):1695–1697, 1985. (Cited on pages 45, 55, and 94.)

[110] W. G. Hoover. Constant pressure equations of motion. *Phys. Rev. A*, 34(3):2499–2500, 1986. (Cited on pages 45 and 55.)

[111] G. J. Martyna, M. L. Klein, and M. Tuckerman. Nosé-hoover chains: The canonical ensemble via continuous dynamics. *J. Chem. Phys.*, 97(4):2635–2645, 1992. (Cited on pages 45, 55, and 94.)

[112] J. H. Irving and J. G. Kirkwood. The statistical mechanical theory of transport processes. IV. The equations of hydrodynamics. *J. Chem. Phys.*, 18(6):817–829, 1950. (Cited on page 48.)

[113] S. G. Volz and G. Chen. Molecular dynamics simulation of thermal conductivity of silicon nanowire. *Appl. Phys. Lett.*, 75(14):2056–2058, 1999. (Cited on page 48.)

[114] N. C. Admal and E. B. Tadmor. Stress and heat flux for arbitrary multibody potentials: A unified framework. *J. Chem. Phys.*, 134:184106, 2011. (Cited on page 48.)

[115] F. H. Stillinger and T. A. Weber. Computer simulation of local order in condensed phases of silicon. *Phys. Rev. B*, 31(8):5262–5271, 1985. (Cited on pages 48, 86, and 94.)

[116] X. W. Zhou, S. Aubry, R. E. Jones, A. Greenstein, and P. K. Schelling. Towards more accurate molecular dynamics calculation of thermal conductivity: Case study of GaN bulk crystals. *Phys. Rev. B*, 79(11):115201–1–115201–17, 2009. (Cited on pages 49, 58, and 74.)

[117] D. P. Sellan, E. S. Landry, J. E. Turney, A. J. H. McGaughey, and C. H. Amon. Size effects in molecular dynamics thermal conductivity predictions. *Phys. Rev. B*, 81:214305, 2010. (Cited on pages 49, 63, 64, 78, 81, and 108.)

[118] T. X. Nguyen, S. K. Bhatia, and D. Nicholson. Prediction of high-pressure adsorption equilibrium of supercritical gases using density functional theory. *Langmuir*, 21(7):3187–3197, 2005. (Cited on page 55.)

[119] E. B. Tadmor. Truncated lennard-jones model for Ar with parameters from Nguyen. `https://openkim.org/cite/MO_398194508715_000`. (Cited on page 55.)

[120] E. B. Tadmor. Driver for the Lennard-Jones model truncated to have zero energy above the cutoff radius. `https://openkim.org/cite/MD_132729421025_000`. (Cited on page 55.)

[121] E. B. Tadmor, R. S. Elliott, J. P. Sethna, R. E. Miller, and C. A. Becker. The potential of atomistic simulations and the Knowledgebase of Interatomic Models. *JOM*, 63:17, 2011. (Cited on pages 55 and 94.)

[122] T. Schneider and E. Stoll. Molecular-dynamics study of a three-dimensional one-component model for distortive phase transitions. *Phys. Rev. B*, 17(3):1302–1322, 1978. (Cited on pages 55, 58, and 94.)

[123] S. J. Plimpton. Fast parallel algorithms for short-range molecular dynamics. *J. Comput. Phys.*, 117:1–19, 1995. (Cited on pages 55 and 94.)

[124] LAMMPS website. `http://lammps.sandia.gov/`. (Cited on pages 55 and 94.)

[125] W. Shinoda, M. Shiga, and M. Mikami. Rapid estimation of elastic constants by molecular dynamics simulation under constant stress. *Phys. Rev. B*, 69(13):134103–1–134103–8, 2004. (Cited on pages 56 and 95.)

[126] D. J. Tobias, G. J. Martyna, and M. L. Klein. Molecular dynamics simulations of a protein in the canonical ensemble. *J. Phys. Chem.*, 97(49):12959–12966, 1993. (Cited on page 56.)

[127] M. Parrinello and A. Rahman. Crystal structure and pair potentials: A molecular-dynamics study. *Phys. Rev. Lett.*, 45(14):1196–1199, 1980. (Cited on page 56.)

[128] G. J. Keeler and D. N. Batchelder. Measurement of the elastic constants of argon from 3 to 77 degrees K. *J. Phys. C: Solid State Phys.*, 3:510–522, 1970. (Cited on page 61.)

[129] H. Kaburaki, J. Li, S. Yip, and H. Kimizuka. Dynamical thermal conductivity of argon crystal. *J. Appl. Phys.*, 102(4):043514–1–043514–6, 2007. (Cited on pages 63, 80, and 81.)

[130] R. Berman. *Thermal Conduction in Solids*. Oxford University Press, Oxford, 1976. (Cited on page 64.)

[131] H. E. Jackson and C. T. Walker. Thermal conductivity, second sound, and phonon-phonon interactions in NaF. *Phys. Rev. B*, 3(4):1428–1439, 1971. (Cited on page 65.)

[132] C. Feldman and M. L. Klein. On the velocity of sound in solid argon. *Phys. Lett. A*, 25(3):190–191, 1967. (Cited on page 68.)

[133] L. Finegold and N. E. Phillips. Low-temperature heat capacities of solid argon and krypton. *Phys. Rev.*, 177:1383–1391, 1969. (Cited on page 69.)

[134] P. L. Kapitza. *J. Phys. USSR*, 4:181, 1941. (Cited on page 72.)

[135] G. L. Pollack. Kapitza resistance. *Rev. Mod. Phys.*, 41(1):48–81, 1969. (Cited on page 73.)

[136] M. E. Lumpkin, W. M. Saslow, and W. M. Visscher. Kapitza conductance: Comparison of the phonon mismatch theory with computer experiments. *Phys. Rev. B*, 17(11):4295–4302, 1978. (Cited on page 73.)

[137] I. M. Khalatnikov. *Zh. Eksp. Teor. Fiz.*, 22:687–, 1952. (Cited on page 73.)

[138] R. J. Stoner and H. J. Maris. Kapitza conductance and heat flow between solids at temperatures from 50 to 300 K. *Phys. Rev. B*, 48:16373–16387, 1993. (Cited on page 73.)

[139] S. Shenogin, L. Xue, R. Ozisik, P. Keblinski, and D. G. Cahill. Role of thermal boundary resistance on the heat flow in carbon-nanotube composites. *J. Appl. Phys.*, 95(12):8136–8144, 2004. (Cited on page 74.)

[140] P. K. Schelling, S. R. Phillpot, and P. Keblinski. Kapitza conductance and phonon scattering at grain boundaries by simulation. *J. Appl. Phys.*, 95:6082–6091, 2004. (Cited on page 74.)

[141] A. J. Cao and J. M. Qu. Kapitza conductance of symmetric tilt grain boundaries in graphene. *J. Appl. Phys.*, 111:053529, 2012. (Cited on page 74.)

[142] B. Deng, A. Chernatynskiy, M. Khafizov, D. H. Hurley, and S. R. Phillpot. Kapitza resistance of Si/SiO_2 interface. *J. Appl. Phys.*, 115:084910, 2014. (Cited on page 74.)

[143] A. Singh and E. B. Tadmor. Thermal parameter identification for non-Fourier heat transfer from molecular dynamics. *J. Comp. Phys.*, 2014. Submitted. (Cited on pages 74, 88, 89, 90, 94, 95, 97, and 108.)

[144] K. V. Tretiakov and S. Scandolo. Thermal conductivity of solid argon from molecular dynamics simulations. *J. Chem. Phys.*, 120(8):3765–3769, 2004. (Cited on page 75.)

[145] P. B. Allen. Size effects in thermal conduction by phonons. *Phys. Rev. B.*, 90:054301, 2014. (Cited on pages 77, 78, and 103.)

[146] D. K. Christen and G. L. Pollack. Thermal conductivity of solid argon. *Phys. Rev. B*, 12:3380–3391, 1975. (Cited on pages 80 and 81.)

[147] M.-C. Desjonquères and D. Spanjaard. *Concept in surface physics*. Springer-Verlag, Heidelberg, Berlin, Germany, 1993. (Cited on page 85.)

[148] R. E. Schlier and H.E. Farnsworth. Structure and adsorption characteristics of clean surfaces of Germanium and Silicon. *J. Chem. Phys.*, 30:917, 1959. (Cited on page 85.)

[149] J. J. Lander and J. Morrison. Low voltage electron diffraction study of the oxidation and reduction of silicon. *J. Appl. Phys.*, 33(6):2089–2092, 1962. (Cited on page 85.)

[150] T. D. Poppendieck, T. C. Ngoc, and M. B. Webb. An electron diffraction study of the structure of silicon (100). *Surf. Sci.*, 75(2):287–315, 1978. (Cited on page 85.)

[151] R. M. Tromp, R. J. Hamers, and J. E. Demuth. Dimer structure observed with scanning tunneling microscopy. *Phys. Rev. Lett.*, 55(12):1303–1306, 1985. (Cited on page 85.)

[152] Y. Kondo, T. Amakusa, M. Iwatsuki, and H. Tokumoto. Phase transition of the Si(001) surface below 100 k. *Surf. Sci.*, 453:L318–L322, 2000. (Cited on page 85.)

[153] P. Perdigão, D. Deresmes, B. randidier, M. Dubois, C. Delerue, G. Allan, and D. Stiévenard. Semiconducting surface reconstructions of p-type Si(100) substrates at 5 k. *Phys. Rev. Lett.*, 92(21):216101–1–216101–4, 2004. (Cited on page 85.)

[154] Y. J. Li, Y. Sugawara, C. Hobbs, Y. Naitoh, M. Kageshima, H. Nomura, N. Ozaki, and L. Kantorovich. Origin of p(2x1) phase on Si(001) by noncontact atomic force microscopy at 5 K. *Phys. Rev. Lett.*, 96, 2006. (Cited on page 85.)

[155] G. Le Lay, A. Cricenti, C. Ottaviani, P. Perfetti, T. Tanikawa, I. Matsuda, and S. Hasegawa. Evidence of asymmetric dimers down to 40 k at the clean Si(100) surface. *Phys. Rev. B*, 66(15):153317–1–153317–4, 2002. (Cited on page 85.)

[156] M. Ono, A. Kamoshida, N. Matsuura, E. Ishikawa, T. Eguchi, and Y. Hasegawa. Dimer buckling of the Si(001) 2 x 1 surface below 10 k observed by low-temperature scanning tunneling microscopy. *Phys. Rev. B*, 67(20):201306–1–201306–4, 2003. (Cited on page 85.)

[157] C. Guo, K. Hermann, and Y. Zhao. Dynamics and energetics of reconstruction at the Si(100) surface. *J. Phys. Chem. C*, 118:25614–25619, 2014. (Cited on page 85.)

[158] M. T. Yin and M. L. Cohen. Theoretical determination of surface atomic geometry: Si(001)-(2x1). *Phys. Rev. B*, 24(4):2303–2306, 1981. (Cited on page 85.)

[159] I. P. Batra. Atomic structure of the Si(001)-(2x1) surface. *Phys. Rev. B*, 41(8):5048–5054, 1990. (Cited on page 85.)

[160] N. Roberts and R. J. Needs. Total energy calculations of dimer reconstructions on the silicon (001) surface. *Surf. Sci.*, 236:112–121, 1990. (Cited on page 85.)

[161] J. Dąbrowski and M. Scheffler. Self-consistent study of the electronic and structural properties of the clean Si(001)(2 x 1) surface. *Appl. Surf. Sci.*, 56:15–19, 1992. (Cited on page 85.)

[162] Ramstad. A., G. Brocks, and P. J. Kelly. Theoretical study of the Si(100) surface reconstruction. *Phys. Rev. B*, 51(20):14504–14524, 1995. (Cited on page 85.)

[163] H. Jeffreys. *The Earth: Its Origin, History and Physical Constitution.* Cambridge University Press, Cambridge, 8 edition, 1976. (Cited on page 88.)

[164] T. G. Müller and J. Timmer. Parameter identification techniques for partial differential equations. *Int. J. Bifurcat. Chaos,*, 14(6):2053–2060, 2004. (Cited on page 91.)

[165] I. J. Schoenberg. Spline functions and the problem of graduation. *Proc. Nat. Acad. Sci. USA*, 52:947–950, 1964. (Cited on page 91.)

[166] C. H. Reinsch. Smoothing by spline functions. *Numer. Math.*, 10:177–183, 1967. (Cited on page 91.)

[167] Carl de Boor. *A Practical Guide to Splines.* Springer Verlag, New York, revised edition, 2001. (Cited on page 91.)

[168] Oleg M. Alifanov. *Inverse Heat Transfer Problems.* Springer Verlag, Berlin Heidelberg, 1994. (Cited on page 92.)

[169] A. Singh. A three-body Stillinger-Weber (SW) model (parameterization) for Silicon, 2013. `https://openkim.org/cite/MO_405512056662_001`. (Cited on page 94.)

[170] A. Singh. A three-body Stillinger-Weber (SW) potential for Silicon, 2013. `https://openkim.org/cite/MD_335816936951_001`. (Cited on page 94.)

[171] L. Ott and M. Longnecker. *An introduction to statistical methods and data analysis*. Duxbury Press, California, 1st edition, 2001. (Cited on page 96.)

[172] E. T. Gawlinski and J. D. Gunton. Molecular-dynamics simulation of molecular-beam epitaxial growth of the silicon (100) surface. *Phys. Rev. B*, 36(9):4774–4781, 1987. (Cited on page 99.)

[173] J. Lampinen, R. M. Nieminen, and K. Kaski. Molecular dynamics simulation of epitaxial growth of the si(001) surface. *Surf. Sci.*, 203(1–2):201–211, 1988. (Cited on page 99.)

[174] G. H. Vineyard. Frequency factors and isotope effects in solid state rate processes. *J. Phys. Chem. Solids*, 3(1–2):121–127, 1957. (Cited on page 102.)

[175] G. Henkelman and H. Jónsson. Long time scale kinetic Monte Carlo simulations without lattice approximation and predefined event table. *J. Chem. Phys.*, 115(21):9657–9666, 2001. (Cited on page 102.)

[176] T. Lazauskas, S. D. Kenny, and R. Smith. Influence of the prefactor to defect motion in α-iron during long time scale simulations. *J. Phys. Condens. Matter*, 26(39):395007–1–395007–8, 2014. (Cited on page 102.)

[177] R. Courant, K. Friedrichs, and H. Lewy. Über die partiellen differenzengleichungen der mathematischen physik. *Mathematische Annalen*, 100(1):32–74, 1928. (Cited on page 103.)

[178] H. D. Baehr and K. Stephan. *Heat and mass transfer*. Springer, San Diego, CA, US, 3rd edition, 2011. (Cited on page 104.)

[179] A. Prados, J. J. Brey, and B. Sánchez-Rey. A dynamical Monte Carlo algorithm for master equations with time-dependent transition rates. *J. Stat. Phys.*, 89:709–734, 1997. (Cited on page 105.)

[180] J. C. Thompson and B. A. Younglove. Thermal conductivity of silicon at low temperatures. *J. Phys. Chem. Solids*, 20:146–149, 1961. (Cited on page 108.)

[181] H. Zheng, J. B. Rivest, T. A. Miller, B. Sadtler, A. Lindenberg, M. F. Toney, L. Wang, C. Kisielowski, and A. P. Alivisatos. Observation of transient structural-transformation dynamics in a cu_2s nanorod. *Science*, 333(6039):206–209, 2009. (Cited on pages 109 and 118.)

[182] P. D. Lax and R. D. Richtmyer. Survey of the stability of linear finite-difference equations. *Comm. Pure Appl. Math.*, 9:267–293, 1956. (Cited on page 141.)

Appendix A

Well-Posedness of the TPI solution

We demonstrate that the PDE in Eq. (3.68) is well-posed in the Hadamard sense, i.e., we show the existence, uniqueness and stability of the solution in Eq. (3.76).

Existence: The solution in Eq. (3.76) is infinitely differentiable as $\sin\lambda_2 t$, $\cos\lambda_2 t$, $e^{\lambda_1 t}, e^{\lambda_3 t}$, t are infinitely differentiable functions. From Eq. (3.75) we have $\lambda_1 < 0$, if $\tau_q > 0$ and $\alpha, \tau_\theta \geq 0$, so $e^{\lambda_1 t} \leq 1$. Also $\lambda_3 < |\lambda_1|$, so $e^{(\lambda_1+\lambda_3)t} < 1$ and $e^{(\lambda_1-\lambda_3)t} < 1$. For all cases in Eq. (3.74), it can be easily shown that $\max_{t\geq 0} T(t) = T(0) = 1$. When $\lambda_2^2 > 0$, we have $\left|\dot{T}(t)\right| < \frac{\lambda_1^2+\lambda_2^2}{\lambda_2}$, and $\left|\ddot{T}(t)\right| < \frac{\lambda_1^2+\lambda_2^2}{\lambda_2}(|\lambda_1| + |\lambda_2|)$. When $\lambda_2^2 < 0$, we have $\left|\dot{T}(t)\right| < \frac{\lambda_1^2-\lambda_3^2}{2\lambda_3}$, and $\left|\ddot{T}(t)\right| < \frac{\lambda_1^2-\lambda_3^2}{2\lambda_3}(|\lambda_1| + \lambda_3)$. And for the final case when $\lambda_2^2 = 0$, we have $\max_{t\geq 0}\left|\dot{T}(t)\right| = \left|\dot{T}(t = -1/\lambda_1)\right| = |\lambda_1|/e$ and $\max_{t\geq 0}\left|\ddot{T}(t)\right| = \left|\dot{T}(t = -2/\lambda_1)\right| = \lambda_1^2/e^2$. Therefore, $|\theta(x,t)|$, $\left|\frac{\partial\theta}{\partial t}(x,t)\right|$, $\left|\frac{\partial^2\theta}{\partial t^2}(x,t)\right|$, $\left|\frac{\partial^2\theta}{\partial x^2}(x,t)\right|$, $\left|\theta\frac{\partial^3\theta}{\partial x^2\partial t}(x,t)\right|$, all are bounded in their domain $(0,L)\times(0,+\infty)$. Thus the solution and derivatives appearing in the model are bounded up and the existence of the solution is confirmed.

Uniqueness: If $\tilde{\theta}$ is another solution to Eq. (3.68), then $w := \theta - \tilde{\theta}$ solves

$$\begin{cases} w_{tt} + \frac{1}{\tau_q} w_t & = c^2 w_{xx} + c^2\tau_\theta w_{xxt}, \\ w(x,0) & = 0, \quad 0 \leq x \leq L, \\ w_t(x,0) & = 0, \quad 0 \leq x \leq L, \end{cases} \tag{A.1}$$

where $w_t = \frac{\partial w}{\partial t}$, $w_{tt} = \frac{\partial^2 w}{\partial t^2}$, $w_{xx} = \frac{\partial^2 w}{\partial x^2}$, $w_{xxt} = \frac{\partial^3 w}{\partial x^2 \partial t}$, and $c^2 = \alpha/\tau_q$. We define the

energy function as

$$E(t) := \frac{1}{2}\int_0^L \left(w_t^2 + c^2 w_x^2\right) dx. \tag{A.2}$$

Using periodic BCs so that $w_x(0,t) = w_x(L,t)$ and $w_{xx}(0,t) = w_{xx}(L,t)$, and integration by parts, we have $\int_0^L w_x w_{xt} dx = -\int_0^L w_t w_{xx} dx$ and $\int_0^L w_t w_{xxt} dx = -\int_0^L w_{xt}^2 dx$. Thus

$$\begin{aligned}
\frac{dE}{dt} &= \int_0^L \left(w_t w_{tt} + c^2 w_x w_{xt}\right) dx \\
&= \int_0^L w_t \left(w_{tt} - c^2 w_{xx}\right) dx = \int_0^L w_t \left(-\frac{w_t}{\tau_q} + c^2 \tau_\theta w_{xxt}\right) \\
&= -\int_0^L \frac{w_t^2}{\tau_q} dx - c^2 \tau_\theta \int_0^L w_{xt}^2 dx < 0.
\end{aligned}$$

Thus for $\tau_q > 0$ and $\tau_\theta \geq 0$, we have $\frac{dE}{dt} \leq 0$. This means $E(t) \leq E(0)$. Since $w(x,0) = 0$ and w is continuous, we have $w_x(x,0) = 0$. Also, $w_t(x,0) = 0$. Thus, $E(0) = 0$. Hence $E(t) = 0$ for $t \geq 0$. This means $w_t(x,t) = w_x(x,t) = 0$. Consequently, w is constant, and $w(x,t) = w(x,0) = 0$. This implies that the solution is unique.

Stability: If $\tilde{\theta}$ is a different solution to θ due to very small changes in the initial conditions, then as above for $w := \theta - \tilde{\theta}$, we can show that $E(t) \leq E(0)$. We define the function $F(t) := \int_0^L w^2 dx = \|w\|^2$, where $\|.\|$ is the L^2-norm. Taking the derivative with respect to time, we obtain $\frac{dF}{dt} = 2\int_0^L w w_t dx$. Since $\int_0^L (w - w_t)^2 dx \geq 0$, we have

$$\frac{dF}{dt} \leq \int_0^L (w^2 + w_t^2) dx \leq F(t) + 2E(t) \leq F(t) + 2E(0). \tag{A.3}$$

Multiplying both sides of Eq. (A.3) by e^{-t}, we obtain

$$\frac{d}{dt}\left(F(t)e^{-t}\right) \leq 2E(0)e^{-t}.$$

Integrating with respect to time over $t \in [0, t_0]$, we obtain

$$F(t) \leq F(0)e^{t_0} + 2E(0)(e^{t_0} - 1).$$

This means

$$\begin{aligned}
\|w(x,t)\|^2 &\leq \|w(x,0)\|^2 e^{t_0} + c^2 \|w_x(x,0)\|^2 (e^{t_0} - 1), \\
&\leq \left(\|w(x,0)\|^2 + c^2 \|w_x(x,0)\|^2\right) e^{t_0}.
\end{aligned}$$

Thus for any small constant $\epsilon > 0$, if $\|w(x,0)\| < \epsilon$, and $\|w_x(x,0)\| < \epsilon$, then $\|w(x,t)\|^2 \leq (1+c^2)e^{t_0}\epsilon^2$, or $\|w(x,t)\| \leq C\epsilon$, where C is a constant. This means that the difference between the two solutions θ and $\tilde{\theta}$ is bounded. Hence, the solution is stable.

Appendix B

Finite difference discretization schemes

The method used in Chapter 6 to numerically solve the continuum thermal partial differential equations is described.

B.1 Finite difference discretization scheme

In Chapter 6 two different partial differential equations (PDEs) were discretized: Jeffreys-type PDE as described in Eq. 6.10 and the Cattaneo-Vernotte (CV) model with heat source term as described in Eq. 6.32 of the main article. We call these two PDEs as PDE I and PDE II. (See Section 6.2, Section 6.3 and Section 6.6 of Chapter 6 for details.)

B.1.1 Solving PDE I

In Section 6.2 of Chapter 6, we derive a one-dimensional (1D) Jeffreys-type partial differential equation for temperature evolution:

$$\frac{\partial\theta}{\partial t} = -\tau_q\frac{\partial^2\theta}{\partial t^2} + \frac{k_0}{\gamma}\left[\left(\frac{\theta}{\theta_0}\right)^s\left(\frac{s}{\theta}\left(\frac{\partial\theta}{\partial x}\right)^2 + \frac{\partial^2\theta}{\partial x^2}\right)\right] + \frac{k_0\tau_\theta}{\gamma}\left[\left(\frac{\theta}{\theta_0}\right)^s\left(\frac{s}{\theta}\frac{\partial\theta}{\partial x}\frac{\partial^2\theta}{\partial x\partial t} + \frac{\partial^3\theta}{\partial x^2\partial t}\right)\right]. \tag{B.1}$$

Assuming that this equation holds at the bin centers x_n ($n = 2, \ldots, N_{\text{bins}} - 1$) at times t_m ($m = 1, 2, \ldots, M$), where t_M is the stopping time, we have from Eq. (B.1):

$$\partial_t \theta|_{mn} = -\tau_q \partial_{tt}\theta|_{mn} + \frac{k_0}{\gamma}\partial_{xx}\theta|_{mn} + \frac{k_0 \tau_\theta}{\gamma}\partial_{xxt}\theta|_{mn}, \tag{B.2}$$

where

$$\partial_t \theta = \frac{\partial \theta}{\partial t}, \tag{B.3a}$$

$$\partial_{tt}\theta = \frac{\partial^2 \theta}{\partial t^2}, \tag{B.3b}$$

$$\partial_{xx}\theta = \Big(\frac{\theta}{\theta_0}\Big)^s \Big(\frac{s}{\theta}\Big(\frac{\partial \theta}{\partial x}\Big)^2 + \frac{\partial^2 \theta}{\partial x^2}\Big), \tag{B.3c}$$

$$\partial_{xxt}\theta = \Big(\frac{\theta}{\theta_0}\Big)^s \Big(\frac{s}{\theta}\frac{\partial \theta}{\partial x}\frac{\partial^2 \theta}{\partial x \partial t} + \frac{\partial^3 \theta}{\partial x^2 \partial t}\Big). \tag{B.3d}$$

All thermal parameters are obtained using the TPI-IRLS method described in Section 6.3 of Chapter 6.

Now Eq. (B.2) together with the initial and boundary conditions described in the main article is numerically solved by discretizing the differential terms with respect to time t and the spatial variable x using a Taylor series expansion [182]. In order to discretize $\partial_t \theta|_{mn}$ and $\partial_{tt}\theta|_{mn}$, a forward time discretization scheme and a central time discretization scheme are used, respectively. The central space discretization scheme is used to discretize $\partial_{xx}\theta|_{mn}$. For the term $\partial_{xxt}\theta|_{mn}$ that involves derivative of temperature in both variables t and x, we use backward difference in time and central difference in

space for discretization. Specifically, we have the following discretization expressions:

$$
\begin{aligned}
\partial_t\theta|_{mn} &= \frac{1}{\Delta t}\left[\theta|_{(m+1)n} - \theta|_{mn}\right] + \mathcal{O}(\Delta t),\\
\partial_{tt}\theta|_{mn} &= \frac{1}{\Delta t^2}\left[\theta|_{(m+1)n} - 2\theta|_{mn} + \theta|_{(m-1)n}\right] + \mathcal{O}(\Delta t^2),\\
\partial_x\theta|_{mn} &= \frac{1}{\Delta x_L + \Delta x_R}\left(\theta|_{m(n+1)}\frac{\Delta x_L}{\Delta x_R} - \theta|_{m(n-1)}\frac{\Delta x_R}{\Delta x_L}\right)\\
&\quad + \frac{\Delta x_R - \Delta x_L}{\Delta x_L \Delta x_R}\theta|_{mn} + \mathcal{O}(\Delta x^2),\\
\partial_{xx}\theta|_{mn} &= \left(\frac{\theta|_{mn}}{\theta_0}\right)^s\left[\frac{2}{\Delta x_L + \Delta x_R}\left(\frac{\theta|_{m(n+1)} - \theta|_{mn}}{\Delta x_R} + \frac{\theta|_{m(n-1)} - \theta|_{mn}}{\Delta x_L}\right)\right.\\
&\quad \left. + \frac{s}{\theta|_{mn}}\left(\partial_x\theta|_{mn}\right)^2\right] + \mathcal{O}(\Delta x^2),\\
\partial_{xxt}\theta|_{mn} &= \left(\frac{\theta|_{mn}}{\theta_0}\right)^s\left[\frac{2}{\Delta t(\Delta x_L + \Delta x_R)}\left(\frac{\theta|_{m(n+1)} - \theta|_{mn}}{\Delta x_R} + \frac{\theta|_{m(n-1)} - \theta|_{mn}}{\Delta x_L}\right.\right.\\
&\quad \left.\left. - \frac{\theta|_{(m-1)(n+1)} - \theta|_{(m-1)n}}{\Delta x_R} - \frac{\theta|_{(m-1)(n-1)} - \theta|_{(m-1)n}}{\Delta x_L}\right)\right.\\
&\quad \left. + \frac{s}{\theta|_{mn}\Delta t}\left(\left(\partial_x\theta|_{mn}\right)^2 - \left(\partial_x\theta|_{(m-1)n}\right)^2\right)\right] + \mathcal{O}(\Delta t, \Delta x^2),
\end{aligned}
\tag{B.4}
$$

where $\Delta t = t_{m+1} - t_m = t_m - t_{m-1}$, $\Delta x_L = x_n - x_{n-1}$, $\Delta x_R = x_{n+1} - x_n$.

Next we solve the continuum equation using an explicit scheme[1] where the current time step is the $(m+1)$th step. The temperature for each bin is calculated by all the known terms on the right hand side already stored from the previous time update.

B.1.2 Solving PDE II

This section describes the finite difference discretization scheme used to solve the CV model in Eq. (6.31) with the stochastic heat source term $r(\boldsymbol{x}, t)$. Assuming that the equation holds at the bin centers x_n $(n = 2, \ldots, N_{\text{bins}} - 1)$ at times t_m $(m = M, M+1, \ldots, \infty)$, we can discretize this PDE as before and write the following discretized equation:

$$
\partial_t\theta|_{mn} = -\tau_q\partial_{tt}\theta|_{mn} + \frac{k_0}{\gamma}\partial_{xx}\theta|_{mn} + r|_{mn}, \tag{B.5}
$$

[1] Schemes that are independent of the information from the current step in the time update are called explicit schemes.

where $r|_{mn}$ is the heat source term modeled by the KMC algorithm. This remains zero for all n and all time except for the bin n for which the dimerization event is selected by the KMC method during the time Δt_R described in Section 6 of Chapter 6. The terms $\partial_t\theta, \partial_{tt}\theta, \partial_{xx}\theta$ have the same meaning as described in Section B.1.1 and they are discretized accordingly.